University of Nevada, Reno

A Controllable Flexible Micropump and a Semi-Active Vibration Absorber Using Magnetorheological Elastomers

A dissertation submitted in partial fulfillment of the
requirements for the degree of Doctor of Philosophy in
Mechanical Engineering

By

Majid Behrooz

Dr. Faramarz Gordaninejad/Dissertation Advisor

May, 2015

We recommend that the dissertation
prepared under our supervision by

MAJID BEHROOZ

entitled

A Controllable Flexible Micropump and a Semi-Active Vibration Absorber Using Magnetorheological Elastomers

be accepted in partial fulfillment of the
requirements for the degree of

DOCTOR OF PHILOSOPHY

Faramarz Gordaninejad, Ph.D., Advisor

Mark A. Pinskey, Ph.D., Committee Member

Emil J. Geiger, Ph.D., Committee Member

Keri L. Ryan, Ph.D., Committee Member

Wanliang Shan, Ph.D., Committee Member

David W. Zeh, Ph.D., Dean, Graduate School

May, 2015

ABSTRACT

This study is focused on magneto-fluid-solid interaction analysis of a soft magnetorheological elastomer (MRE) controllable flexible micropump. In addition, material characterizations of MRE, modeling, fabrication and testing of a MRE-based vibration absorber system are investigated.

Theoretical modeling and analysis of a controllable flexible magnetically-actuated fluid transport system (CFMFTS**)** is presented. For the first time, soft magnetorheological elastomer (MRE) is proposed as an actuation element in a fluid transport system (micropump). The flexible micropump can propel fluid under a fluctuating magnetic field. Magnetic-fluid-solid interaction analysis is performed to determine deflection in the solid domain and velocity of the fluid under a magnetic field. The effects of key material and geometric system parameters are examined on the micropump performance. Two- and three-dimensional analyses are performed to model the asymmetric deflection of the channel under a magnetic field. It is successfully demonstrated that the proposed system can propel the fluid in one direction.

In addition, a novel semi-active variable stiffness and damping absorber (VSDA) is modeled, built and tested. Magnetically induced mechanical properties of MRE and their controllability are investigated by quasi-static and dynamic experiments. The VSDA is modeled, using springs, dashpots and the Bouc-Wen hysteresis element, fabricated and implemented in a scaled building to assess performance. Experiments are performed on a single VSDA, integrated system of four VSDAs, and a scaled building supported by four VSDAs. To demonstrate feasibility, a scaled, two-story building is constructed and installed on a shake table

supported by four prototype VSDAs. The properties of VSDAs are regulated in real time by varying the applied magnetic field through the controller. A scaled earthquake excitation is applied to the system, and the vibration mode is controlled by a Lyapunov-based control strategy. The control system is used to control displacement and acceleration of the floors. Results demonstrate that the proposed VSDA significantly reduces acceleration and relative displacement of the structure.

Keywords: Fluid Transport System, Soft Magnetorheological Elastomer, Micropump, Vibration Absorber, Variable Stiffness, Semi-Active Control, Variable Stiffness and Damping

ACKNOWLEDGMENTS

I would like to dedicate this work to my parents and my wife who encouraged and supported me towards the completion of this work.

I would like to express my sincere gratitude to Professor Faramarz Gordaninejad for providing this opportunity for me to be a part of his group at the Composite and Intelligent Materials Laboratory (CIML) at the University of Nevada, Reno. His excellent guidance led to successful completion of this work. I would also like to thank Dr. Xiaojie Wang for helping me to advance part of this research. Conducting my PhD research under the supervision of Prof. Gordaninejad and Dr. Wang in the field of magnetorheological elastomers was a great opportunity for me to work on cutting edge research with people who are at the top of their fields. It also taught me how to be an independent researcher, an effective teacher, and how to improve my interpersonal skills.

I would like to express my gratitude to my PhD Committee Members, Dr. Emil J. Geiger, Dr. Keri L. Ryan, Dr. Wanliang Shan and Dr. Mark A. Pinskey for their interest in my research and their helpful comments.

I also would like to thank all CIML student members with whom I collaborated. They certainly made my graduate study an enjoyable process. Finally, I would like to acknowledge that this work was supported in part by the National Science Foundation (NSF-Grant # CMMI #0900780).

TABLE OF CONTENTS

CHAPTER 1 1

INTRODUCTION 1

1.1. Controllable Flexible Magnetically –Actuated Fluid Transport System (Micropump) Utilizing MRE 2

1.2. MRE-based Variable Stiffness and Damping Absorber (VSDA) 6

1.3. Dissertation Organization 11

CHAPTER 2 14

A CONTROLLABLE FLEXIBLE MAGNETICALLY ACTUATED FLUID TRANSPORT SYSTEM 14

2.2. Modeling 19

2.3. Flow Analysis of a Converging Microchannel 21

2.4. Two-Dimensional Magneto-Fluid-Solid-Interaction (MFSI) Analysis 25

2.5. Parametric Two-Dimensional Analysis 36

2.6. Three-Dimensional Analysis 43

2.7. Parametric Three-Dimensional Analysis 50

2.8. Summary and Conclusions 58

CHAPTER 3 60

BEHAVIOR OF MAGNETORHEOLOGICAL ELASTOMERS WITH COATED PARTICLES....60

3.1. Introduction....60

3.2. Coated and Non-Coated Particle MRE Specimens....63

3.3. Shear Experiments....69

3.4. Summary and Conclusions....78

CHAPTER 4....79

MODELING OF A NEW SEMI-ACTIVE/PASSIVE MAGNETORHEOLOGICAL ELASTOMER VIBRATION ABSORBER....79

4.1. Introduction....79

4.2. Design of the MRE-Based VSDA....81

4.3. Double Lap Shear Experiments....85

4.4. Theoretical Study and Parameter Identification....88

4.5. The Integrated System....93

4.6. Summary and Conclusions....97

CHAPTER 5....98

PERFORMANCE OF A NEW MAGNETORHEOLOGICAL ELASTOMER ISOLATION SYSTEM....98

5.1. Introduction....98

5.2. Dynamic Performance of the VSDA 100

5.3. The Isolated Scaled Building 102

5.4. Lyapunov-Based Controller 105

5.5. Simulation of Controlled Isolated Scaled Building 107

5.6. Experimental Study 110

5.7. Summary and Conclusions 115

CHAPTER 6 117

SUMMARY, CONCLUSIONS AND FUTURE WORK 117

6.1. Summary and Conclusions of CFMFTS 117

6.2. Future Work for CFMFTS 117

6.3. Summary and Conclusions of VSDA 118

6.4. Future Work for VSDA 119

References 120

Appendix A. Fabrication of Magnetorheological Elastomers 144

Appendix B. Effect of Frequency on the Performance of the VSDAs 147

Appendix C. Data Acquisition System 149

Appendix D. Dynamic Performance of a Single VSDA 151

Appendix E. Design and Characterization of the Scaled Building 167

LIST OF FIGURES

Figure 1.1. Section view of traditional lead rubber bearing [57]..... 6

Figure 2.1. Relaxing and contracting of the lymphatic vessel [115]. 15

Figure 2.2. Deformation of a SMREM ; left to right: applied magnetic field H=50, 80 and 110 kAm-1 [31]. 16

Figure 2.3. Schematic of the function of the proposed ..... 18 SMRS-based one-way valve CFMFTS. 18

Figure 2.4. Large deformation of a SMREM..... 19

Figure 2.5. The proposed two-dimensional model for the CFMFTS. 20

Figure 2.6. Sinusoidal-shaped wall microchannel with elliptical cross section. 22

Figure 2.7. Numerical pressure gradient of sinusoidal-shaped wall microchannel with elliptical cross section a=200μm b=100 μm compared with analytical solution [133]..... 23

Figure 2.8. Velocity distribution of sinusoidal-shaped wall microchannel with elliptical cross section a=200 μm b=100 μm..... 24

Figure 2.9. Pressure distribution of sinusoidal-shaped wall microchannel with elliptical cross section a=200μm b=100 μm..... 24

Figure 2.10. Sample error of finite elemnt analysis. 27

Figure 2.11. A sample meshing for the 2D finite element analysis. 27

Figure 2.12. Distribution of magnetic flux density inside SMREM microchannel. 28

Figure 2.13. Distribution of magnetic flux density inside SMREM microchannel. 29

Figure 2.14. Fluid propulsion with zero input velocity..... 30

Figure 2.15. The rate of outflow for micropump without valve. 31

Figure 2.16. The volume of transferred fluid vs. time for micropump without valve. 31
Figure 2.17. Fluid propulsion with zero input velocity. 32
Figure 2.18. The rate of outflow at each time for micropump with valve. 33
Figure 2.19. History of the vomule of pumped fluid for microchannel without valve. 33
Figure 2.20. Deflection of the micropump at different times dring a cycle. 35
Figure 2.21. Effect of micropump diameter on the fluid flow. 37
Figure 2.22. Effect of valve length on the fluid flow. 37
Figure 2.23. Effect of valve opening distance on the fluid flow. 38
Figure 2.24. Effect of valve spacing on the fluid flow 38
Figure 2.25. Effect of elastic modulus on flow. 39
Figure 2.26. Effect of elastic foundation on the fluid flow. 40
Figure 2.27. Effect of fluid viscosity on the fluid flow. 41
Figure 2.28. Effect of electromagnetic load on the fluid flow. 42
Figure 2.29. Effect of magnetic permeability on the fluid flow. 43
Figure 2.30. Induced magnetic field in the flexible micropump. 44
Figure 2.31. Magnetic flux density along the wall of the SMREM micropump. 45
Figure 2.32. Three-dimensional model of the CFMFTS. 46
Figure 2.33. Discretization of the CFMFTS. 46
Figure 2.34. Sample error for three-dimensional analysis. 47
Figure 2.35. Velocity and deflection of MR micropump at maximum fluid velocity. 48
Figure 2.36. Rate of the flow during one cycle. 49
Figure 2.37. Total pumped fluid during one cycle. 49

Figure 2.38. Effect of micropump diameter on the fluid flow. 51

Figure 2.39. Effect of valve length on the fluid flow. 52

Figure 2.40. Effect of valve opening distance on the fluid flow. 53

Figure 2.41. Effect of valve spacing on the fluid flow. 53

Figure 2.42. Effect of elastic modulus on flow. 54

Figure 2.43. Effect of elastic foundation on the fluid flow. 55

Figure 2.44. Effect of fluid viscosity on the fluid flow. 56

Figure 2.45. Effect of electromagnetic load on the fluid flow. 57

Figure 2.46. Effect of magnetic permeability on the fluid flow. 58

Figure 3.1. The mechanism of surface coating of iron particles poly(tetrafluoropropyl methacrylate) through a combination of Reversible Addition Fragmentation Chain Transfer and click chemistry [146]. 65

Figure 3.2. SEM images of (a) non-coated and (b) coated iron particle [146]. 66

Figure 3.3. Electromagnet for curing MREs and the mold inside. 67

Figure 3.5. High pressure reactor for MRE ageing. 69

Figure 3.7. Double lap shear test setup and INSTRON dynamic testing system. 72

Figure 3.8. Pure elastomer (a) without oxidation, and (b) after one week of oxidation. 73

Figure 4.1. (a) Schematic of the cross section of VSDA, and (b) photo of the VSDA. 83

Figure 4.2. Magnetic field distribution inside the VSDA for different input currents. 84

Figure 4.3. Double lap shear test setup on the INSTRON dynamic testing system. 86

Figure 4.4. Shear deformation test results of VSDA at 0.1 Hz 87

Figure 4.5. The proposed phenomenological model. 89

Figure 4.6. On-state and off-state shear force deformation characteristics of VSDAs for 5% strain at 0.1 Hz..... 91

Figure 4.7. Off-state strain-dependent behavior of VSDAs at 0.1 Hz..... 92

Figure 4.8. On-state strain-dependent behavior of VSDAs at 4 Amps and 0.1 Hz. 93

Figure 4.9. Photo of the experimental setup for the integrated system with four VSDAs. .. 95

Figure 4.10. SIMULINK model of the integrated system. 96

Figure 4.11. Transmissibility results of the integrated system of VSDAs for various input currents.....96

Figure 5.1. Photo of the dynamic shear test experiments 101

Figure 5.2. (a) Transmissibility, and (b) Phase angle of 0.1g sinusoidal constant amplitude acceleration input for input electric currents ranging from 0 to 3 Amps. The insert in Figure 2 (a) represents peak frequency vs. input electric current. 102

Figure 5.3. Photo of the experimental setup. 103

Figure 5.4. SIMULINK model of the controlled isolated scaled building. 108

Figure 5.5. The scaled El Centro earthquake EW (a) acceleration, (b) power spectrum density. 109

Figure 5.6. Passive and controlled: (a) acceleration, and (b) displacement of the third floor. 110

Figure 5.7. Typical results of the effect of VSDAs and control strategy on the third floor acceleration.....111

Figure 5.8. Typical results of the effect of VSDAs and control strategy on the relative displacement of the third floor. 112

Figure 5.9. Power spectrum density of acceleration and displacement. 113

Figure 5.10. Maximum relative (a) acceleration and (b) displacement of the scaled building. 114

Figure 5.11. Maximum absolute (a) acceleration and (b) displacement of the scaled building. 114

Figure A.1. Photo of: (a) Electromagnetic device, and (b) MREs mold..... 144

Figure A.2. Silicone–RTV MRE with 70% wt. iron..... 144

Figure A.3. The fabricated rubber support and mold..... 145

Figure A.4. The optical images of aligned iron particles in silicone–RTV MREs: (a) 2x, and (b) 20x in magnification. 146

Figure B.1. Off-state frequency dependent behavior of VSDAs at 5% strain. 147

Figure B.2. On-state frequency dependent behavior of VSDAs at 5% strain. 148

Figure C.1. Block diagram of the control of a two-story building with four VSDAs..... 150

Figure D.1. Photo of the experimental setup. 152

Figure D.2. Transmissibility of 0.1g sinusoidal constant amplitude acceleration input for different input electric currents ranging from 0 to 3 Amps. The insert in Figure 2(a) represents peak Dynamic performance of the VSDA in an Integrated System..... 157

Figure D.3. Phase angle difference for 0.1 g sinusoidal constant amplitude acceleration input for different input electric currents ranging from 0 to 3 Amps..... 158

Figure D.4. Transmissibility of 0.2g sinusoidal constant amplitude acceleration input for different input electric currents ranging from 0 to 2.5 Amps, Insert in Figure: Peak frequency vs. change in input electric current for 80%wt. non-aligned MRE..... 160

Figure D.5. Phase angle of 0.2g sinusoidal constant amplitude acceleration input for different input electric currents ranging from 0 to 2.5 Amps for 80%wt. non-aligned MRE. 160

Figure D.6. Transmissibility of 0.2g sinusoidal constant amplitude acceleration input for different input electric currents ranging from 0 to 2.5 Amps, Insert in Figure: Peak frequency vs. change in input electric current for 80%wt. aligned MRE. 161

Figure D.7. Phase angle of 0.2g sinusoidal constant amplitude acceleration input for different input electric currents ranging from 0 to 2.5 Amps for 80%wt. aligned MRE. 162

Figure D.8. Stiffness change of VSDA for 80%wt. aligned MRE compared to 80% wt. non-aligned MRE. 163

Figure D.9. Damping change of VSDA for 80%wt. aligned MRE compared to 80% wt. non-aligned MRE. 163

Figure D.10. Temperature increase in MREs with 4 Amps electric current input. 165

Figure D.11. Transmissibility of 0.3g sinusoidal constant amplitude acceleration input for different input electric currents ranging from 0 to 5 Amps for MRE and Rubber material system 2, Insert to Figure 11(b): Peak frequency vs. input electric current. 166

Figure E.1. The schematic of the instrumentation of the scaled building test setup. 168

Figure E.2. The numerical model of the isolated scaled building without additional mass.169

Figure E.3. The numerical model of the isolated scaled building with additional mass. 170

Figure E.4. Transmissibility of 0.05 g sinusoidal constant amplitude acceleration input for 0 and 1 Amps input electric currents for the 1st floor of the scaled building without additional mass. 172

Figure E.5. Transmissibility of 0.05 g sinusoidal constant amplitude acceleration input for 0 and 1 Amps input electric currents for the 2nd floor of the scaled building without additional mass.....172

Figure E.6. Transmissibility of 0.05 g sinusoidal constant amplitude acceleration input for 0 and 1 Amps input electric currents for the 3rd floor of the scaled building without additional mass.....173

Figure E.7. Transmissibility of 0.05 g sinusoidal constant amplitude acceleration input for different input electric currents of 0 and 1 Amps for the 1st floor of the scaled building with 16.6 Kg additional mass on each floor. 174

Figure E.8. Transmissibility of 0.05 g sinusoidal constant amplitude acceleration input for different input electric currents of 0 and 1 Amps for the 2nd floor of the scaled building with 16.6 Kg additional mass on each floor. 175

Figure E.9. Transmissibility of 0.05 g sinusoidal constant amplitude acceleration input for different input electric currents of 0 and 1 Amps for the 3rd floor of the scaled building with 16.6 Kg additional mass on each floor. 175

LIST OF TABLES

Table 3. 1. Effective Shear Modulus and Percentage of MR Effect. 77

Table 4. 1. Constant Parameters Used for VSDA Modeling. 90

Table 4. 2. Strain-Dependent Parameters Used for VSDA Modeling. 91

Table 5.1. Comparison of the scaled building percentage of maximum absolute acceleration and displacement changes. 115

Table D.1. Characterization Properties of VSDA for 0.2 g Acceleration Input. 154

Table D.2. Characterization Properties of VSDA for 0.3 g Acceleration Input. 155

Table D.3. Characterization Properties of VSDA for 0.4 g Acceleration Input. 155

Table D.4. Single VSDA Damping and Stiffness with 80%wt. Aligned MRE and for Different Input Electric Currents and Different Acceleration Inputs 156

Table E.1. Scaling factors used for the scaled building. 167

Table E.2. Comparison Between First Natural Periods of the Isolated Scaled Building Using Different Methods. 170

CHAPTER 1

INTRODUCTION

This study is divided into two sections -- a controllable flexible magnetically-activated micropump, and a base isolation of structure using magnetorheological elastomer (MRE). The study of magneto-fluid-solid interaction of a flexible controllable transport system employs soft MRE membrane (SMREM) as the actuation element. The uniqueness of this study is the combined effect of magnetic actuation on a flexible microfluidic system. This work leads to fundamental understanding of the propelling fluid with a controllable actuator which is activated by a magnetic field. The result of this work could potentially be helpful in developing a system that can be used, for example, for biological fluid delivery, such as, food or drug delivery or human lymphatic vessels.

The second part of this research describes vibration isolation of structure using a unique, MRE-based controllable system. Vibration isolation is vital in structures in preventing and/or reducing damage and save lives during natural hazard events. Various active, passive and semi-active absorbers have been proposed and utilized during past decades but each option has its advantages and drawbacks. MRE-based absorbers can be an attractive choice since they can be controlled semi-actively.

1.1. Controllable Flexible Magnetically –Actuated Fluid Transport System (Micropump) Utilizing MRE

The inspiration of the first part of this research comes from the lymphatic vessels in human body. The lymphatic system collects lymph throughout the body and transports the lymph back to the blood. The lymphatic system has two types of valves: primary and secondary. Interstitial fluid enters the primary valves of lymphatic vessels and secondary valves are one-way valves that help lymph to move forward, unidirectionally. The lymphatic vessels pump the fluid in a sequence of propagating wave via the one-way valves along the vessels. There have been numerous efforts to examine artificial blood vessels. Different designs of artificial blood vessels using elastomers and live cells are patented [1, 2]. Artificial blood vessels have been made over the past 50 years from different passive materials including PolyTetraFluoroEthylene and live cells [2], Polyethylene terephthalate and polyester [3] and smooth muscle and endothelial cells of blood vessels [4]. Other researchers have made and implanted artificial vessels made of collagen and PolyGlycolic Acid [5]. However very few investigations have suggested an artificial lymphatic vessel [6]. The complexity of lymphatic vessels compared to blood vessels lies in the different fluid transfer system. The blood vessels utilize the heart and its one way valves to propel the blood, but lymphatic vessels need to transfer body fluid with contraction of the vessel itself and through a series of one way valves inside the vessel. Smooth muscle within the wall of the lymphatic vessel generates the contraction needed to propel the lymph.

To understand the mechanism of fluid propulsion and design of such fluid transport system, one needs to properly model the behavior of the flexible microchannel. There has been

numerous research on modeling the mechanical behavior of human blood vessels, but modeling either the primary or secondary part of the lymphatic system is relatively new, and unique. Most efforts have been conducted in the last decade; however, there are still many challenges to be addressed [7]. Lymph is a transparent fluid with properties close to water. The viscosity of Lymph has been measured 1.5 to 2.2 cP for dogs [8] or is considered to be the same as water [9]. Thus, for the purpose of simulation, water properties can be used as a good approximation. A lumped-parametric model and parameter sensitivity analysis are performed for lymphatic system [10]. Galie et. al. developed a computational model to predict the velocity and pressure of the primary lymphatic valves [11]. Rahbar [9] modeled the lymph flow with a moving wall without considering the effect of the wall on the fluid movement known as the fluid solid interaction (FSI). Stresses on walls of a tube can be modeled as static pressures, but, interaction between the fluid and the wall can influence the results, and thus, fluid structure interaction might be necessary. However, performing FSI analysis is three to four times more time consuming [12]. To accurately study a flexible fluid transport system, FSI study needs to be performed.

FSI is a multiphysics problem which deals with the interaction between structural deflection and fluid movement physics. FSI has been used for interaction between blood and blood vessels such as investigation of general blood flow [13, 14], arterial blood flow analysis [15, 16], and aorta blood flow analysis [17]. FSI problems are usually too complicated to be solved analytically and hence numerical-based strategies are usually employed to find a solution [18–22]. Also, because of the complexity of the problem, researchers tried to find more efficient numerical solvers [23]. In some FSI problems, movement of solid boundary causes the fluid to

move and hence the fluid domain discretization should follow the movement of the corresponding solid boundary. Most numerical methods use the Arbitrary Lagrangian Eulerian (ALE) method to take fluid mesh movement into account [24–26]. In FSI models three types of elements need to be defined for the fluid domain, interface domain, and structure domain [27]. Also, large displacement affects the FSI analysis and strategies were proposed for considering the effect of large displacement [28, 29] on FSI analyses.

Deformation of the solid domain can be due to an external surface or boundary load such as mechanical stress, magnetic, or electric induced deformation. Application of a magnetic field can cause magnetostriction. This means that the magnetic field can create deformation (or actuation) in the magnetically permeable material. Barham et. al. [30] presented a solution for deformation of pressurized magnetic membrane based on magnetoelasticity. Raikher et. al. [31] presented an analytical formulation for deformation instability of magnetic membrane within magnetic field and solved the related magnetoelasticity problem numerically.

There is limited work on magnetically actuated micropumps with potential biomedical applications [32–34]. By embedding a permanent magnet inside an elastomeric membrane, an electromagnetic powered micropump can be achieved [35–38]. Wang et. al. presented a design for an electromagnetically actuated micro-valve pump using magnetic membrane [39]. Ferrofluids have been suggested as actuation element of the micropumps [40–42]. Magnetic shape memory alloy is also used for a magnetic micropump [43]. LaRocque et. al. [44] suggested a peristaltic actuator using polymer foam infused by MR Fluid.

Polymers filled with ferrous or magnetic particles have recently received attention as actuation elements for microfluidic devices [45]. Polymer filled with iron particles is used as

actuation element of a micropump under magnetic field [46]. Recent works by Khaderi et. al. [87, 88] investigated the magnetic fluid solid interaction analysis of artificial cilia and showed the effect of different geometrical configurations on the generated flow by their proposed system. Fahrni et. al. [89] developed the magnetic artificial cilia using polymer and experimentally investigated the deformation of the cilium under a fluctuating magnetic field induced by a rotating magnet. Hussong et. al. showed the generated flow through such a system [90]. Magnetic actuation of artificial cilia was shown by Peng et. al. [91].

There have been many investigations on magnetic microvalves, but they usually include mechanical and non-flexible components [47]. Prosthetic microvalves have been suggested for human circulation systems with non-flexible mechanical components [48]. Passive flexible valves prosthetic with stents are also suggested in [49–51]. A heart valve made of only polymers with stiffer materials for stent and softer materials for the valve has been suggested [52].

Valveless configurations reduce the complexity of the system as suggested for a magnetic micropump by Yamamata et. al. [37]. Valves can be formulated with lumped parameter model or finite element models. Bertram et. al. [53] modeled the valves in lymphatic vessels as resistances dependent on transmural pressure. For FSI numerical simulation, valves can be modeled in two-dimensional space, but flexible valves usually have a three-dimensional deformation, which requires three-dimensional simulations. Simplified 2D [54] and 3D models of aortic valve were investigated by Hart et. al. [55]. Fluid structure interaction modeling of aortic valves has been performed by Marom et. al. [56] to observe stresses in the valve wall and associated velocities at different instances.

1.2. MRE-based Variable Stiffness and Damping Absorber (VSDA)

The inspiration for the design of the VSDA comes from traditional lead rubber bearings which are widely used for structural applications. Figure 1.1 represents a typical lead-rubber bearing which has steel shims that prevents bulging in high axial loads.

Figure 1.1. Section view of traditional lead rubber bearing [57].

A VSDA can change stiffness and damping of the system, thus avoiding resonant frequencies and improving the system's response during excitation. By implementing VSDAs along with appropriate control strategy, resonant response can be avoided and system behavior can be suppressed. Semi-active absorbers have been shown to be effective in vibration isolation of structures [58, 59]. Most conventional variable stiffness devices are mechanical devices [58, 60] or hydraulic systems [61–63] and have inherent disadvantages, such as, complex structure, slow response and leakage [64].

A MRE-based device may provide a solution to these challenges. MRE-based devices can operate in a wide range of frequencies, can tolerate large shear deformations, and have fast

response time which makes them desirable for natural hazard applications. Furthermore, MRE-based devices do not have complex structures and do not have the leaking or sedimentation issues as compared to MR fluid dampers.

Magnetorheological materials offer controllable mechanical properties by application of a magnetic field. There are different magnetically controllable materials including MR fluid, MRE, MR foam and MR gel [65] that show different mechanical or electrical properties under an external magnetic field. MREs are composed of micron sized magnetic permeable particles and an elastomeric medium. MRE is solid, flexible, can operate in wide range of frequencies, and tolerate large deformations in tension, compression and shear. MRE has a fast response time (in order of milliseconds) under a magnetic field [66].

Stiffness of MREs can be altered by applying a magnetic field for over 100 percent [67]. Shear modulus in MREs can be found from Eq. (1.1) which relates volume fractions, permeability and applied magnetic field to shear modulus [68]:

$$G = 12\phi_p\mu_0\mu_m\left(\frac{R}{d}\right)H_0^2\frac{(\mu_p-\mu_m)^2}{\sqrt{1+\varepsilon^2}\left(3\sqrt{1+\varepsilon^2}(\mu_p+\mu_m)-4\left(\frac{R}{d}\right)(\mu_p-\mu_m)\right)^2} \quad (1.1)$$

where ϕ_p is the volume fraction of particles, μ_0 is the permeability of free space, μ_m is the permeability of the matrix, μ_p is the permeability of iron particles, R is the radius of particles, d is the distance between particles, H_0 is the applied magnetic field, and ε is the shear strain. Application of the magnetic field changes the shear modulus of MREs, and as a result the natural frequency of MREs change according to Eq. (1.2) [69]:

$$\Delta\omega = \omega_o \left(\sqrt{1 + \frac{\Delta G}{G_o}} - 1 \right) \tag{1.2}$$

where ω_o and G_o are the off-state natural frequency and off-state shear modulus and $\Delta\omega$ and ΔG are the change in natural frequency and shear modulus due to magnetic field. Depending on the location of the MRE device i.e. on the top of the structure or beneath the structure, and the supported mass, a MRE-based absorber can change the natural frequency of the system.

Damping in MREs is mainly due to the elastomer matrix, iron particles, matrix interface, and magneto-mechanical hysteresis damping [70]. Damping of MREs also changes within magnetic field but it is mainly dependent on the type of elastomer matrix, since damping in MREs is created by interfacial slipping among particles and the matrix and is higher for larger iron particle percentages [71]. Damping ratio of MRE can be written as [71]:

$$D = \varphi_m D_m + \mu n (F_0 + F_m) s \tag{1.3}$$

where φ_m is the volume percentage of the matrix, D_m is the damping ratio of the matrix, n is the number of the particles in the unit volume of MRE, S is the interfacial displacement, μ is the friction factor among iron particles and matrix and F_0 and F_m are interaction forces between elastomer matrix and particles with and without magnetic field.

Controllability of MR elastomer makes them a desirable choice for vibration control and actuation. The controllable properties can be utilized in variable stiffness and damping devices such as a prototype for car suspension bushing [66], a conceptual design for vehicle

transmission system vibration reduction [72] and adaptive vehicle seat suspension [73]. Other researches proposed soft MRE for air flow controllable valve [74] and adjustable springs in prosthetic devices [75]. Also, MREs can be used for sensing applications since their capacitance and conductance change with an application of a magnetic field [66].

MRE has been numerically shown to be effective is vibration isolation of structures [76]. A semi-active/passive absorber using magneto-rheological elastomer has potential applications for base isolation [77]. MRE-based devices have been used as the controllable semi-active elements in various vibration isolation applications including base isolation of a structure [78], adaptive tuned vibration absorbers [79–81] and dynamic vibration absorbers [82-83]. It has been shown that MREs can be used in variable stiffness devices for vibration control [65, 66, 82, 84, 85]. In structural applications MRE have been used in Adaptive Tuned Vibration absorber (ATVA) [80, 83, 86–92] and base Absorber for building structures [93, 94]. ATVAs are devices that add to the system as an additional mass and change system's stiffness and damping but base absorbers are located under the building. ATVAs can shift the natural frequency of the system by changing the shear modulus of MREs [86]. ATVAs with a real time controller can potentially suppress the response of a building compared to passive dynamic vibration absorbers [95].

Modification of traditional lead rubber bearing with MREs has led to a new controllable bearing device [96] and a small-scale MRE-based bearing was studied as base absorber for structural applications [97]. To use VSDAs for vibration control, the shear force deformation relationship needs to be identified. Shear force deformation relationship of MREs have been

experimentally investigated [98] and models have been proposed to predict behavior of MRE devices under various mechanical deformation and applied magnetic fields [99, 100].

MREs have recently been proposed and used as base absorber for structural applications [78]. Recently Li et. al. [101] presented an absorber using MRE and presented shear force characteristics for different applied current and different input load frequency.

Utilizing MREs without a controller may not be beneficial for all frequency bands, thus, a controller can tune their properties based on the input vibration to minimize the transferred vibrations. Hence, using controllable base absorbers may result in better performance in terms of both acceleration and displacement reduction. Semi-active control strategies have been effective for structural vibration mitigation applications [102] Also, semi-active vibration absorbers can potentially outperform passive absorbers with minimum input power, if their mechanical properties are tuned with a controller [60]. Recently it has been shown that semi-active base isolation using magnetorheological damper and ball-cone absorber can achieve isolation capabilities for a six story scaled building similar to active absorbers but with less power consumption [103].

Most semi-active absorbers are intended to mitigate vibrations by changing either stiffness or damping or both in the structures. Semi-active vibration absorbers have been proven to be effective and economical in structural control [59]. Moreover, semi-active absorbers are superior to passive systems with smaller input power requirements [104, 105] while they can be as effective [106] or even outperform active vibration reduction systems [61]. Semi-active controllable dampers can simultaneously reduce the acceleration and displacements in a structure [107], but reliability issues may limit their application for civil structures [108].

Different control strategies including optimal control [109, 110], maximized energy dissipation with on-off control [111], skyhook [110], and Lyapunov based strategies [111–113] have been implemented for controlling MRF dampers, but limited studies have been conducted on control of MRE based devices. Different control strategies for structural control have been proposed for design purposes [114] and Jansen et. al. [111] compared different control strategies and found Lyapunov and clipped optimal control as the most effective strategies for semi-active structural control. In a recent theoretical work, a MRE isolation system has been implemented to a scaled structure with a fuzzy logic control strategy [78].

This study aims at the feasibility of a novel, fail-safe, VSDA as a base isolation bearing system. The VSDA presented in this work has a novel design. Due to the integration of MRE and passive rubber elements in its design, the proposed VSDA is fail-safe. That means that if electronics and power failure occur, the VSDA retains a minimum functionally of a passive rubber steel base absorber. To validate the capability of MREs and to demonstrate that it can be utilized as controllable protective devices, new MRE materials as well as prototypes of MRE variable stiffness systems are developed, characterized, and tested.

1.3. Dissertation Organization

The first Chapter is the introduction to topics that are covered in this research including the CFMFTS and the VSDA. This Chapter presents a detailed literature review of the state-of-the-art regarding magnetic and FSI analysis and the relevant proposed applications in this field. It also reviews work in the field application of MRE for vibration control including in structural control.

The second Chapter describes the application of soft magnetorheological elastomer for a controllable flexible magnetically-actuated fluid transport system (CFMFTS). In this Chapter the capability of the proposed system for propelling required amount of fluid is inspected. First the pressure change of the sinusoidal boundary condition is investigated by the COMSOL finite element package and analytical modeling to observe the accuracy of the finite element model. Then, the magnetic-fluid-solid interaction (MFSI) behavior of the time varying sinusoidal boundary condition is inspected numerically with two-dimensional analyses and effect of each system parameter is investigated. Finally a three-dimensional model of the problem is developed, analyzed and discussed.

The third Chapter presents the procedure of coating particles for MRE. The polymerization of the iron particles changes the surface of the particles and hence changes the mechanical and endurance properties of the MREs. Such properties under the effect of accelerated oxidation have been investigated by means of double lap shear experiments.

The forth Chapter describes a novel base absorber which employs MR elastomer to make the base absorber controllable. The design of the absorber is inspired by the traditional lead rubber bearing (LRBs). First an MRE-based absorber is designed based on optimization of the magnetic field passing through MREs to achieve the highest change in the stiffness. Quasi-static shear tests have been performed on the VSDAs to prove the ability of the VSDAs to change the stiffness and damping. Then, the mechanical behavior is modeled using a phenomenological model. Dynamic tests have been performed to observe the ability of the VSDAs to change the stiffness and damping with Swept Sine technique. Then, an integrated system is designed with a mass to observe the effect of the VSDAs in changing stiffness of a

system. Using the calculated constants for the model and a SIMULINK model, this behavior is modeled accurately.

The fifth Chapter explains a 1:16 scaled building which is isolated by four VSDAs. Scaled seismic inputs are applied to the isolated scaled building and effectiveness of VSDAs to mitigate the seismic vibration is investigated. The Lyapunov based control strategy is used to control the behavior of the scaled building. The behavior of the isolated scaled building under seismic vibration is numerically modeled using SIMULINK. Performance of the system with the parameters found from numerical study, is investigated using shake table experiments. It describes the results of controlled isolated scaled building and control procedure.

The sixth Chapter presents the summary and concluding remarks of this research. It also presents the proposed future work for this research.

CHAPTER 2

A CONTROLLABLE FLEXIBLE MAGNETICALLY ACTUATED FLUID TRANSPORT SYSTEM

2.1. Introduction

This Chapter presents analytical and numerical investigations of a controllable flexible magnetically-actuated fluid transport system (CFMFTS). The inspiration of the proposed system comes from the vessels and secondary valves of the lymphatic system in human body that moves lymph unidirectionally. The proposed system can potentially have other biomedical applications, such as, augmentation of the damaged lymphatic vessels either as a replacement or as an auxiliary lymph transport vessel. The CFMFTS would be helpful for people with lymphatic conditions by substituting larger lymphatic vessels with diameters greater than 500 microns. CFMFTS may also be used for other biological fluid transport where it is necessary not to damage cells and organisms with fast movement and sharp edges of regular pumps. With a smooth peristaltic movement, CFMFTS ensures not to damage the bio-fluids therefore it can also be utilized in food and drug delivery systems.

The lymphatic system collects lymph throughout the body and transports lymph back to blood. Lymph is a transparent fluid with the viscosity of 1.5 to 2.2 cP for dogs [8] and for the simulation, it can be represented by water which has similar fluid properties [9, 11]. The lymphatic system has two types of valves: primary and secondary.

Primary valves are where the interstitial fluid enters the lymphatic vessel and secondary valves are one-way valves that help lymph to move unidirectionally. The lymphatic vessels move the liquid with a sequence of propagating waves with the aid of the one-way secondary valves at intervals along the vessels. Lymphatic vessels have smooth muscles that have contracting and relaxing cycles called Systole and Diastole [115] to move the lymph as shown in Figure 2.1. When the Lymphangyon is compressed, a posetive pressure is generated and right hand side valve will open to let the lymph move unidirectionally. When the pressure is released and lymphangyon expands, left valve will open to let the lymph enter the lymphangyon. Such a phenomenon is the inspiration of the propoesd electromaechanical smooth fluid transport system.

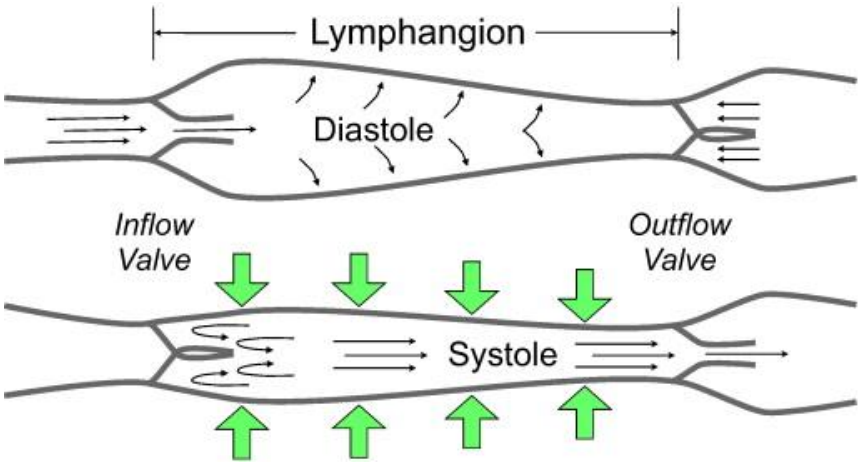

Figure 2.1. Relaxing and contracting of the lymphatic vessel [115].

To understand the mechanism of the fluid propulsion in the CFMFTS, a numerical modeling is needed that can illustrate the performance. In some cases, the movement of solid boundary causes the fluid to move and the fluid finite element mesh should follow the movement of the corresponding solid domain. Arbitrary Lagrangian-Eulerian method can

consider the fluid mesh movement [24–26]. In finite element fluid-solid interaction analysis, three types of elements are needed for the fluid, interface and structure domain [27]. The large displacement affects the fluid-solid interaction analysis and strategies [28, 29]. The proposed CFMFTS consists of soft magnetorheological elastomer membrane (SMREM) as the actuation element of the system. A SMREM is made of a soft highly-elastic matrix with embedded micron-sized ferromagnetic particles. Once a magnetic field is applied to SMREM, it deflects within a few milliseconds as shown in Figure 2.2. Such a movement is used in the proposed system to generate micro-propulsion.

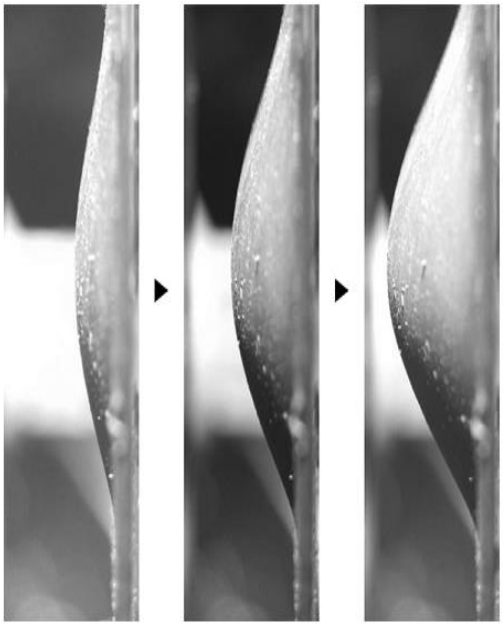

Figure 2.2. Deformation of a SMREM ; left to right: applied magnetic field H=50, 80 and 110 kAm-1 [31].

An applied magnetic field can produce a significant deformation in soft magnetically permeable materials depending on the stiffness of the material. Different analytical and numerical studies have examined the nonlinear behavior of such materials within a magnetic

field. Barham et. al. [30] studied the behavior of a pressurized magnetic membrane based on magnetoelasticity. There is a threshold in the amount of magnetic field required to initiate the deformation which was analytically investigated by Raikher et. al. [31]. A few applications have been proposed for magnetic induced actuation such as an electromagnetically actuated micropump using a magnetic membrane [39]. Angel [116] implemented a magnetic membrane in an adjustable mirror, and LaRocque et. al. [44] proposed a magnetic peristaltic actuator using a polymer foam infused by a magnetorheological fluid.

In the proposed system magnetic field deforms the SMREM and a pressure generated from this action pushes the fluid forward through a series of one-way valves as illustrated schematically in Figure 2.3. An electromagnet is designed to induce a magnetic field that actuates the SMREM. The electromagnet surface will be located at a distance from the microchannel to simulate an actual working condition. The proposed system is reliable, flexible and implantable with low-power requirement. The elastomer needs to be highly flexible for this system to have the maximum deflection upon applying magnetic field. The elastic modulus is considered 100 kPa in order to minimize the input power required to actuate the SMREM. The material also needs to have high fatigue endurance since it is subjected to fluctuating force.

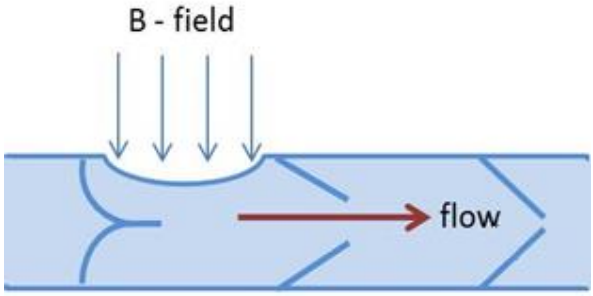

Figure 2.3. Schematic of the function of the proposed SMRS-based one-way valve CFMFTS.

In this study, performance of the proposed CFMFTS is investigated using a time-dependent magneto-fluid-structure interaction finite element analysis. First, the flow of fluids through sinusoidal wall is modeled, numerically analyzed, and compared with an analytical solution, for a passive case (i.e., zero applied magnetic field) to examine the accuracy of the finite element fluid modeling. Then, the effect of SMREM deflection on the net flow of two microchannels with and without valves is considered. A two-dimensional (2D) time-dependent model using a coupled fluid-solid and magnetic interaction is developed. The modeling and analysis are extended to include a magnetic field that is applied to the wall of the flexible microchannel in order to produce the one-way forward movement of the fluid. A parametric study has been performed to observe the effect of different electromagnetic and mechanical system properties on the performance of the system. A three-dimensional model is developed to examine the effect of asymmetric deflection of the SMREM tube on fluid flow results.

2.2. Modeling

A SMREM is considered to be consisting of a highly-elastic matrix with embedded micron-sized ferromagnetic particles. Once a magnetic field is applied to the SMREM, it deflects within a few milliseconds. Figure 2.4 shows large deformation of a sample SMREM under a magnetic field. Such a movement is utilized to generate a micro-propulsion.

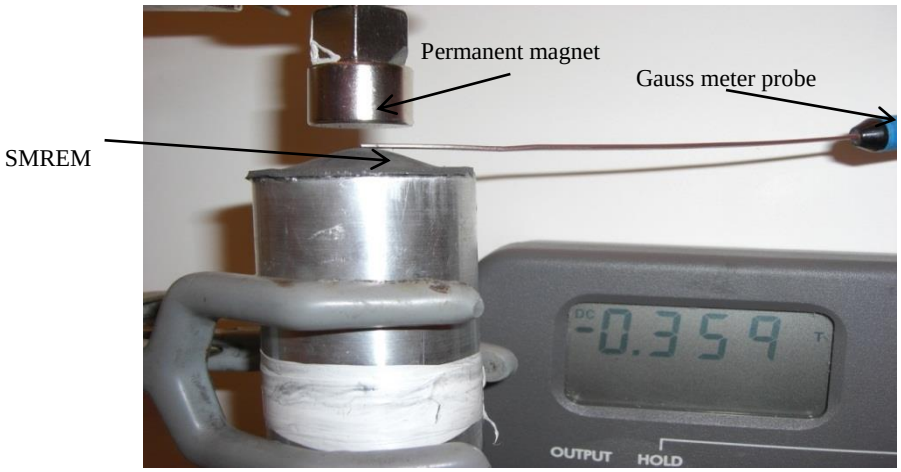

Figure 2.4. Large deformation of a SMREM.

A two-dimensional analytical work is considered to obtain an understanding of the behavior of the entire CFMFTS, which consists of one-way flexible valves incorporating SMREM, controlled by a magnetic field. The cross-section of the system is schematically demonstrated in Figure 2.5**.** The CFMFTS consists of a SMREM, passive rubber, and a series of one-way valves. The valves are flexible, which allow the fluid flow in and out depending on the movement of the SMREM wall. An applied magnetic field on the SMREM produces time-varying loads on the microchannel, mimicking the contractile activity and regulating flow. An electromagnet located at a distance from the microchannel is designed to induce a strong enough magnetic field that can magnetize iron particles and hence actuate the SMREM. The magnetic

field deforms the top part of the microchannel made of SMREM while the bottom part moves less only due to the generated pressure. Such an asymmetric movement generates a net pressure in the space between the two valves and pushes the fluid forward. The elastic foundation modeling represents the surrounding environment, which restricts the movement of the microchannel, depending on the magnitude of the spring constant.

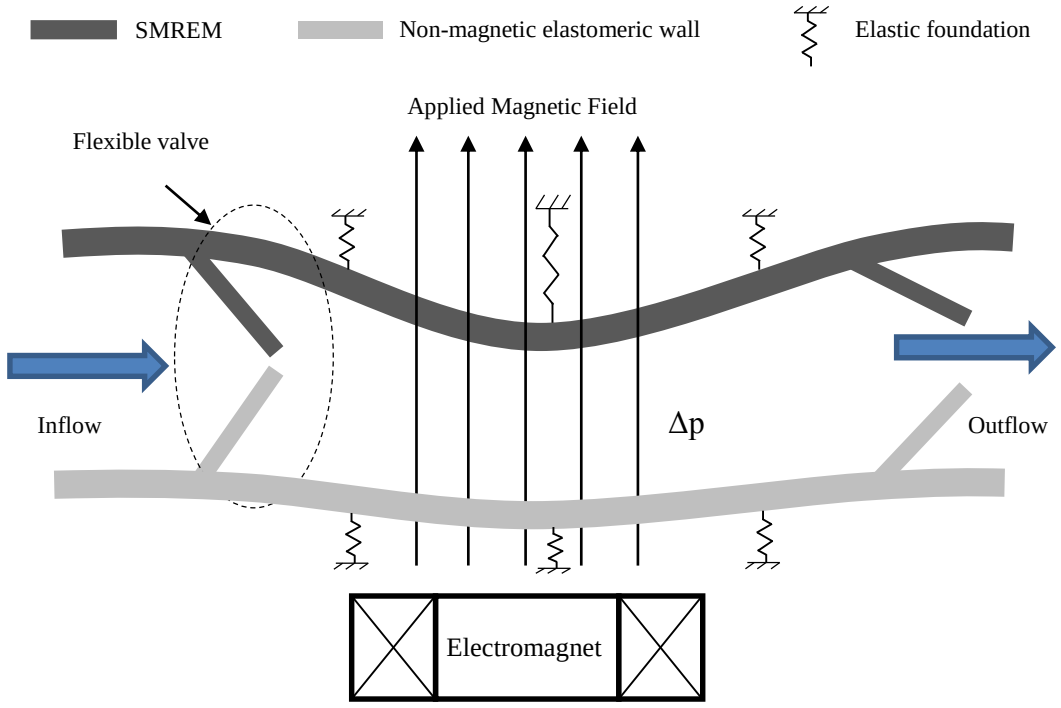

Figure 2.5. The proposed two-dimensional model for the CFMFTS.

The numerical modeling can predict the flow behavior of fluid throughout the CFMFTS in response to an external magnetic field. The proposed model should consider the fluid, solid and magnetic field physics. The performance of the CFMFTS is evaluated by examining design parameters, such as the microchannel and valve geometry, magnetic field density, mechanical and electromagnetic material properties of SMREM.

For this study, three modules of fluid, solid, and electromagnetic are needed, if a multiphysics finite element package is employed. COMSOL multiphysics finite element package is used to couple the above-mentioned modules. First a 2D analysis is performed to investigate the mechanism of the effect of magnetic field on the SMREM. Then, a three-dimensional (3D) finite element analysis of the system with elastic foundation is performed. The interaction of pressure and deformation of the SMREM due to an external magnetic field determines the flow patterns inside the chamber, movements of valves, and the volume of fluid transported. In order to model the deformation of the SMREM, when subjected to uniform or non-uniform magnetic fields, a 3D finite element model is developed based on Maxwell's, Navier-Stokes, and equations of motion of an elastic body to obtain the interaction forces of the ferromagnetic particles, as well as, permeability changes with large deformations. Finally 2D and 3D studies are compared.

2.3. Flow Analysis of a Converging Microchannel

To verify the flow analysis, a converging microchannel with sinusoidal wall boundary condition is analyzed using COMSOL multi-physics software. Results are compared to an analytical solution using the following non-dimensional formulation [117], as shown in Figure 2.6.

$$\hat{p} = \left(\frac{\rho U_0^2}{\varepsilon Re}\right) p \tag{2.1}$$

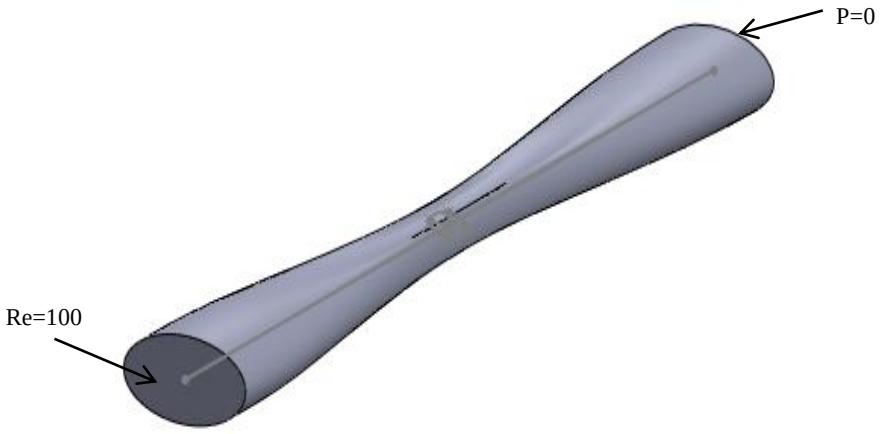

Figure 2.6. Sinusoidal-shaped wall microchannel with elliptical cross section.

Comparisons between the numerical and analytical non-dimensional pressure gradient of a converging microchannel for the input Reynolds number of 100 and the discharging fluid to the atmospheric pressure is shown in Figure 2.7. Microchannel's length is 3mm and the major radius is 200μ and a minor radio is 100μ for this analysis. The numerical results of both the maximum pressure and the pressure drop agree well with the analytical results.

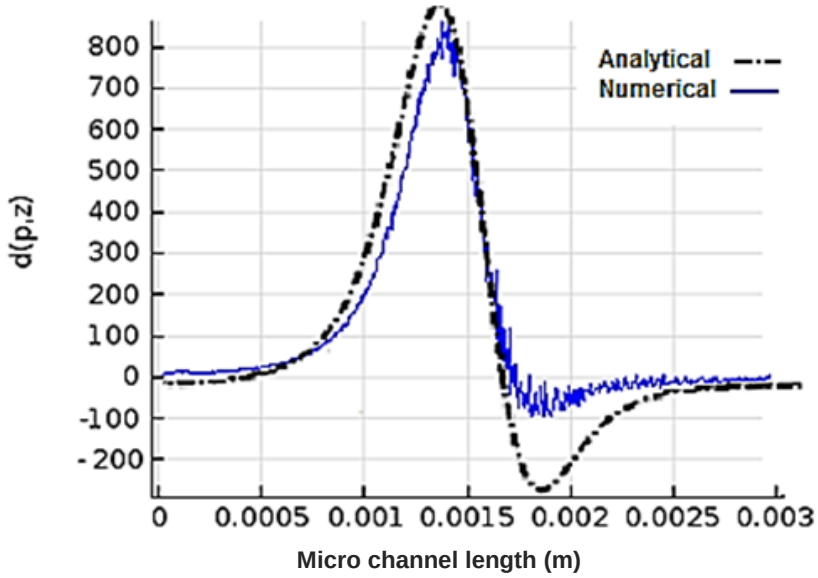

Figure 2.7. Numerical pressure gradient of sinusoidal-shaped wall microchannel with elliptical cross section a=200µm b=100 µm compared with analytical solution [133].

Figure 2.8 illustrates the velocity of the sinusoidal-shaped wall and elliptical cross-section microchannel and Figure 2.9 shows pressure drop for the same geometry and boundary conditions. As can be seen, the velocity and pressure changes are consistent with the Bernoulli's principal. It is demonstrated that the maximum velocity along with zero pressure occurs slightly after the minimum cross section of the microchannel.

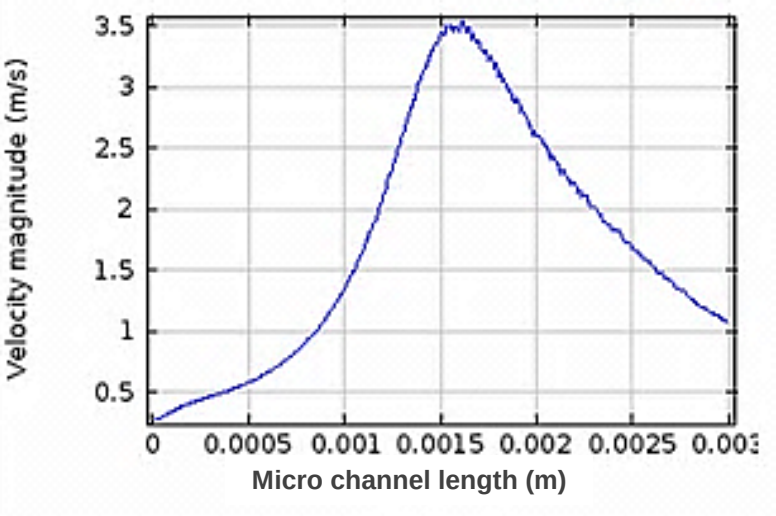

Figure 2.8. Velocity distribution of sinusoidal-shaped wall microchannel with elliptical cross section a=200 µm b=100 µm.

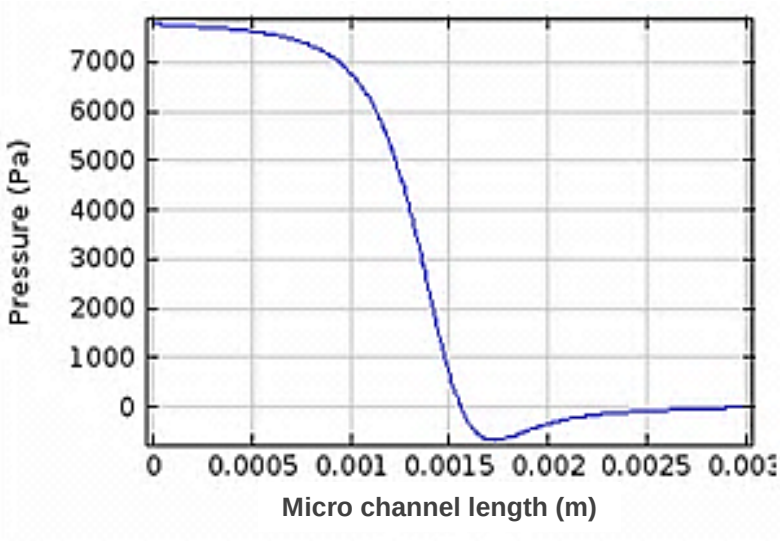

Figure 2.9. Pressure distribution of sinusoidal-shaped wall microchannel with elliptical cross section a=200µm b=100 µm.

2.4. Two-Dimensional Magneto-Fluid-Solid-Interaction (MFSI) Analysis

The CFMFTS propels the fluid via the controllable magnetic actuation by using the induced magnetic force within the solid boundary. The magnetic field is applied on the electromagnet through an external current density. A sphere made of air is modeled for encapsulation of the entire system. The electromagnet generates a magnetic field strength domain, $\boldsymbol{H}$ which is calculated from the Ampere's law in time dependent form:

$$\sigma\frac{\partial \boldsymbol{A}}{\partial t} + \boldsymbol{\nabla} \times \boldsymbol{H} = \boldsymbol{J} \tag{2.2}$$

where σ is the electrical conductivity, $\boldsymbol{A}$ is the magnetic vector potential and $\boldsymbol{J}$ is the external current density which is calculated from:

$$\boldsymbol{J} = \sigma \mathbf{v} \times \boldsymbol{B} + \boldsymbol{J}^{e} \tag{2.3}$$

where J^{e} is the external current density and $\mathbf{v}$ is the velocity of conductor. Magnetic field density, $\boldsymbol{B}$ is calculated from:

$$\boldsymbol{B} = \boldsymbol{\nabla} \times \boldsymbol{A} \tag{2.4}$$

where A is the magnetic vector potential. The constitutive equation is:

$$\mathbf{B} = \mu_0(\boldsymbol{H} + \boldsymbol{M}) \tag{2.5}$$

where μ_0 is the permeability of the free space and **M** is the magnetization vector. Replacing **B** and $\boldsymbol{J}$ in Ampere's law gives:

$$\boldsymbol{J^e} = \sigma\frac{\partial \boldsymbol{A}}{\partial t} + \boldsymbol{\nabla} \times (\mu_0^{-1}\boldsymbol{\nabla} \times \boldsymbol{A} - \boldsymbol{M}) - \sigma\mathbf{v} \times (\boldsymbol{\nabla} \times \boldsymbol{A}) \tag{2.6}$$

Magnetic force is applied using Maxwell stress which is defined as:

$$\boldsymbol{n}.\sigma_{maxwell} = -0.5\boldsymbol{n}(\boldsymbol{H}.\boldsymbol{B}) + (\boldsymbol{n}.\boldsymbol{H})\boldsymbol{B}^T \tag{2.7}$$

where n is the normal vector in the outward direction of the magnetic domain surface. Total stress in the solid domain is the result of fluid pressure and magnetic stress as follows:

$$\sigma_{total} = \sigma_m + \sigma_p \tag{2.8}$$

Magnetic actuation of the SMREM is investigated in this section through numerical modeling of the CFMFTS system. Although the effect of magnetic field on the proposed CFMFTS system causes a 3D deflection but a simplified 2Dmodel can facilitate understanding of the mechanism. A fully coupled solver is used for this study. Figure 2.10 shows a sample error analysis with respect to Newton-Raphson iterations which is $u^{i+1} - u^i$. The average error of this numerical analysis is 4×10^{-4}. Figure 2.11 shows the discretization of the two-dimensional micropump. There are 5,114 domain elements, 588 boundary elements and a total of 19,125 degrees of freedom solved for.

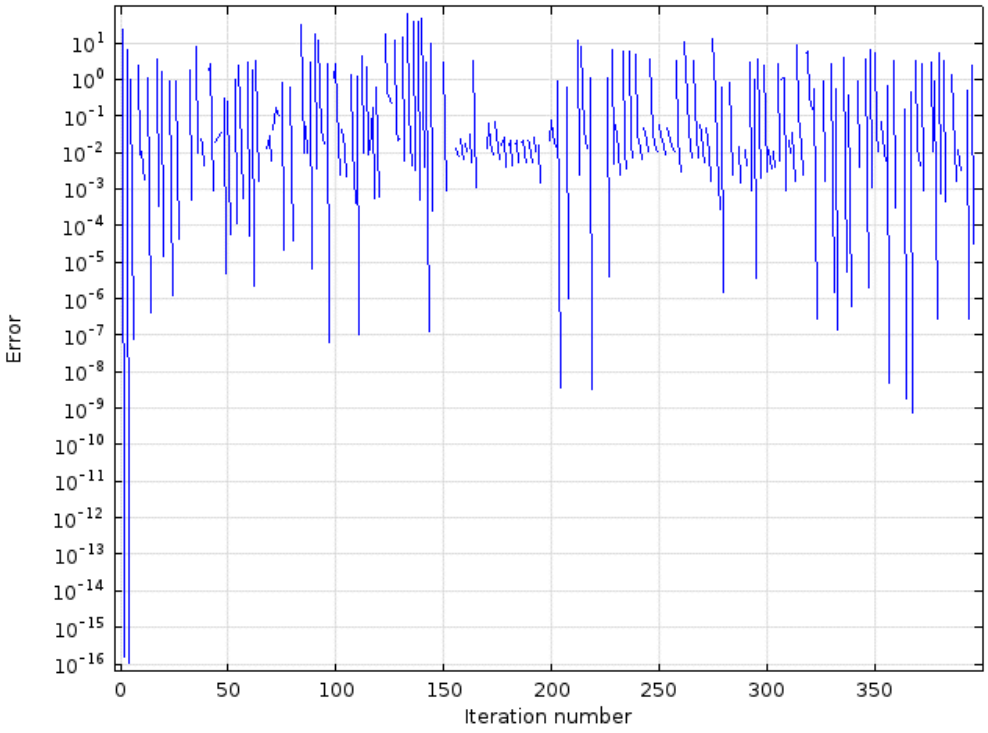

Figure 2.10. Sample error of finite elemnt analysis.

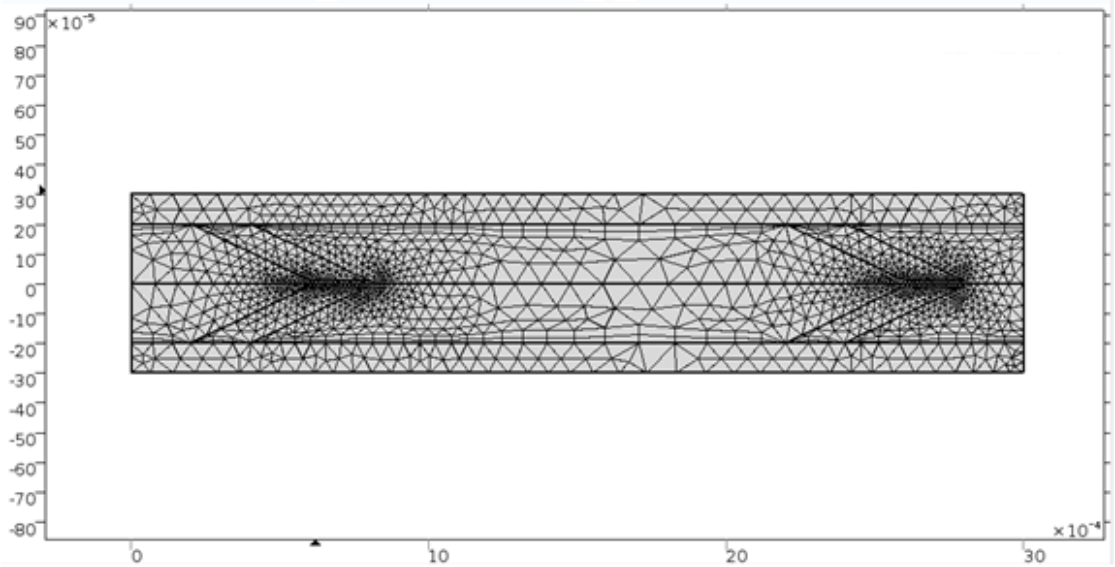

Figure 2.11. A sample meshing for the 2D finite element analysis.

The magnetic flux density distribution generated inside the wall of the micropump is shown in Figure 2.12. Figure 2.13 demonstrates the magnetic field in the top wall of the micropump. Since the shape of the microchannel is not symmetric with respect to the y axis, magnetic field distribution is not completely symmetric and the distribution of the magnetic field is not uniform. With the SMREM microchannel placed 2.5 mm above the top of the electromagnet, an average of 0.037 T magnetic field density is generated, which results in the deflection of the microchannel.

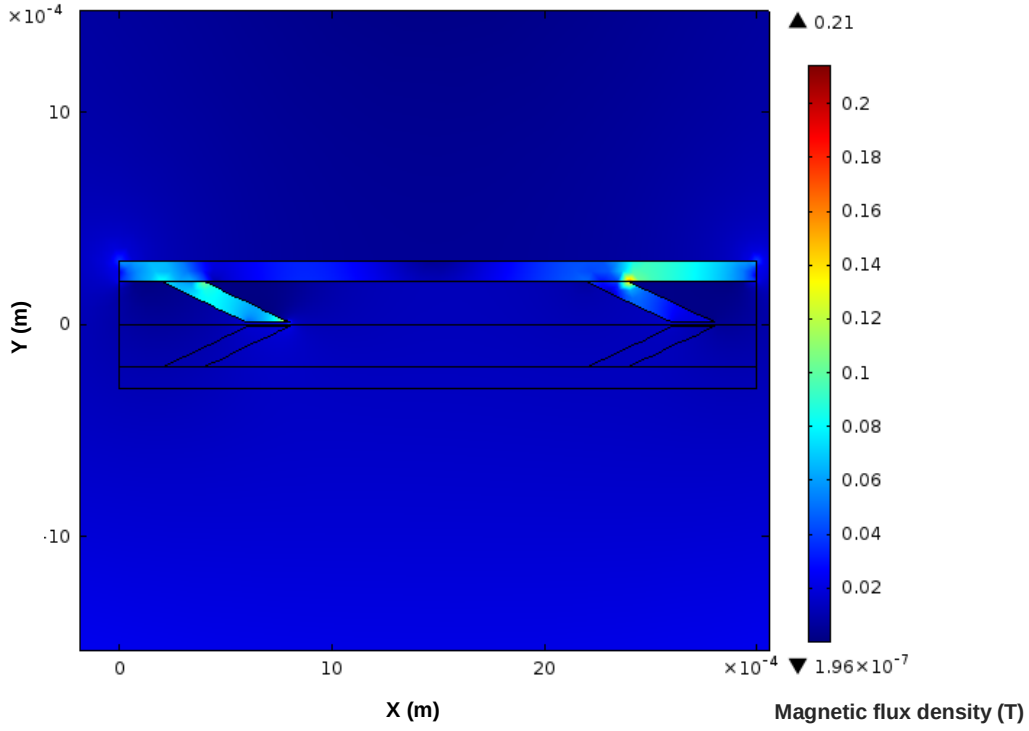

Figure 2.12. Distribution of magnetic flux density inside SMREM microchannel.

To analyze the performance of this system, magnetic, fluid, and structural modules along with the Arbitrary Lagrangian-Eulerian module were utilized to combine the effect of moving solid boundary on the boundary with the fluid. The Arbitrary Lagrangian-Eulerian moving mesh method is used to simulate the fluid-solid interaction. To exanime the net flow generated by the system, the input velocity is considered zero and the velocity generated due to the external magnetic load on the boundary is obtaineded. Load is applied as a time-dependent body force which varies sinusoidally on the top wall of the microchannel for one second. Spring foundation is applied to the top and bottom of microchannel.

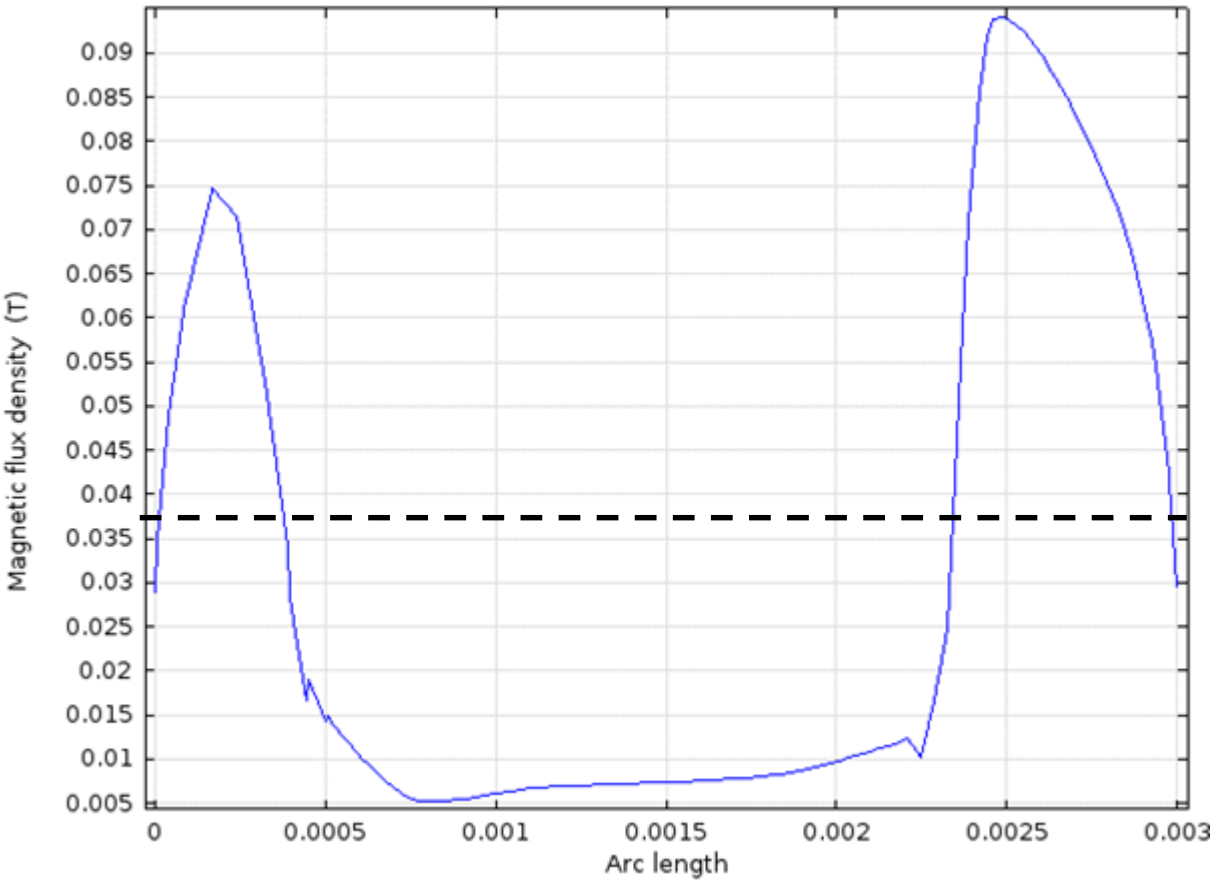

Figure 2.13. Distribution of magnetic flux density inside SMREM microchannel.

Figure 2.14 demonstrates the fluid velocity generated and the solid boundary displacement at t=0.25s, which corresponds to the maximum velocity. The modeled microchannel has the width of 3 mm, microchannel inner width of 400µ and the wall thickness of 100µ. Large deformation is considered for this analysis. Since the input velocity is zero, the amount of flow that is passing through the outlet depends only on the deformation of the solid domain. As can be seen in Figure Figure 2.15 the maximum flow rate occurs before 0.1s and the flow returns to the microchannel as the solid boundary retracts to original position. Figure 2.16 demonstrates the amount of fluid volume pumped at each time.

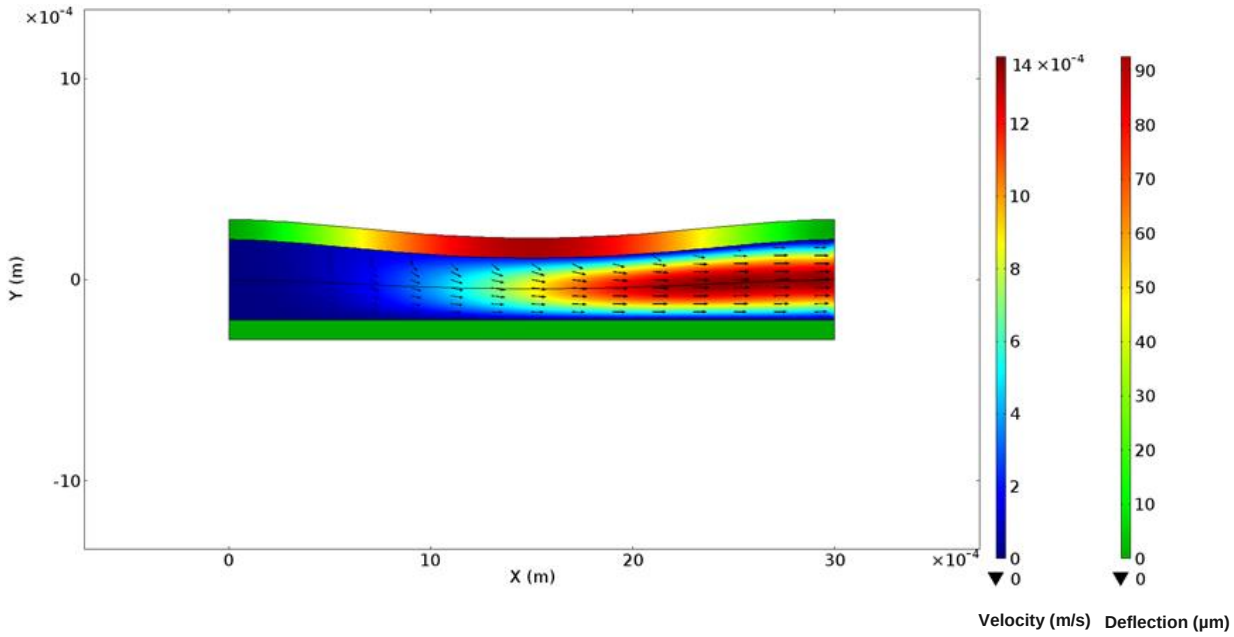

Figure 2.14. Fluid propulsion with zero input velocity.

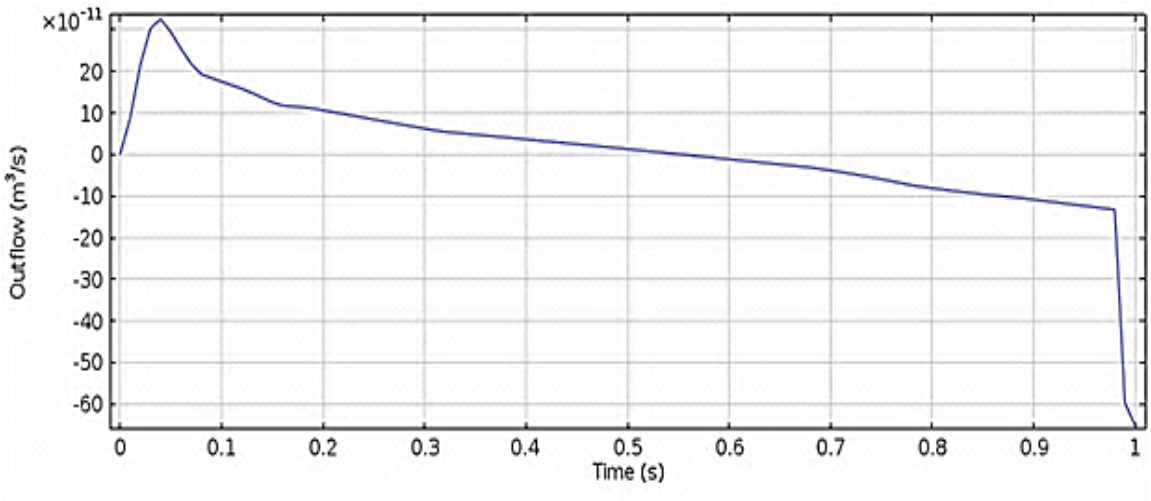

Figure 2.15. The rate of outflow for micropump without valve.

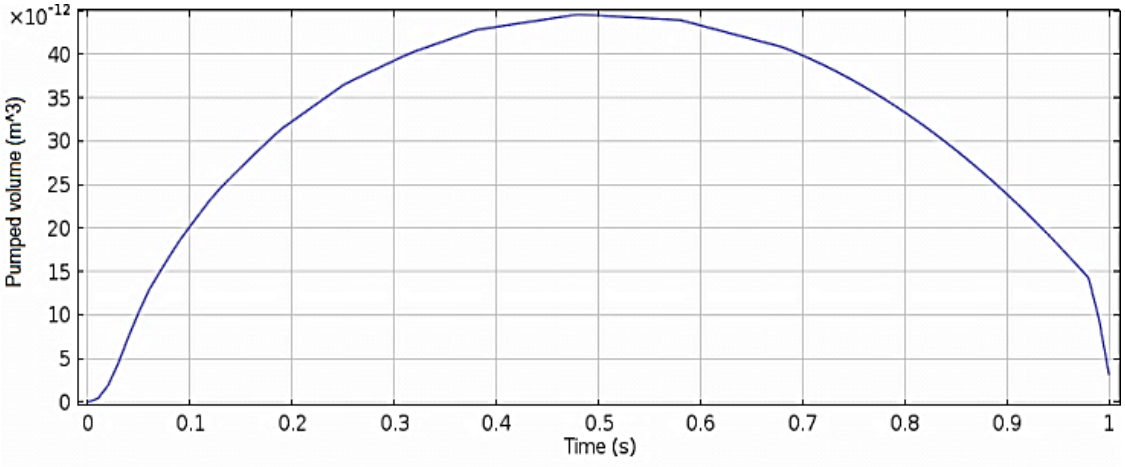

Figure 2.16. The volume of transferred fluid vs. time for micropump without valve.

As the microchannel retracts, the transferred flow returns to the microchannel due to the negative pressure. To prevent the fluid returning to the microchannel, two conical valves are implemented which are presented in Figure 2.17. Adding the valves increases the maximum velocity at the t=0.25 (s) since they reduce the fluid transfer cross section.

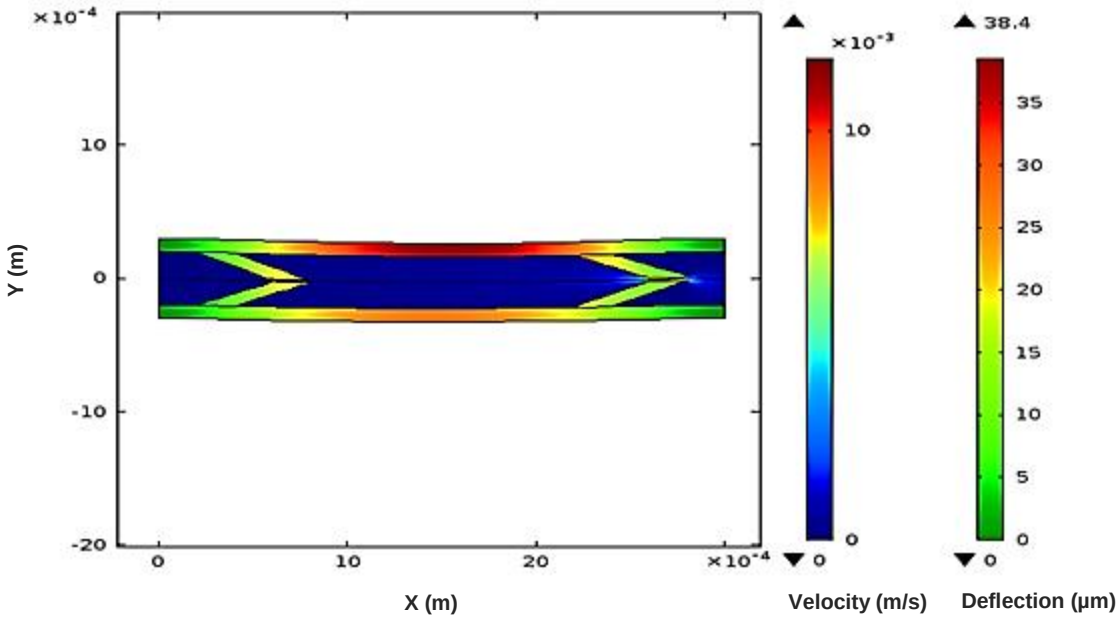

Figure 2.17. Fluid propulsion with zero input velocity.

Figure 2.18 demonstrate the flow rate and Figure 2.19 shows the total volume of fluid transported by the microchannel with two valves. From Figure 2.18 it can be seen that the backward flow rate reduces significantly by the adding the valves. Also, Figure 2.19 shows that adding valves produces a *net flow transferred to the right* as opposed to Figure 2.16 in which all of the transferred flow returns to the micropump as a result of retraction.

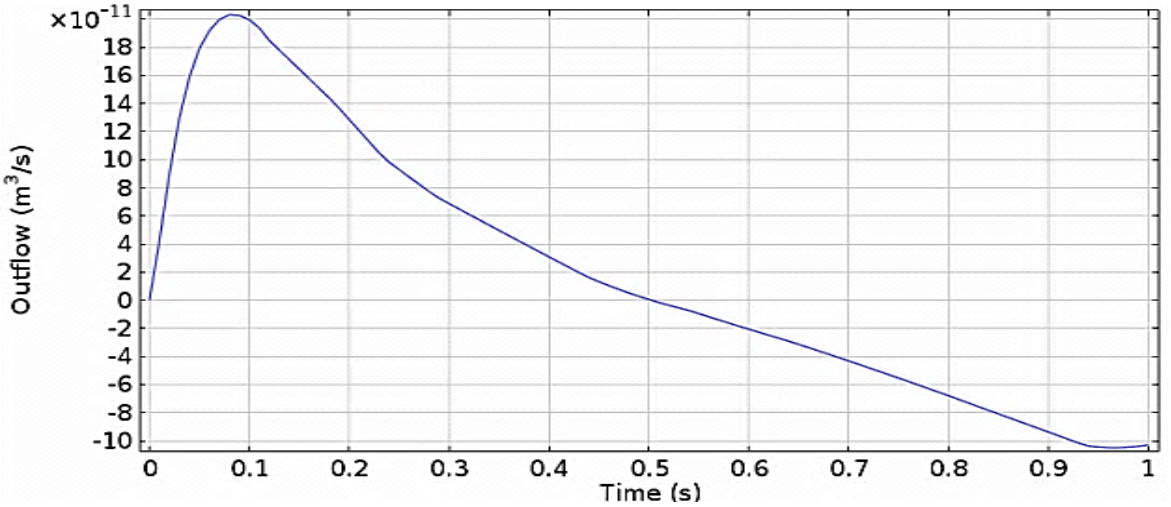

Figure 2.18. The rate of outflow at each time for micropump with valve.

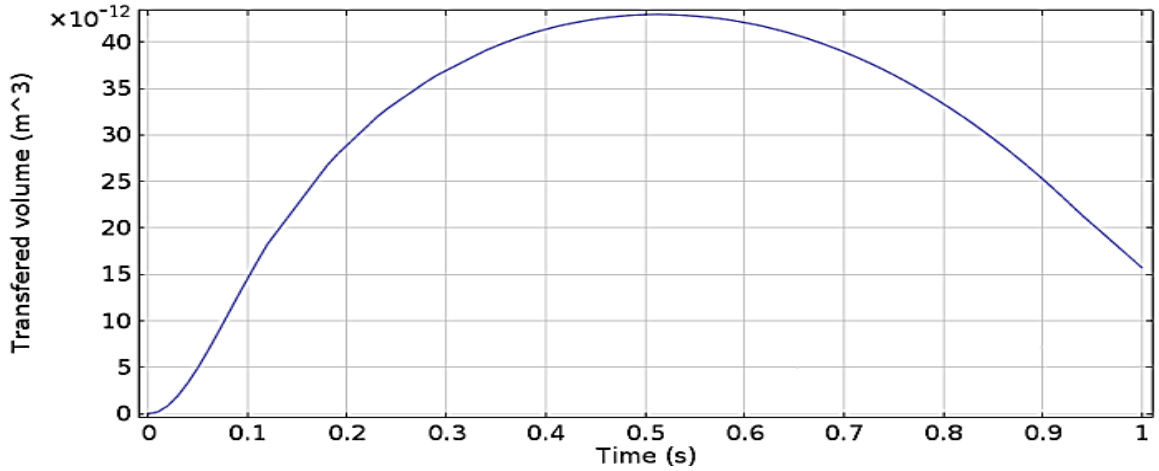

Figure 2.19. History of the vomule of pumped fluid for microchannel without valve.

Figure 2.20 demonstrates the deflection of the microchannel and the valve at 0.1 s increments. In all figures, left bar is the deflection in Micron and right bar is the velocity in m/s. As the mgnetic field increases with a sinosuidal function, deflection in the microchannel increases and thus the velocity of the fluid increases up to 0.5 s. Then, as the channel retracts,

the flow velocity decreases. In the next section, different system parameters are investigated numerically to observe their effect on the net flow.

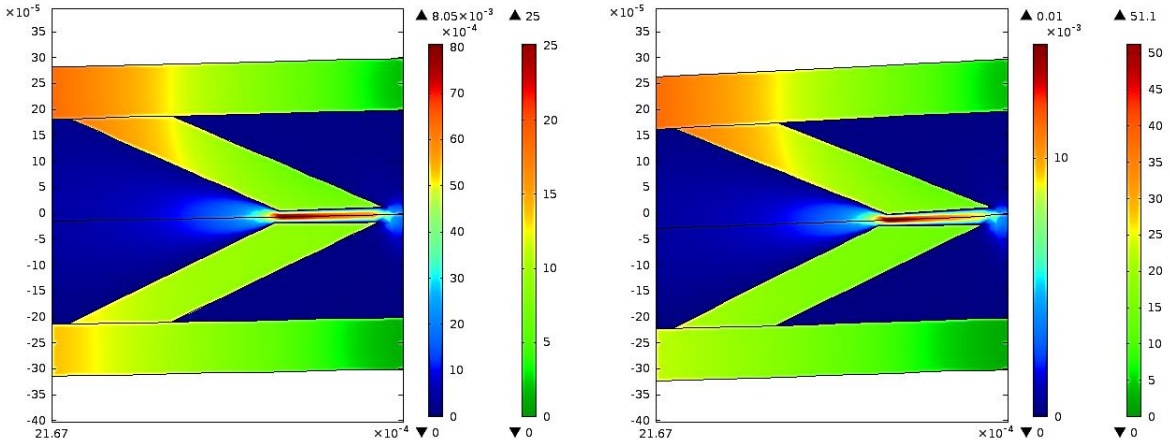

t=0.1 s

t=0.2 s

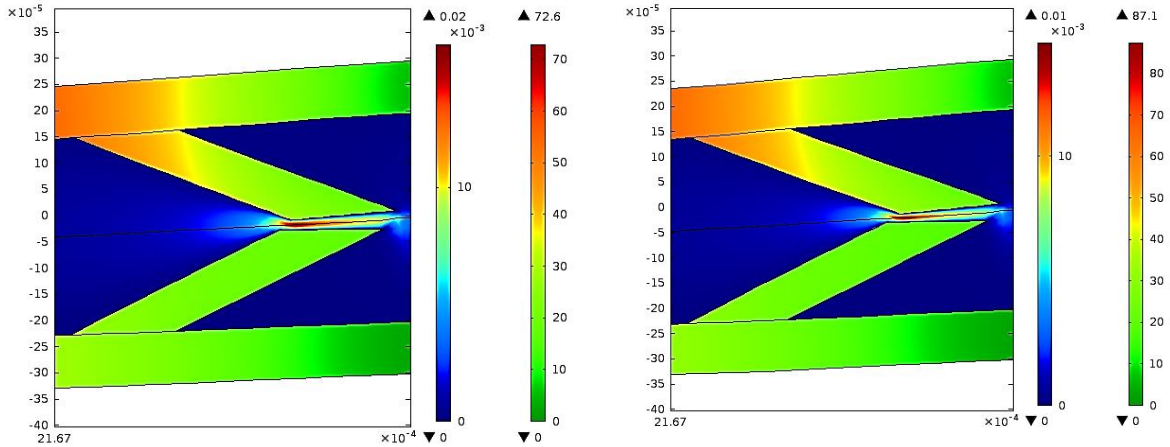

t=0.3 s

t=0.4 s

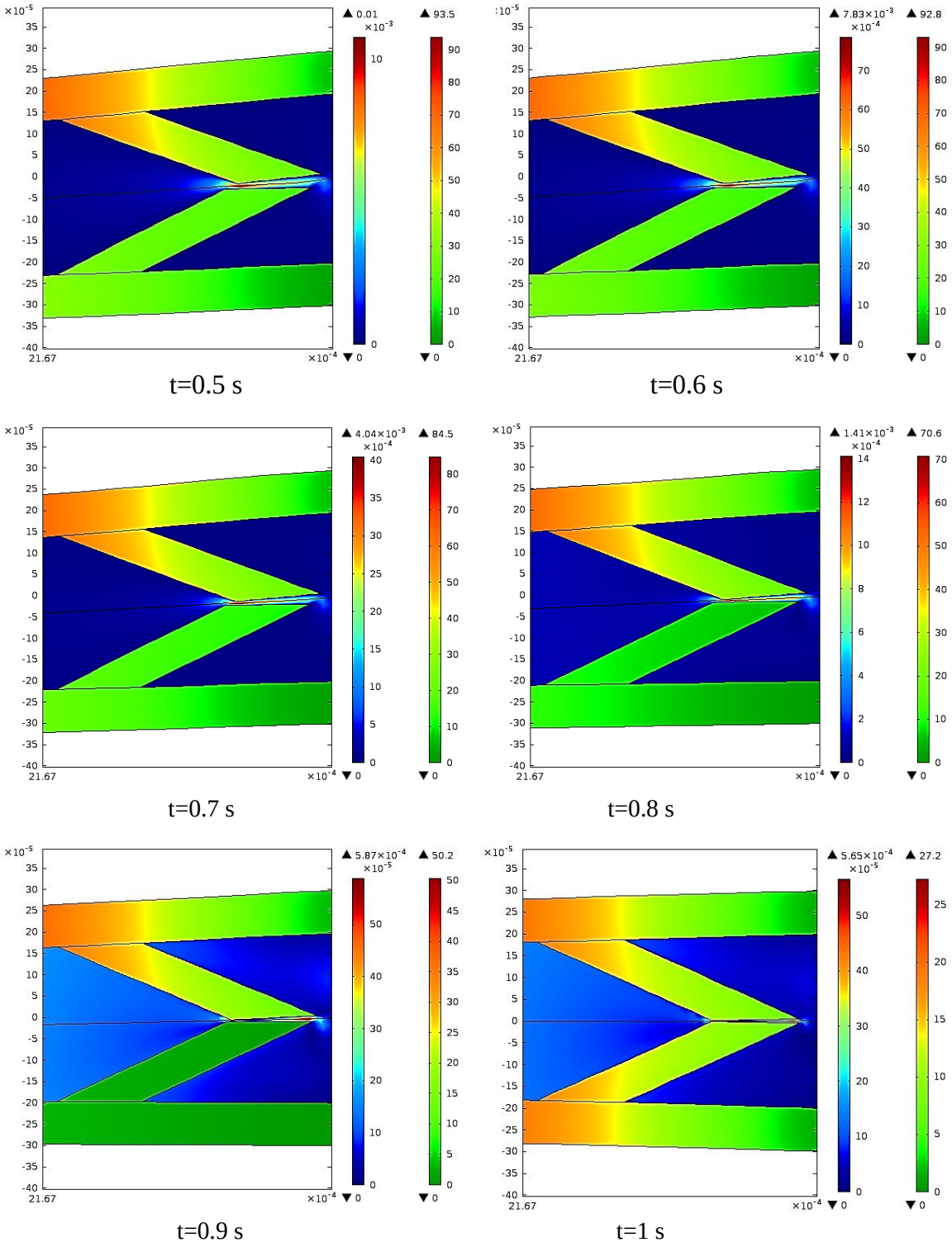

Figure 2.20. Deflection of the micropump at different times dring a cycle.

2.5. Parametric Two-Dimensional Analysis

The amount of transported volume of fluid depends on different geometrical and non-geometrical properties such as material properties of the solid and fluid domain, microchannel geometry, valve geometry and applied magnetic field. Studying system parameters provides an understanding of the effect of each parameter on the performance of the system. To examine such effects on the transferred flow, each parameter is individually varied while others are kept constant. In Figure 2.21 to Figure 2.29, solid line represents the results of numerical modeling while dashed line is the curve fitting. Curve fitting equation is shown inside the graph.

First, geometric parameters, such as, the microchannel and valves are numerically studied. It is demonstrated that when the channel diameter increases, the amount of encapsulated fluid increases. In addition, larger SMREM area results in larger magnetic force. Therefore, when magnetic field and other parameters are kept constant and channel diameter is increased, net transferred flow increases rapidly as illustrated in Figure 2.21.

Valves geometry and location play a key role in the performance of the proposed system especially since the valves are flexible. Figure 2.22 shows how length of the valves affects the net transferred volume of fluid. With larger valve length, the net transferred flow decreases. Larger valve length in 2D analysis attributes to an increased outflow friction between fluid and valve wall, and thus reduces the net flow.

Figure 2.23 illustrate that total flow decreases with a parabolic relation with valve opening but it reaches a certain value as the opening approaches zero. When the valve opening is wide, there is less resistance on the fluid, therefore, net flow decreases.

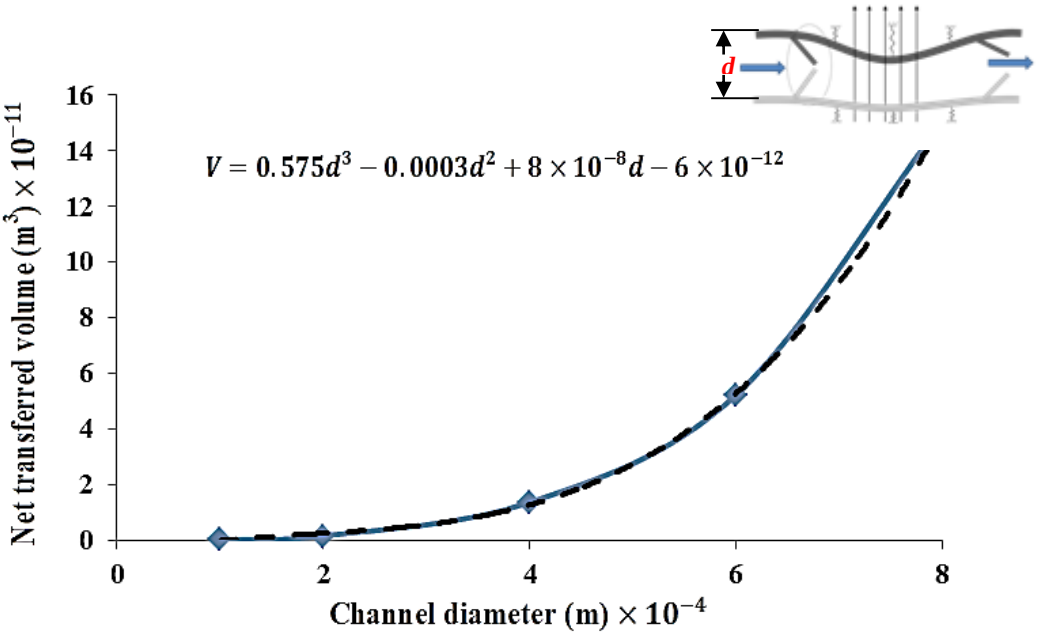

Figure 2.21. Effect of micropump diameter on the fluid flow.

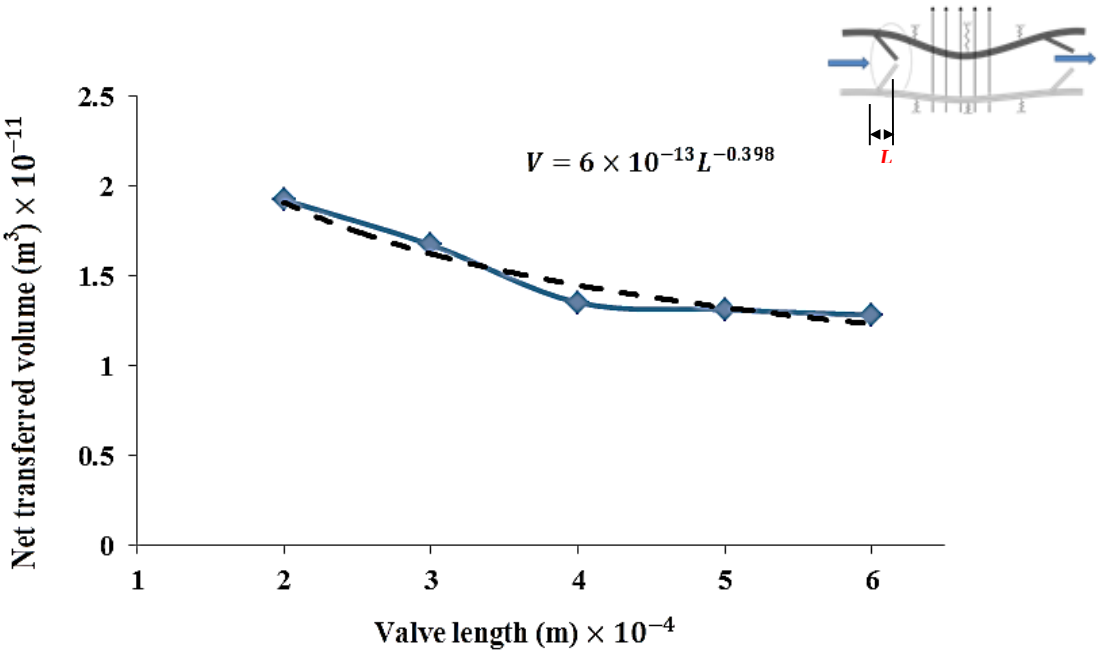

Figure 2.22. Effect of valve length on the fluid flow.

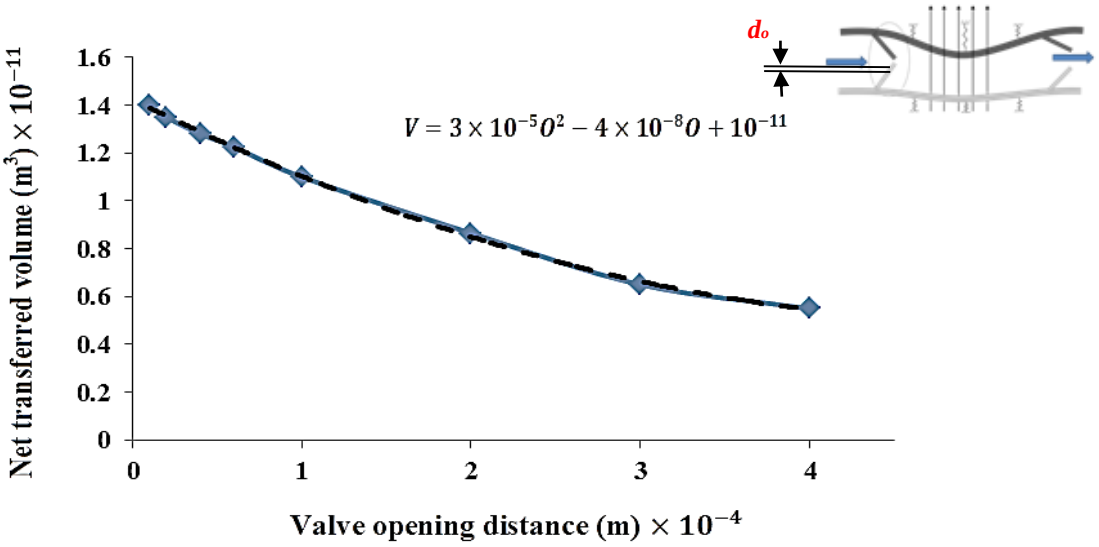

Figure 2.23. Effect of valve opening distance on the fluid flow.

Valve spacing also affects the final pumped flow and as valve spacing decreases, the flow also decreases with a logarithmic function as shown in Figure 2.24. This is due to larger encapsulated fluid between valves when the valves are farther from each other.

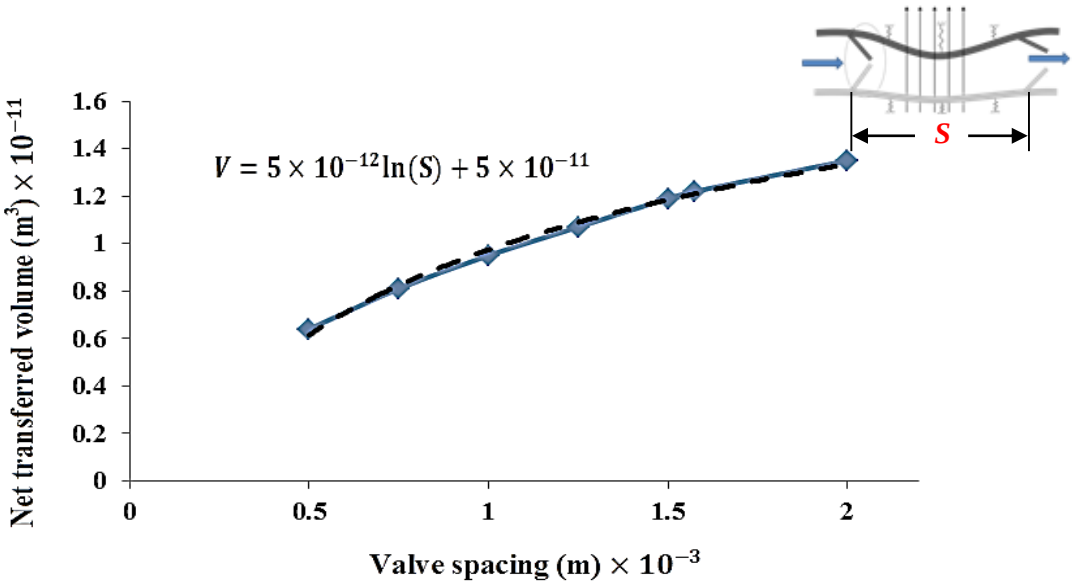

Figure 2.24. Effect of valve spacing on the fluid flow.

Next, mechanical and magnetic properties of the microchannel are studied. Elastic modulus the microchannel, and the spring constant of the elastic foundation affects the performance of the system. Figure 2.25 displays that for elastic modulus of 1 MPa or higher the microchannel becomes very stiff and cannot deflect enough to propel the fluid. Elastic foundation can also affect the results. A very stiff foundation would not let the deflection of microchannel.

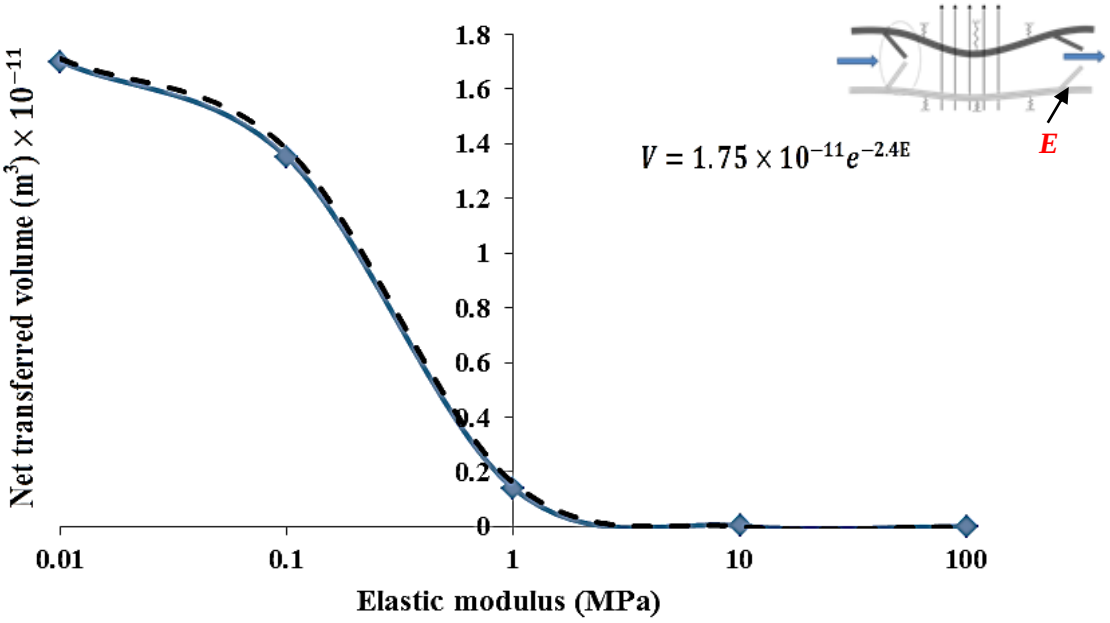

Figure 2.25. Effect of elastic modulus on flow.

To observe the effect of elastic foundation on the performance of the system it has been varied from zero to that of a rigid base. Figure 2.26 indicates that the rigid foundation reduces the deflection of the bottom part in 2D analysis, and therefore, increases the squeezing and the performance. The performance does not change significantly for up to 5 (kN/m.m^2). An exponential function can express the behavior of elastic foundation. It is shown that a transition

period occurs from 10 to 800 (kN/m.m^2) where the elastic foundation becomes very stiff that the magnetic force cannot deflect the channel and net flow approaches zero.

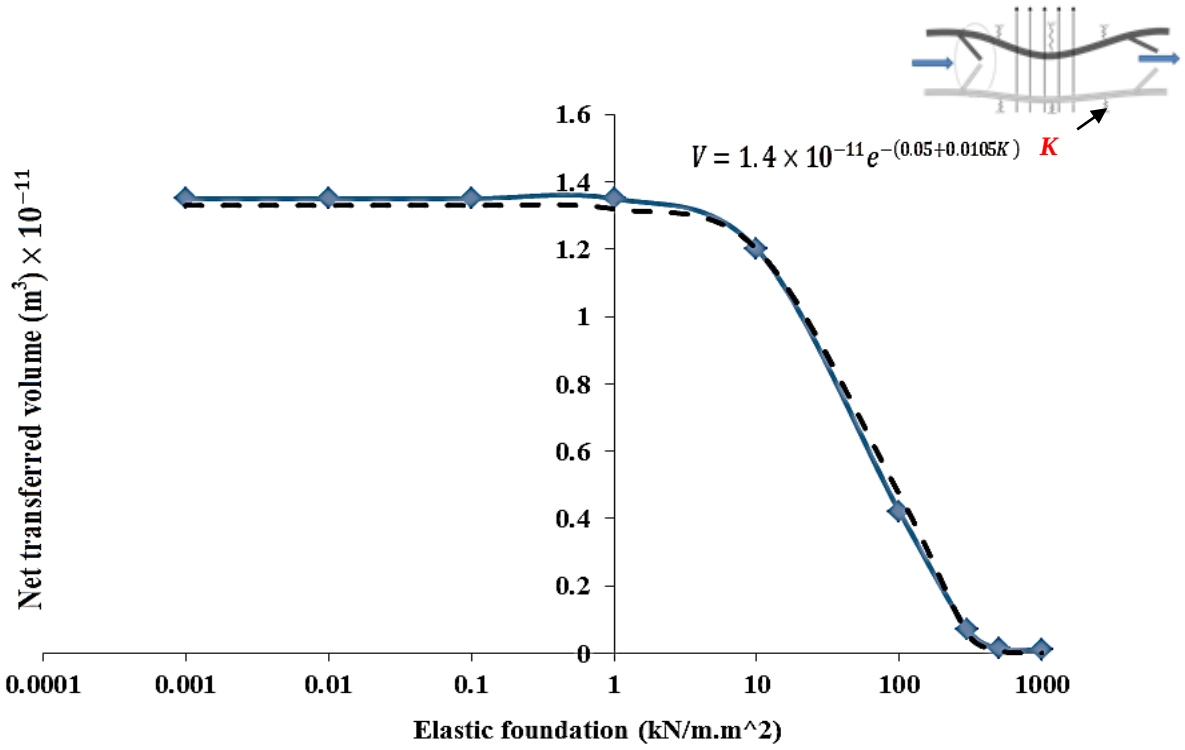

Figure 2.26. Effect of elastic foundation on the fluid flow.

Fluid viscosity also affects the total amount of fluid pumped by the system which can be explained with a polynomial function as shown in Figure 2.27. As the viscosity of the fluid increases the amount of transferred volume approaches zero. Also, if the viscosity is very low fluid returns to the channel easily and this reduces the net flow. However, there is an optimum value for the fluid viscosity which is determined to be equal to 0.02.

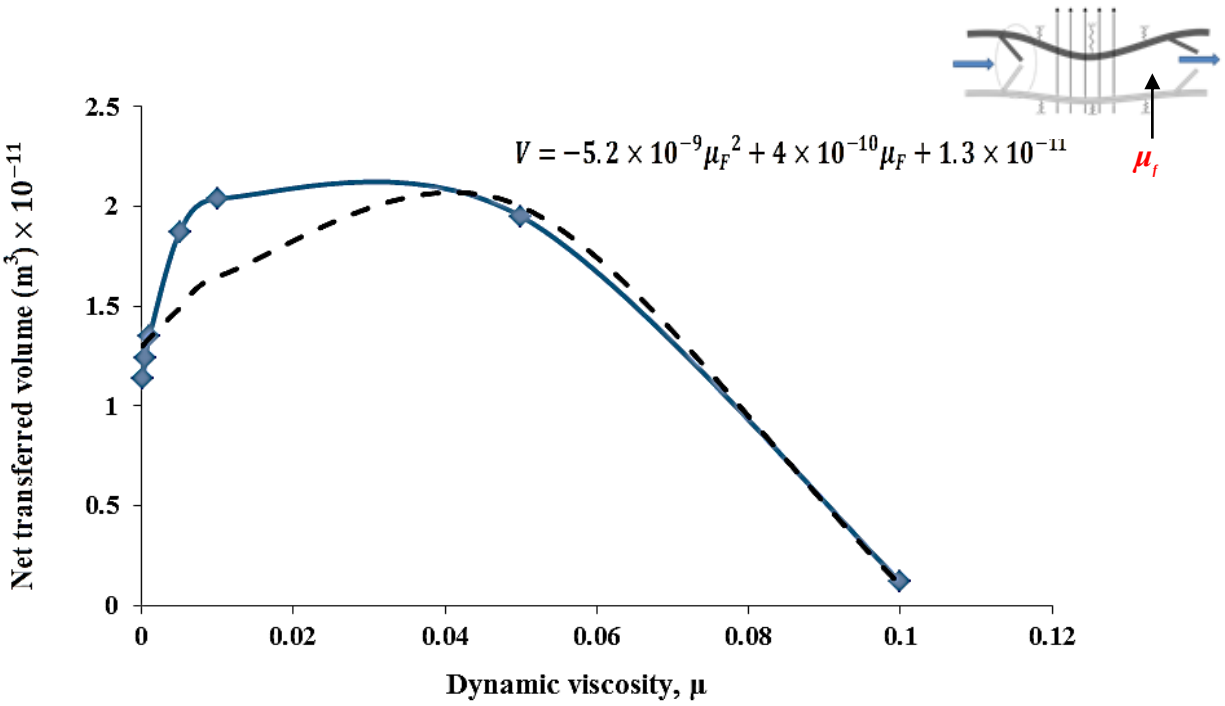

Figure 2.27. Effect of fluid viscosity on the fluid flow.

Magnetic force is applied to the microchannel using an electromagnet. Therefore, characteristics of the electromagnet and magnetic properties of the SMREM can also change the performance of the system. Figure 2.28 demonstrates the pumped fluid increases with applied magnetic field since larger magnetic field is associated with more squeezing of the channel. But, net flow reaches a plateau since the amount of encapsulated fluid in the microchannel is limited.

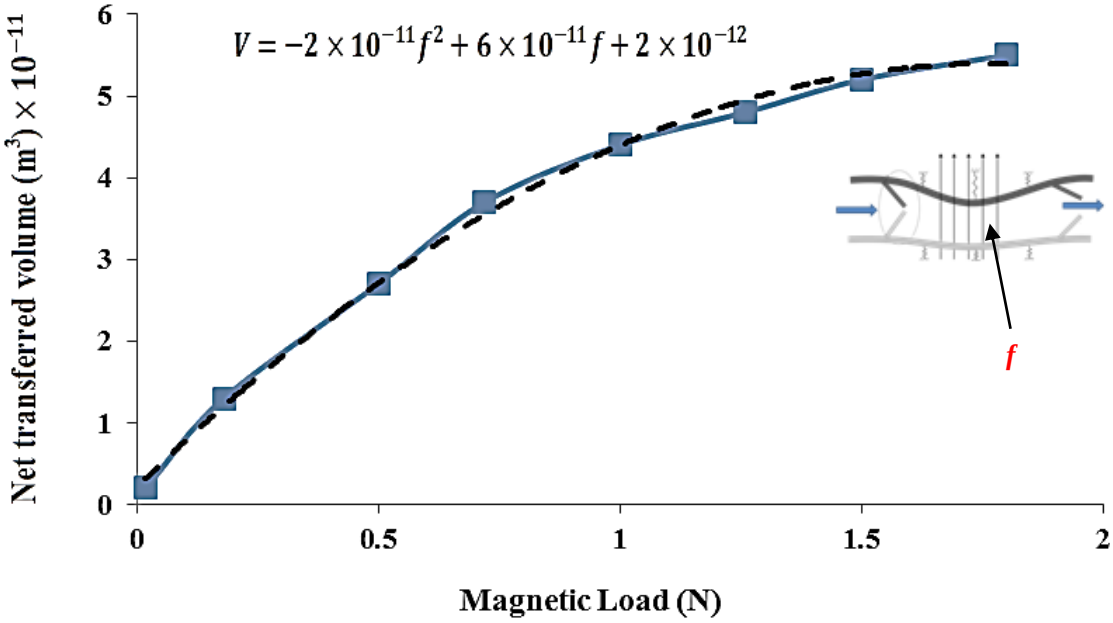

Figure 2.28. Effect of electromagnetic load on the fluid flow.

A macro-mechanics model is used for magnetic properties of MRE i.e. bulk properties for the MRE is considered with magnetic permeability of μ. Figure 2.29 demonstrates the effect of magnetic permeability of the total pumped volume which can be defined with a logarithmic load. SMREM with smaller magnetic permeability will results in less magnetic force and less deflection. However it shows after magnetic permeability of 500 the performance does not significantly change since the SMREM approaches saturation.

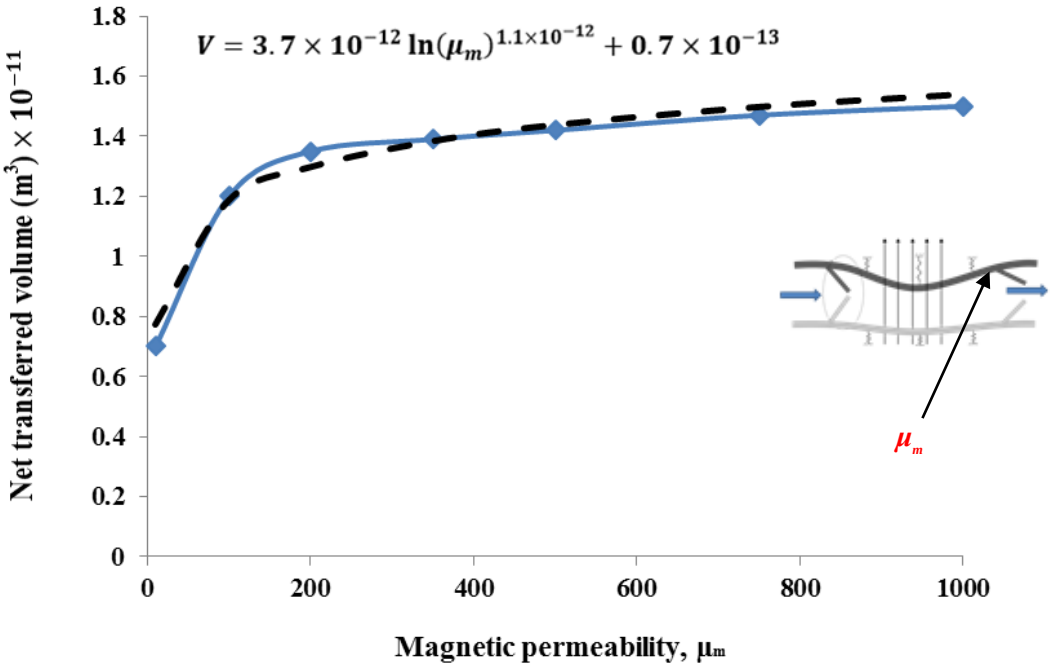

Figure 2.29. Effect of magnetic permeability on the fluid flow.

2.6. Three-Dimensional Analysis

Although 2D analysis gives significant insight into the problem, the actual deflection of the microchannel is non-symmetrical. Moreover the effect of elastic foundation and magnetic field are different in 3D analysis. Therefore, the 3D finite element analyses are vital to investigate the difference between the 2D and 3D results. To achieve this goal the magnetic fluid solid interaction problem is modeled three dimensionally to consider the effect of non-symmetrical deflection of the microchannel and magnetic field on the performance of the system.

To perform analysis of the contracting microchannel, electromagnetic module, fluid module, structural module and Arbitrary Lagrangian - Eulerian (ALE) module are used. ALE enables us to consider the effect of moving solid boundary on the fluid domain. Similar to 2D

analysis, fluid is considered stagnant at microchannel entrance and on the outlet, the fluid is discharged to atmospheric pressure. The force that is generated by the magnetic field squeezes the microchannel. Figure 2.30 illustrates the amount of magnetic field generated inside MRE micropump. Figure 2.31 demonstrates the average value of the magnetic field inside the wall of the micropump, which has an average value of 0.057 T.

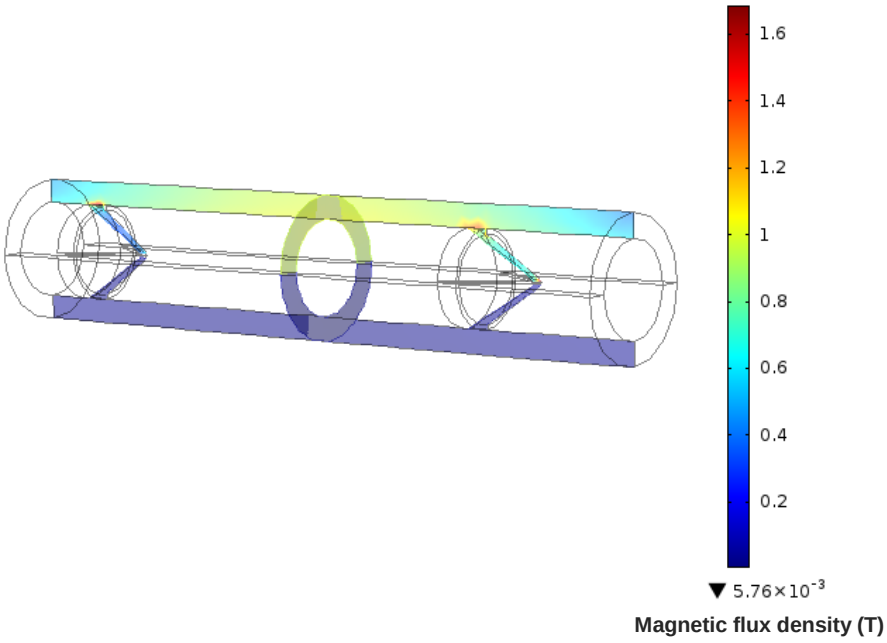

Figure 2.30. Induced magnetic field in the flexible micropump.

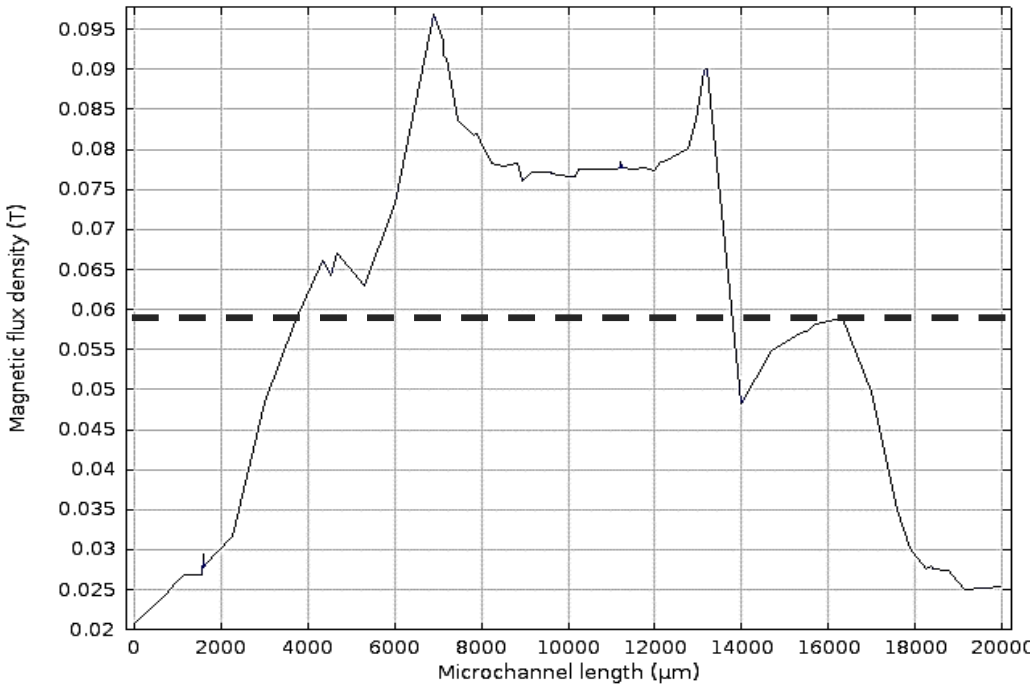

Figure 2.31. Magnetic flux density along the wall of the SMREM micropump.

In one cycle of applying magnetic field, the channel is squeezed to move the fluid. The velocity that is generated in fluid domain is a result of deflection of solid wall. However, as the flexible channel retracts, all of the fluid moves back to the channel. By designing appropriate one-way vales, we can prevent some of the backward movement. This way, a unidirectional flow is generated in the microchannel. The valve flaps open and close due to the outer wall movements. Figure 2.32 shows the 3D design of the CFMFTS with the direction of the magnetic field and top section made of SMREM. The current design of the valves includes four 80-degree flaps. Figure 2.33 shows the generated mesh with 32,757 domain elements, 5,829 boundary elements, and 1,163 edge elements. Figure 2.34 shows a sample of error of numerical analysis of the fully coupled non-linear solver which has an average value of 0.001.

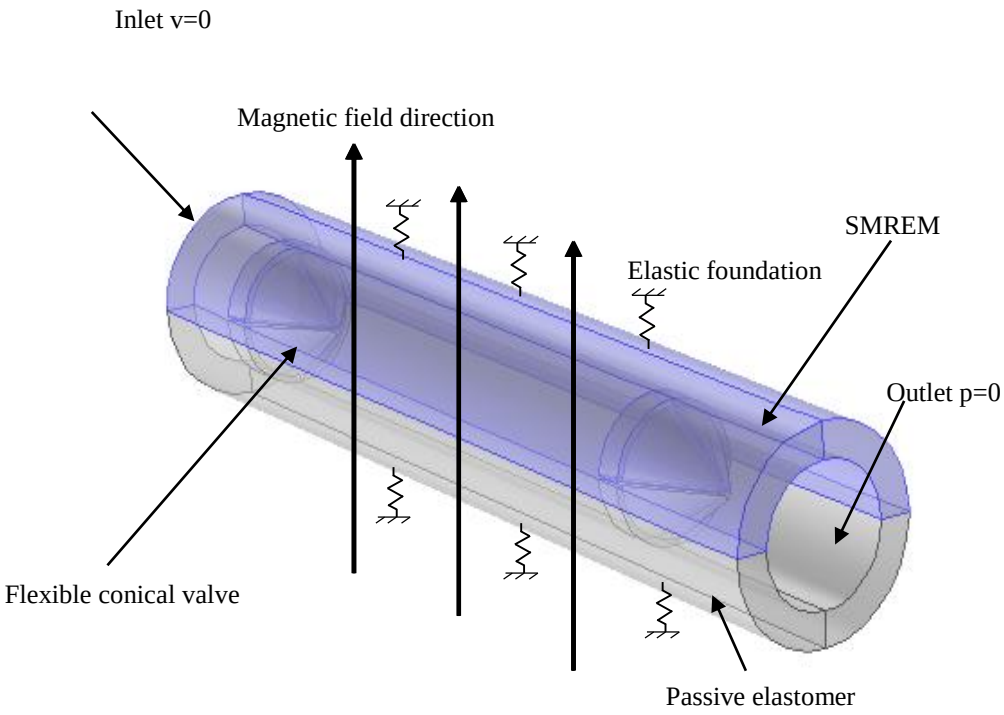

Figure 2.32. Three-dimensional model of the CFMFTS.

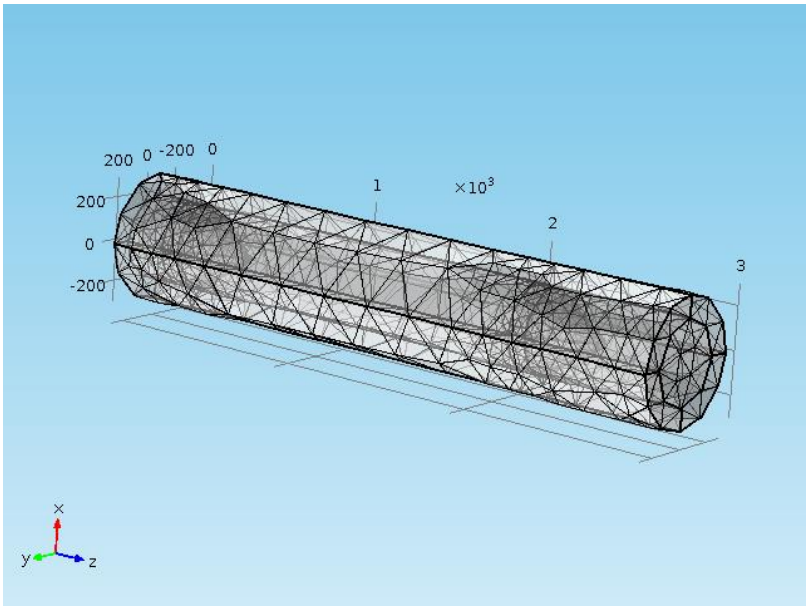

Figure 2.33. Discretization of the CFMFTS.

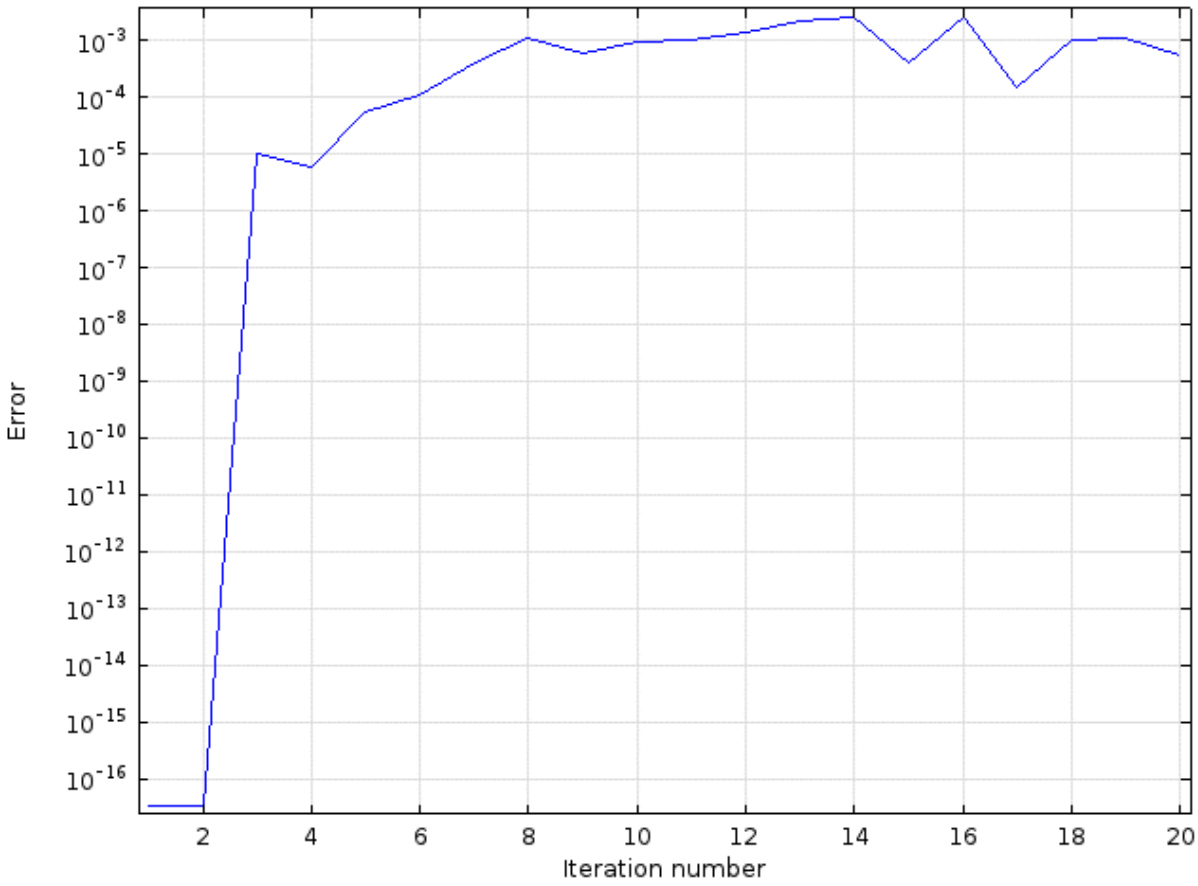

Figure 2.34. Sample error for three-dimensional analysis.

When the magnetic force is applied, the middle section collapses and the positive pressure generated in this section opens the right valve and closes the left valve. At around quarter of a cycle, velocity reaches its maximum as shown in Figure 2.35 at t=0.31s.

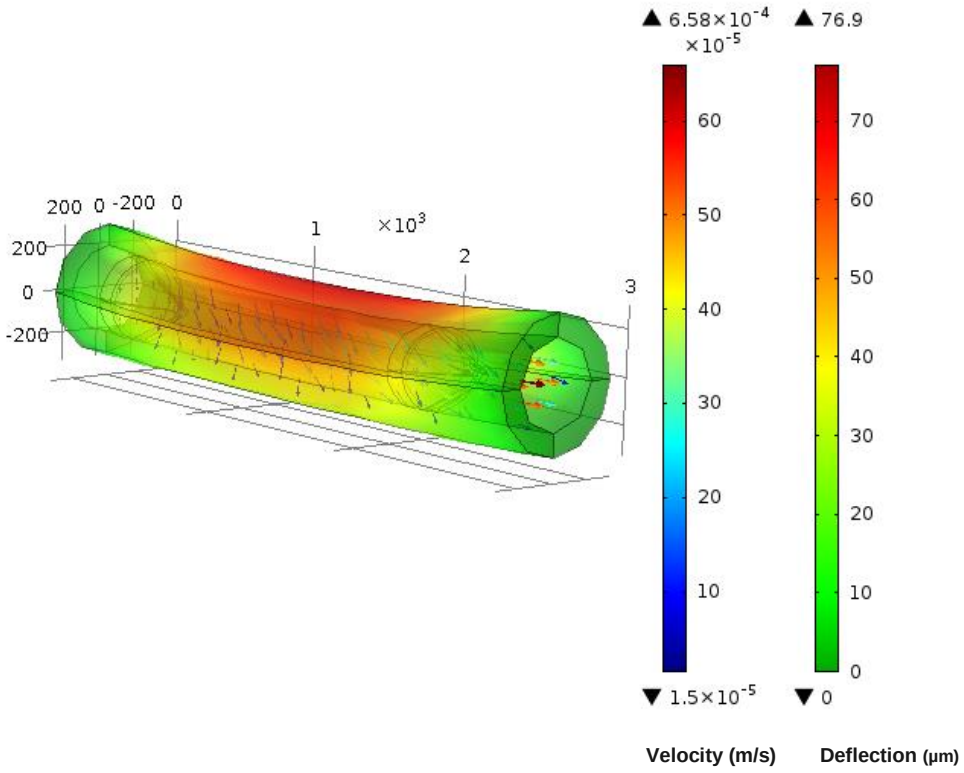

Figure 2.35. Velocity and deflection of MR micropump at maximum fluid velocity.

Figure 2.36 shows the rate of flow during one cycle. The maximum outflow is reached at t=0.32s but the maximum inflow is reached at 0.7s instead of 0.64s. This delay and resistance for the reverse flow generates a net flow. Figure 2.37 demonstrates the total volume of fluid pumped at each moment which is obtained by integrating velocity over the outlet area. It is shown that using flexible valves generate net flow, since a positive value of pumped fluid is generated at the end of the cycle.

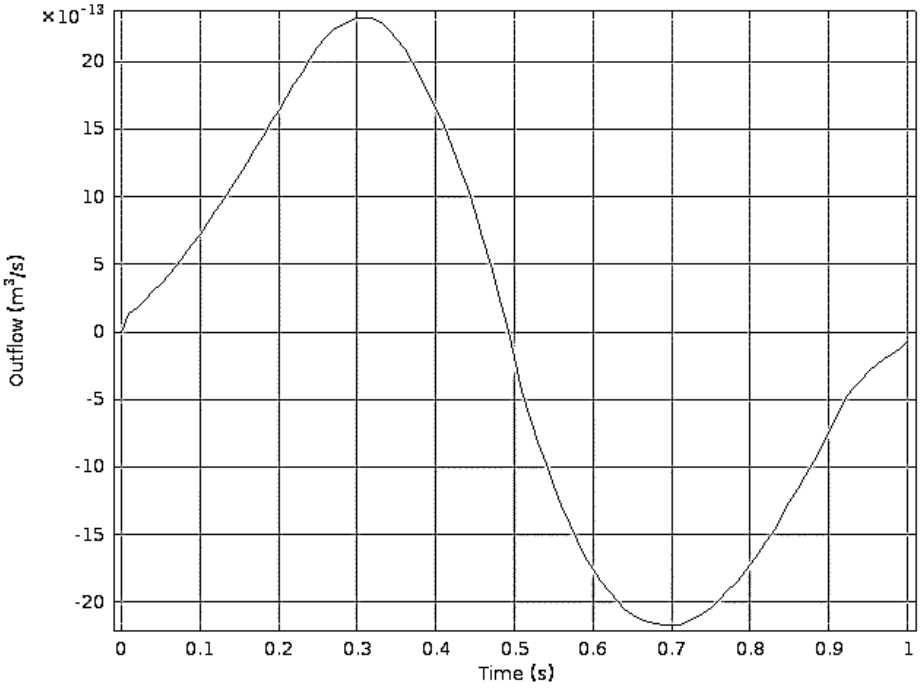

Figure 2.36. Rate of the flow during one cycle.

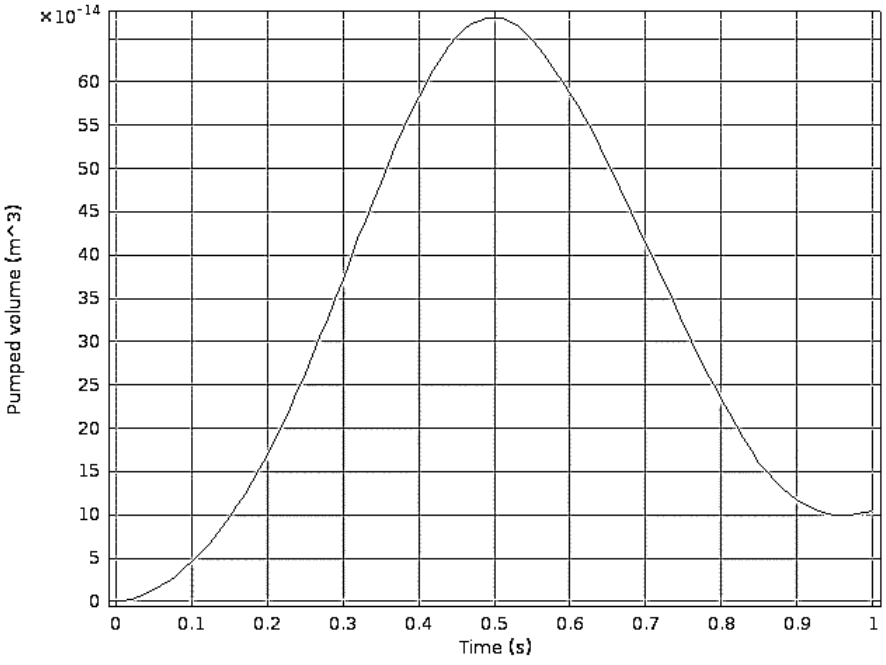

Figure 2.37. Total pumped fluid during one cycle.

2.7. Parametric Three-Dimensional Analysis

Similar to two-dimensional analysis, a parametric study is performed on the three 3D model of the CFMFTS. In this model, magnetic field is applied using an electromagnet and the magnetic field is induced inside SMREM part of the microchannel. The magnetic force of SMREM compresses the microchannel and pushes the fluid outward. By comparing two- and three-dimensional models, one can decide if the 2D study can accurately, capture performance of the system, or a 3D study is necessary. Different geometrical parameters, mechanical properties and magnetic properties are studied using the 3D model. The volume of transported fluid corresponding to each parameter is investigated. In Figure 2.38-Figure 2.46 solid line represents the numerical modeling results and dashed line represents the curve fitting. Curve fitting equation is also shown in the figures.

The microchannel has a 3D deflection, therefore, geometric parameters may show different trend in the 3D analysis. Figure 2.38 shows the effect of channel diameter on the net generated flow. The net transferred flow increases for larger diameters since larger diameter results in larger volume of fluid and larger magnetic force. Similar behavior is observed for the 2D model.

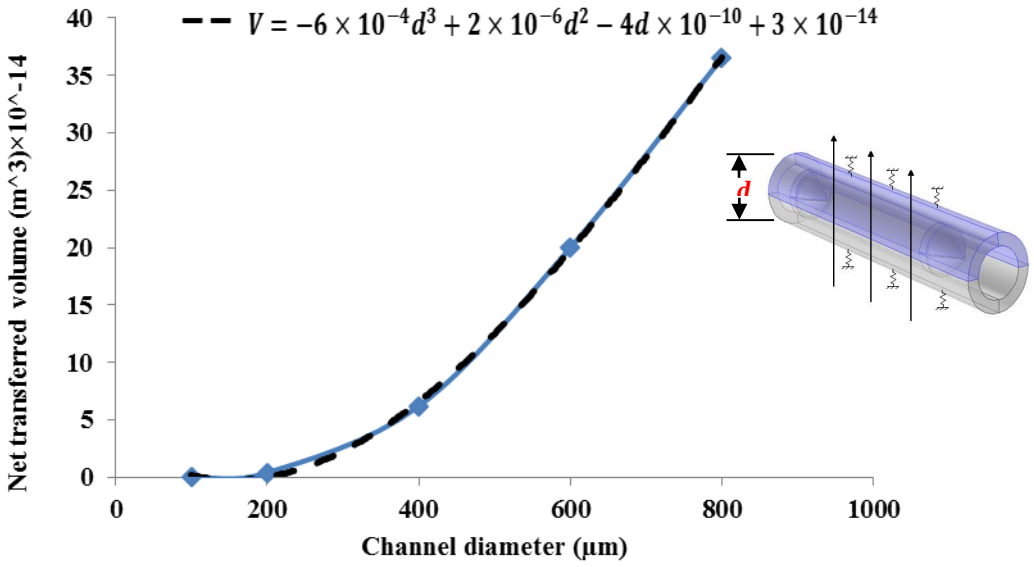

Figure 2.38. Effect of micropump diameter on the fluid flow.

Valves geometry is also varied here similar to the 2D parametric study to examine the effect of 3D deflection. As can be seen from Figure 2.39, unlike the 2D analysis, there is an optimum value for valve length which is about 400µ. Smaller valve length makes the structure stiffer since the valve cannot open and close, effectively. Also larger valve length increases the friction between fluid and valve and, thus decreases the net flow.

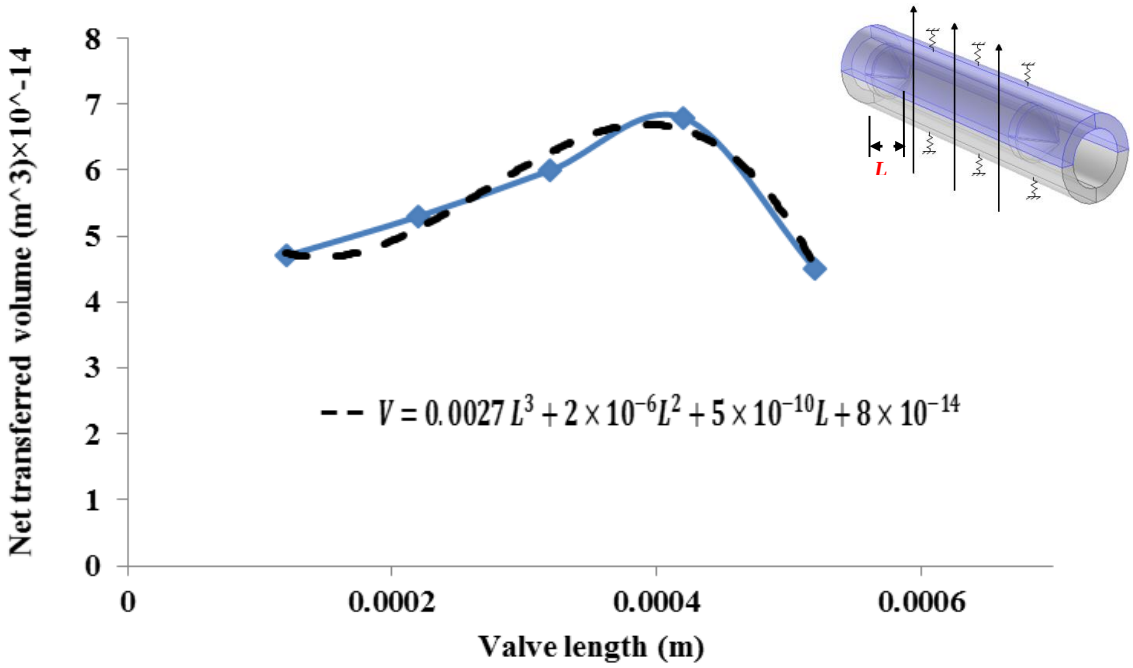

Figure 2.39. Effect of valve length on the fluid flow.

Next, the effect of valve opening diameter on the net flow is investigated. If the opening is very small, there will be less outflow and backflow; thus reducing the total pumped volume of fluid. Also, very large valve opening eliminates the valve functionality. Figure 2.40 illustrate that there is an optimum value for the valve opening which is around 60μ. Valve spacing also affects the final pumped fluid and as valve spacing decreases, the flow also increases for larger distance between two valves since there is larger volume of fluid and larger magnetic force between the two valves as shown in Figure 2.41.

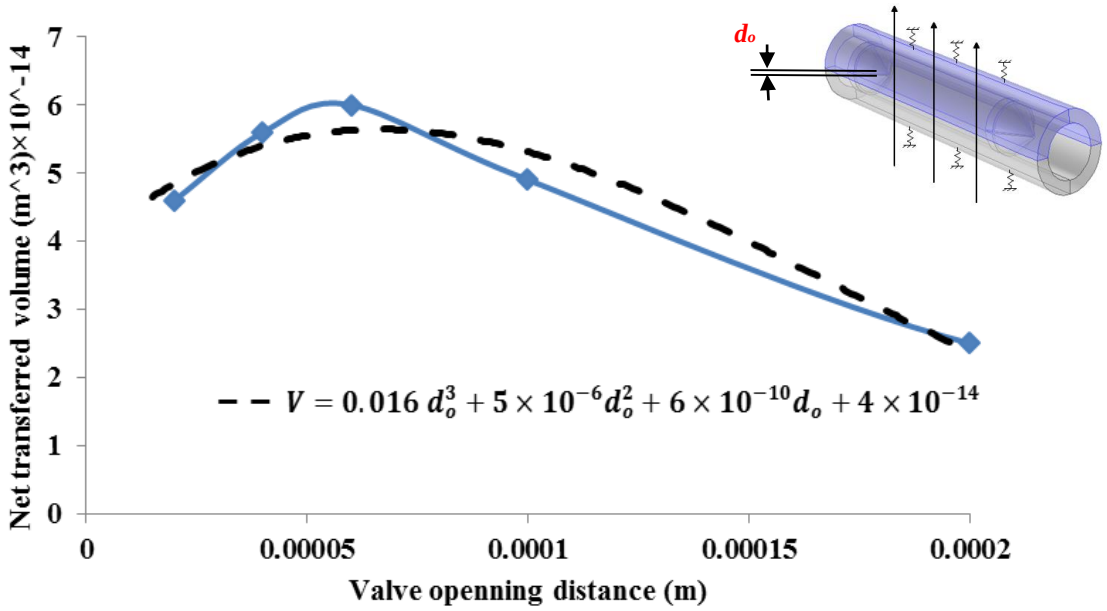

Figure 2.40. Effect of valve opening distance on the fluid flow.

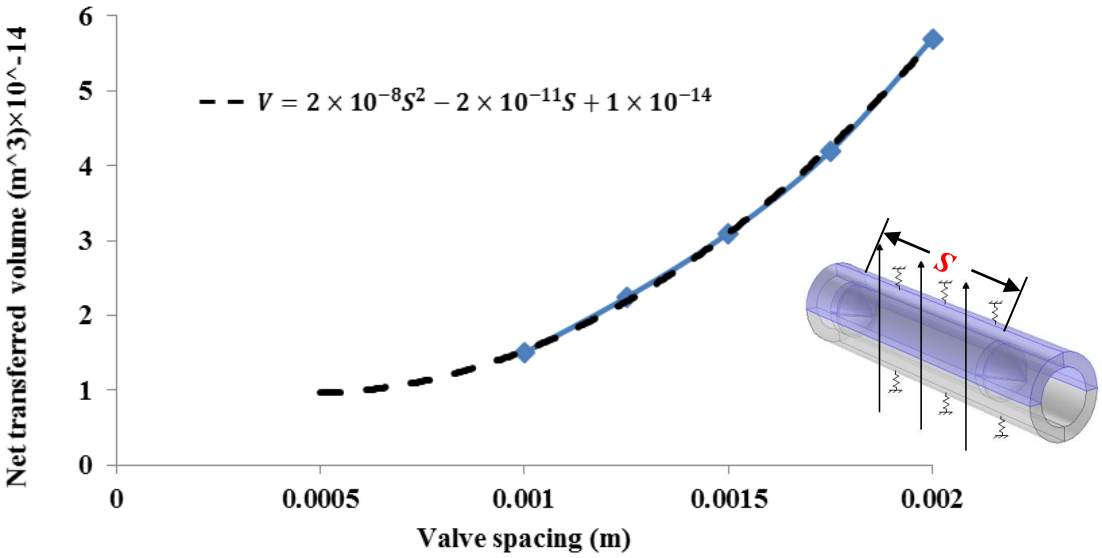

Figure 2.41. Effect of valve spacing on the fluid flow.

Next, mechanical and magnetic properties of the microchannel are studied. Elastic modulus and the spring constant of the elastic foundation affect performance of the system. Figure 2.42 shows that for elastic modulus of 1 MPa or higher the microchannel becomes very stiff and cannot deflect enough to propel fluid. Also if the channel is very soft i.e. $E \leq 0.01$ MPa, the net flow reaches its maximum since the fluid inside the channel is limited.

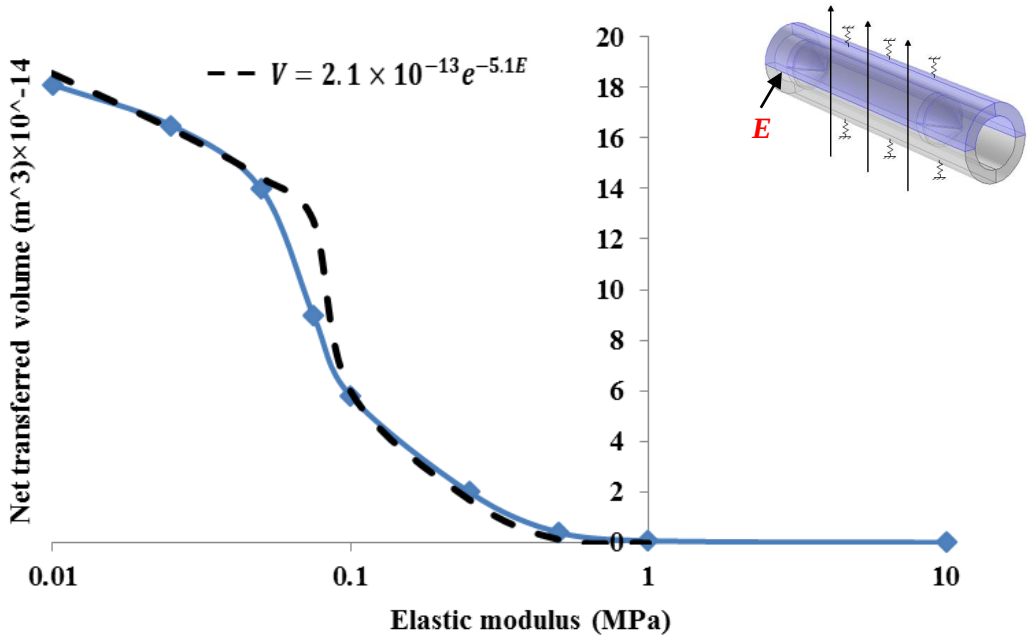

Figure 2.42. Effect of elastic modulus on flow.

Elastic foundation is one of the key factors in the performance of the system since a very stiff foundation does not allow the deflection of the microchannel. To examine the effect of elastic foundation on the performance of the system, the elastic foundation is varied from zero to that of a rigid base. Figure 2.43 indicates that the rigid foundation diminished the performance since the bottom of the channel cannot deflect. Also very low spring foundation constants decreases the net flow since the entire channel moves freely and it does not produce enough

deformation. Therefore, an optimum value for the spring foundation is determined which is 7×10^6 N/m.m^2. This result is also different from 2D analysis since in 2D the z direction of fluid and solid domain are not restrained.

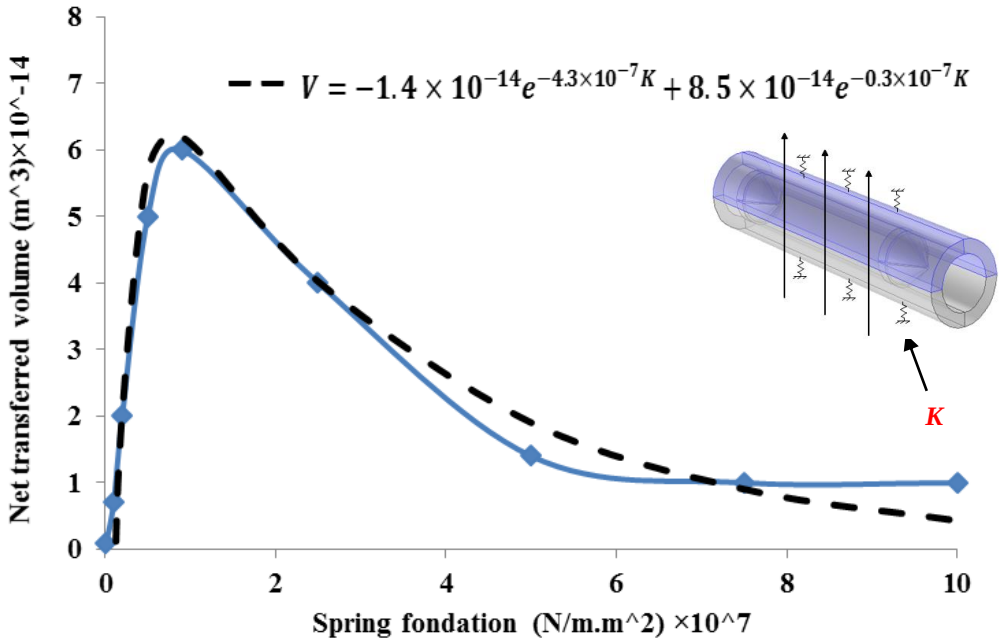

Figure 2.43. Effect of elastic foundation on the fluid flow.

Fluid viscosity also affects the total amount of fluid pumped by the system which can be explained with a polynomial function as shown in Figure 2.44. For the fluid viscosity of 0.01-0.05 Pa.s the pumped volume is minimal.

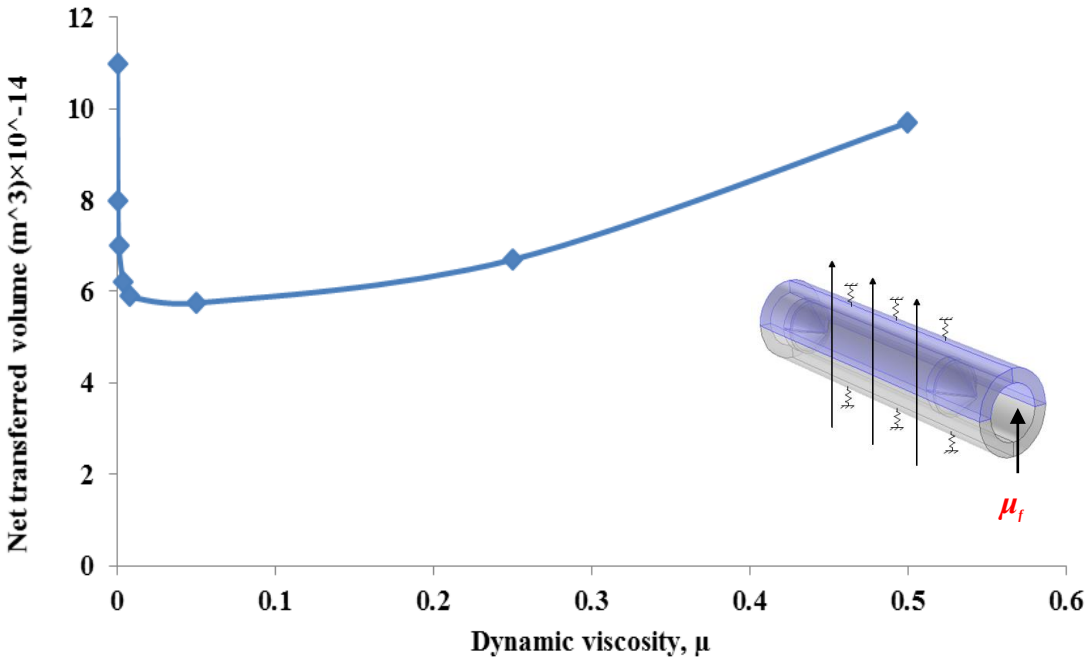

Figure 2.44. Effect of fluid viscosity on the fluid flow.

Magnetic force over the top part of the microchannel can be obtained using finite element methods by considering a lumped magnetic model. Figure 2.45 demonstrates the pumped fluid increases with applied magnetic field, but it reaches a plateau since the amount of encapsulated fluid in the microchannel is limited. This result is also consistent with 2D analysis since larger forces can squeeze the flexible channel more.

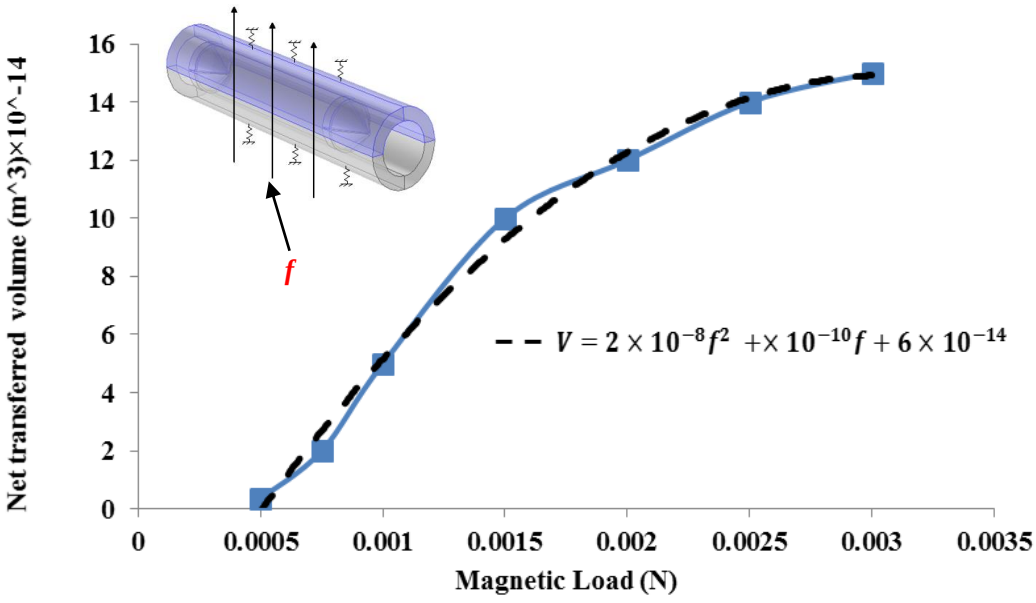

Figure 2.45. Effect of electromagnetic load on the fluid flow.

Using the macro-mechanics model for magnetic properties of MRE, magnetic permeability μ has been varied. As shown in Figure 2.46, increasing the magnetic permeability will increase the net flow; however around the magnetic permeability of 500, the SMREM becomes saturated and performance of the system remains the same.

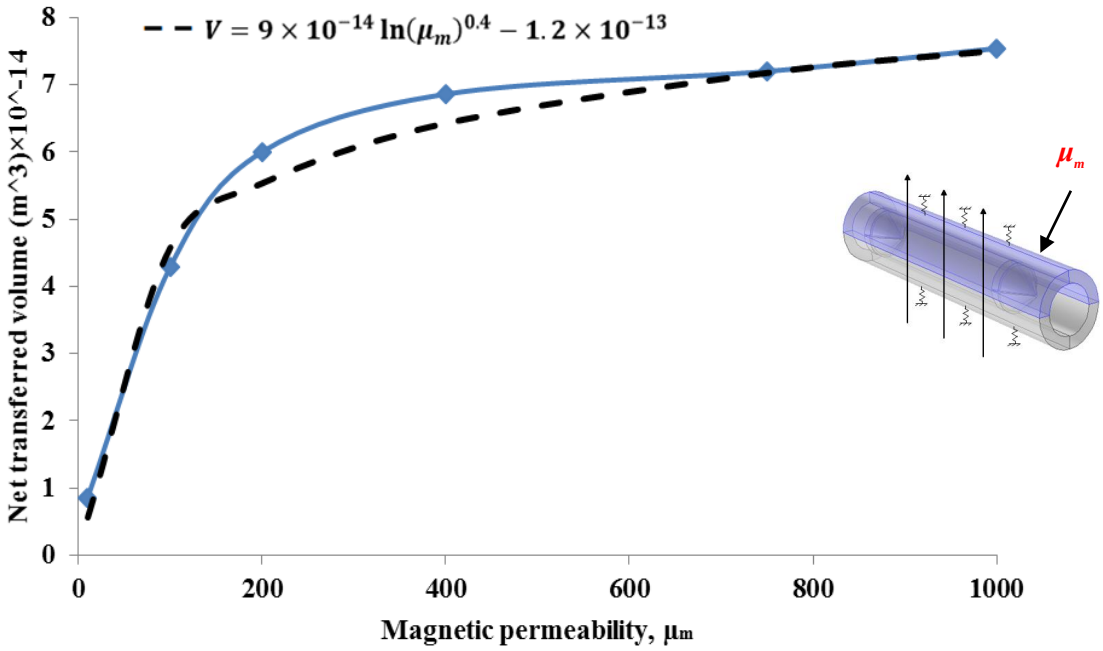

Figure 2.46. Effect of magnetic permeability on the fluid flow.

2.8. Summary and Conclusions

A flexible magnetically-actuated fluid transport system is presented, modeled and numerically analyzed in this Chapter. The flexible microchannel is made of soft magnetorheological elastomer membrane. A magnetic-solid-fluid coupling model is produced and numerically solved using time-dependent nonlinear solver of COMSOL multi-physics finite element package.

First, fluid flow in a converging microchannel is compared with analytical results to gain confidence with numerical fluid analysis. Next, 2D analyses are performed and the effect of each system parameter is individually investigated. Results of two-dimensional analysis show key parameters and their respective effect are channel diameter, 1,600%, elastic modulus,

1,600%, elastic foundation, 1,200%, and magnetic load, 500%. Finally, a three-dimensional analyses are performed to consider the effect of non-symmetric deflection on the transferred fluid. Results of the 3D analysis demonstrate that channel diameter, valve spacing, elastic modulus of the microchannel and magnetic load and magnetic permeability of the SMREM have similar effect for 2D and 3D analyses. However, valve length and valve opening distance, elastic foundation constant and fluid viscosity show different behavior.

CHAPTER 3

BEHAVIOR OF MAGNETORHEOLOGICAL ELASTOMERS WITH COATED PARTICLES*

3.1. Introduction

Magnetorheological elastomer (MRE) is a type of material which is composed of magnetic permeable particles dispersed in an elastomeric medium and show variable mechanical properties within a magnetic field. To fabricate MRE, magnetic particles are added to liquid-state mixture of polymer parts and the resulting mixture is cured either inside or outside of an external magnetic field resulting in isotropic or directional (orthotropic) MRE, respectively [69, 118]. When particles are aligned within the magnetic field, chain-like structures of magnetic particles are formed and locked in place. Gong et. al. [119] showed that isotropic MRE does not have a chain-like structure because it is cured without a magnetic field. The advantage of directional MREs is higher stiffness change, if the load is applied in the direction of the alignment or perpendicular to it. Magnetization of directional MRE is higher, when the magnetic field is applied parallel to the direction of the iron particle chains [120]. Also, higher compressive modulus, thermal conductivity and MR effect are observed for aligned polyurethane MREs [121] compared to homogenous MREs. Researchers have found that MR effect is more pronounced for softer elastomer matrix and the storage modulus

---

**This chapter is published in the Journal of Smart Materials and Structures. Behrooz, M., Sutrisno, J., Zhang, L., Fuchs, A., & Gordaninejad, F. (2015). Behavior of magnetorheological elastomers with coated particles. Smart Materials and Structures, 24(3), 035026.*

can be increased from 400 times [122] to 800% [67], if the off-state shear modulus is low, i.e. in order of kilo Pascal. Davis has theoretically found the optimum particle concentration for increasing the shear modulus to be 27% by volume [123]. Using shear tests, it has been shown that MR effect increases at higher frequencies [98] and a normal applied compressive load causes a reduction in MR effect during shear deformation [124].

MRE can show stiffness, damping, and hysteresis change within a magnetic field; however, damping change is minimal compared to stiffness change [125]. Such controllable properties can be utilized in vibration isolation applications such as variable stiffness elements, since MREs have a response time in order of milliseconds [66]. The controllable properties can be utilized in variable stiffness and damping devices such as vehicles' engine mounts [66], vibration absorber for vehicle transmission system [72], adaptive vehicle seat suspension [73], adaptive tuned vibration absorbers (ATVA) [80, 87], and base Absorber for building structures [94]. Other researches proposed soft MRE for air flow controllable valve [74] and adjustable springs in springs in prosthetic devices [75]. There is also limited work for modeling MRE behavior and it poses its own challenges since MRE shows non-linear viscoelastic behavior which is affected by magnetic field and loading frequency. A model is presented by Shen et. al. [126] for predicting the stress strain behavior of MREs within magnetic field as well as phenomenological models based on Ramberg-Osgood [99] and Bouc-Wen model [125].

In MREs iron particles are embedded in an elastomeric medium and are not exposed to air; however, the moisture and oxygen can penetrate with time and alter the properties of elastomeric matrix or the bonding between the matrix and the particles. Also, the hygrothermal effects may reduce the strength of the bonds among iron particles and the elastomeric matrix or

may affect the elastomeric matrix itself. It is shown that oxidation can significantly reduce the stability of natural rubber based MREs and higher oxidation rates are observed for MREs containing larger percentage of iron particles [127]. To prevent the oxidation of iron particles and hence increase the durability of the MREs, iron particles can be coated with different techniques including RAFT and click chemistry.

However coating may change mechanical, electrical, and magnetic properties of MREs that need to be investigated further. Coating carbonyl iron particles with Polypyrrole ribbons has other advantages such as improving sedimentation properties of MR fluid [128]. Also, coating particles of MR fluid with a layer of polysiloxanes can increase the oxidation and chemical stability [129]. It is shown that coating with poly methyl methacrylate PMMA can increase the shear modulus over 200%, and thus, reduce the relative MR effect [130]; but Lauryl Sodium Sulfate (SDS) and Sorbitan Monooleate (Span 80) as a coating layer have reduced the base shear modulus and increased the relative MR effect [131]. Compression test results have shown that polymerized iron particle MREs have higher oxidation stability [132]. The combination of RAFT and click chemistry reactions for surface polymerization of iron particles has been studied by Yuan et. al. [133]. Moreover, it is shown that coating particles reduces the magnetization saturation point [134]. Although previous studies have investigated the effect of particle coating on magnetization of particles and changes in properties of MRF, only a few studies have been performed on the effect of coating on mechanical properties on MRE.

In this research, particles of 50%wt MRE specimens are coated utilizing a combination of RAFT and click chemistry methods. To investigate the effect of coating on the performance of MREs, ASTM standard double lap shear specimens are fabricated for pure elastomer, 50%wt

coated, and 50%wt non-coated iron particles. MRE specimens are oxidized using an accelerated heat chamber. Shear experiments are performed to investigate the effect of coating and oxidation on MRE specimens. Results show that oxidation reduces the off-state shear stiffness of the MREs and hence increases the relative stiffness changes due to magnetic field. Finally coating of iron particles does not significantly change the shear modulus, but protects the MREs by reducing the loss of stiffness due to oxidation.

3.2. Coated and Non-Coated Particle MRE Specimens

3. 2. 1. Surface coating mechanism of iron particle via click chemistry

Polymer coating on iron particle surface can enhance both chemical and physical performances of MRE. A RAFT technique is employed to graft the polymers. Since the surface coating materials are non magnetizable, they do not affect the magnetic field while they improve the endurance of MRE. It is shown that 20%wt polymer coating on the iron particles surface decreases the magnetic saturation about 5% in compared with pristine iron particles [135]. The effect of coating on the magnetic saturation of iron particles may be negligible because the thickness of coating is in nanometer scale and mass percentage of polymer coating is lower than previously reported [135]. RAFT method offers a narrow polydispersity index which means polymer has uniform molecular weight [136–142] polymer can be covalently bonded to the substrate.

To coat the iron particles, the substrate should be functionalized using azide, and the tandem molecule is functionalized using alkyne group in order to react through click chemistry. Copper (II) sulfate is reduced in the presence of sodium ascorbate, which becomes Cu (I),

denoted as $[LnCu]^{+}$. In click chemistry, the ligand (Ln) can be the solvent, such as acetonitrile, and water [139]. The reduced copper/ligand reacts with alkyne group and this is followed by interaction with nitrogen from azide group. Finally, the reaction between the alkyne and azide functional groups yields a ring closed triazole group.

In this process, 0.5 grams of azide modified iron particles was added into a glass vial and followed by adding poly(tetrafluoropropyl methacrylate, MW 200.13 g/mol [143]) (0.5 grams) $CuSO_4$ (6.65 mg), sodium ascorbate (241 mg) and DMF (2 mL). The mixture was sonicated for 5 minutes and continuously stirred in oil bath at 70°C for 18 hours. The conjugated poly(tetrafluoropropyl methacrylate)/iron particles were filtered, and washed using DMF several times with toluene consecutively. Then, the poly(tetrafluoropropyl methacrylate) coated iron particles were dried in a vacuum oven at 50^{o}C for 24 hours.

Initially, iron particles were functionalized with 2-4(-chlorosulfonylphenyl)-ethytrichlorosilane (CTCS) in toluene. The particles were washed using distilled water and ethanol, consecutively, and dried in vacuum oven [132]. Surface initiated iron particles were then reacted with sodium azide in dimethylformamide (DMF) to provide azide terminated particles which would be reacted with alkyne through click chemistry reaction [144]. 3-benzylsulfanylthiocarbonylsufanyl-propionic acid as chain transfer agent (CTA) was synthesized according to the reported literature [145]. The synthesized CTA was modified with propargyl alcohol to provide alkyne group [144]. The alkyne terminated CTA was used to polymerize tetrafluoropropyl methacrylate monomer. This reaction resulted in alkyne functionalized poly(tetrafluoropropyl methacrylate). The mechanism of surface coating of iron

particles poly(tetrafluoropropyl methacrylate) through a combination of Reversible Addition Fragmentation Chain Transfer (RAFT) and click chemistry is shown in Figure 3.1.

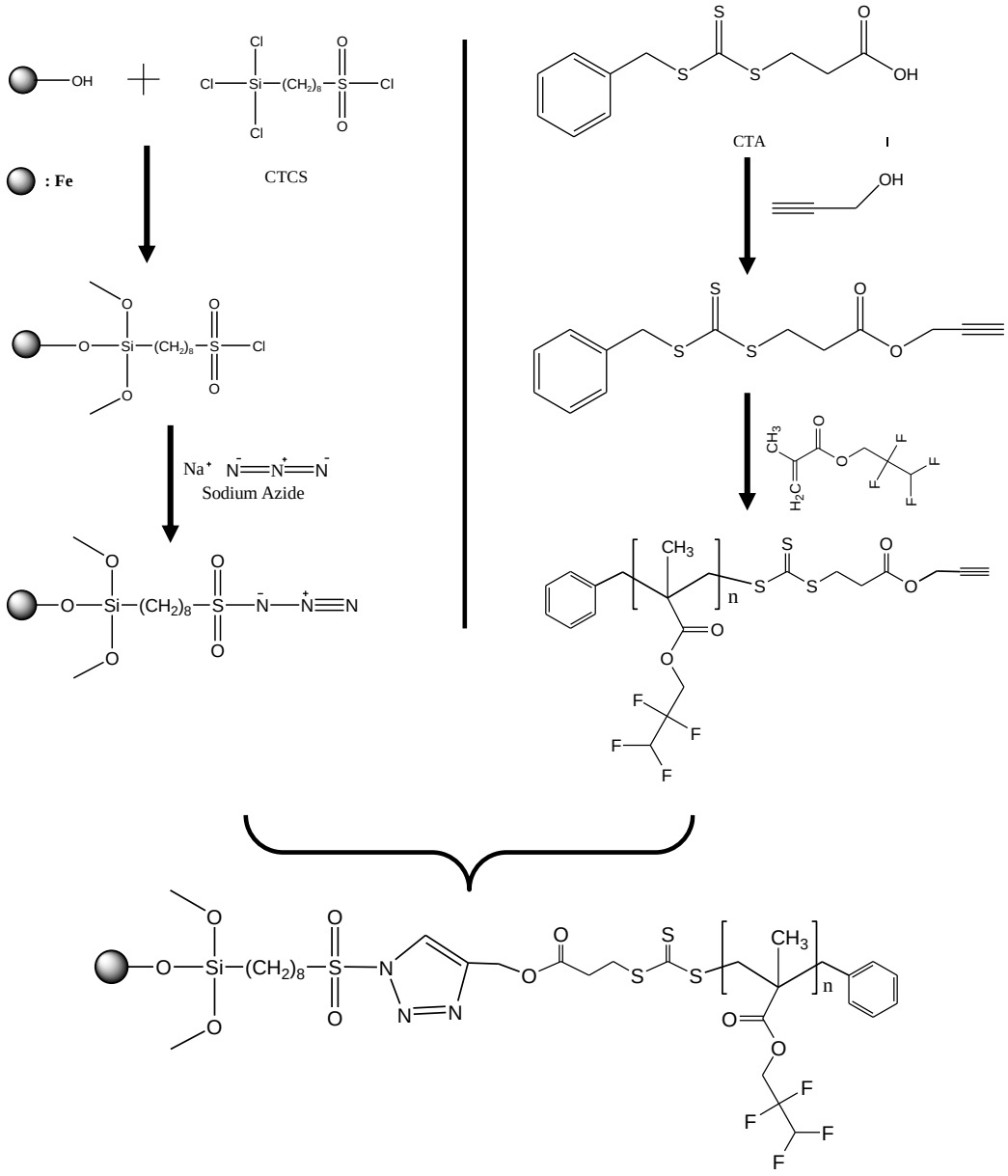

Figure 3.1. The mechanism of surface coating of iron particles poly(tetrafluoropropyl methacrylate) through a combination of Reversible Addition Fragmentation Chain Transfer and click chemistry [146].

The chemical analysis and surface morphologies of grafted poly(tetrafluoropropyl methacrylate)–iron particles was characterized using Hitachi S-4700 equipped with an Oxford EDS System. The specimens were magnified from 800X to 35,000X at an accelerating potential of 20kV. The SEM images of non- and surface coated iron particles are shown in Figure 3.2 (a) and Figure 3.2 (b), respectively. Thin and uniform grafted polymers on a single iron particle can be seen in these pictures.

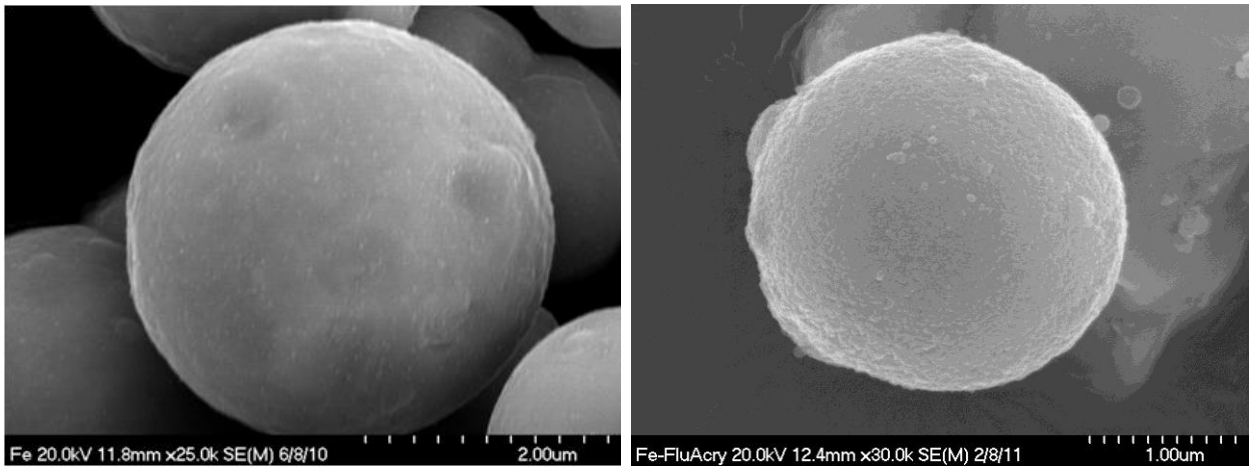

(a) (b)

Figure 3.2. SEM images of (a) non-coated and (b) coated iron particle [146].

3. 2. 2. MRE Fabrication

For this research pure rubber specimens, 50%wt coated and non-coated Silicone MREs were prepared. Silicone QM113A and B (Quantum Silicones) with the hardness of 7 durometer were used for elastomer matrix and carbonyl iron powder CN (3-7 microns, BASF) with a density of 3.5 (g/cm^3) was used as iron particles. The two components were mixed with a mixer for 7 minutes at a weight ratio 10:1. Then, iron particles were added at the desired weight

percentage, mixed, and the resulting mixture is poured into the mold. Then, the polymer was degassed at 25in Hg vacuum for 30 minutes to remove the bubbles, and cured under 1.0T of magnetic flux density for 5 hours at 70^{o}C to align the iron particles. The curing process was continued in the oven at 70^{o}C for 12 hours. The shear specimens were fabricated based on the ASTM standard [147]. The electromagnet with the shear specimen mold is shown in Figure 3.3 (a) and the shear MRE mold is shown in Figure 3.3 (b). The MRE mold is capable of curing 12 specimens at a time. The picture of silicone MRE specimens is shown in Figure 3.4 (a) and a silicone MRE double lap shear test is shown in Figure 3.4 (b). Sil-Poxy silicon adhesive was used and cured for 12 hours to bond MREs and steel bars. The surface of steel bars, where attached to MREs, were roughened using 220 grit sandpaper.

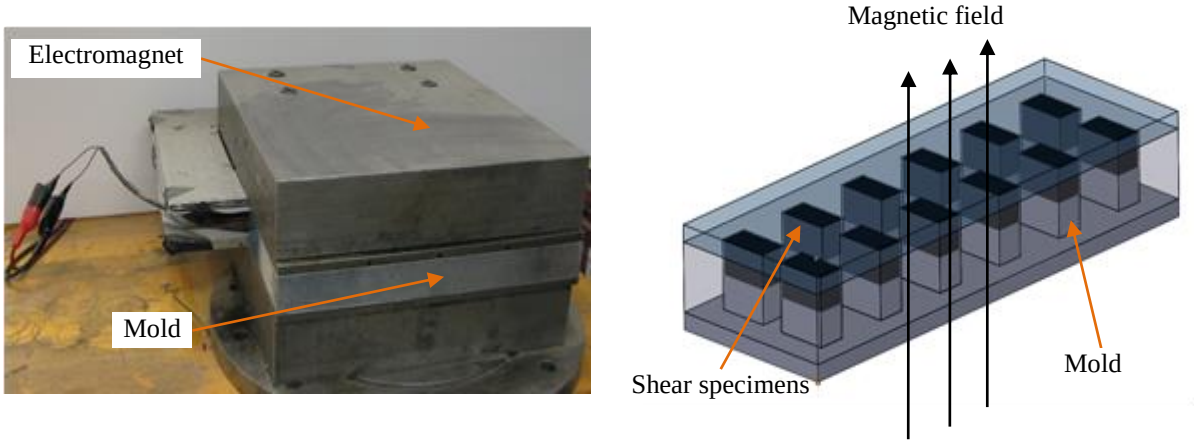

(a) (b)

Figure 3.3. Electromagnet for curing MREs and the mold inside.

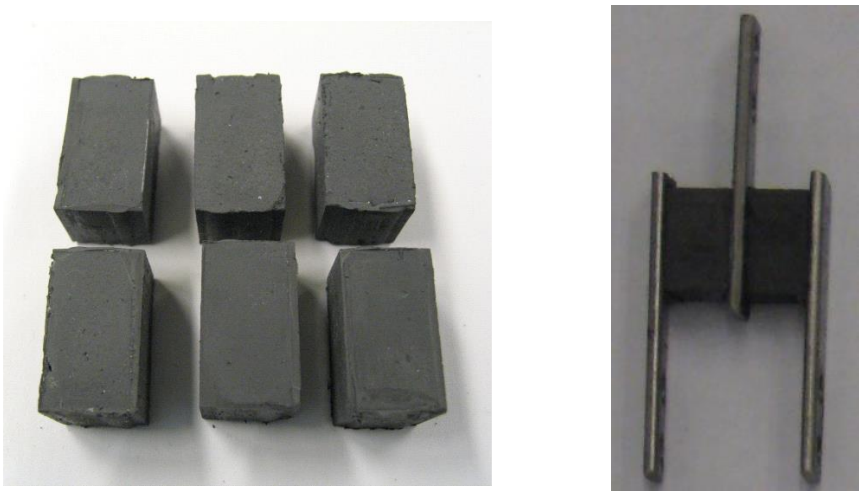

(a) (b)

Figure 3.4. Room Temperature Vulcanization (RTV) SiliconeMRE (a) shear specimens (b) shear specimen, for shear test.

3. 2. 3. Oxidation of MREs

Elastomer matrix and MRE specimens were exposed to air at room temperature for one week after they were removed from the mold prior to oxidation. Rectangular shape elastomer matrix and MRE specimens were placed on three aluminum racks and the position of each specimen was marked. The racks were placed into the chamber and the chamber was sealed. Compressed air was added to the chamber until the pressure reached 100psi. The thermo-controller was set to 100°C. When the temperature stabilized at 100°C, the pressure was adjusted back to 0.68 MPa. The specimens were taken out after one weeks. The oxidative test procedure for the MRE specimens with polymer coated iron particles was treated, similarly. The accelerated aging chamber is shown in Figure 3.5.

Figure 3.5. High pressure reactor for MRE ageing.

3.3. Shear Experiments

Shear properties of MREs can be examined using a quasi-static shear experiment. To correlate the input electric current with the magnetic field inside MRE specimens, the magnetic field is measured using a magnetometer. As shown in Figure 3.6 (a) the probe of the magnetometer is inserted in a small slit inside the specimen and the electric current is changed to measure the magnetic field of different specimens. The actual magnetic field inside MREs is expected to be a little higher since the slit is expected to reduce the flux density. Figure 3.6 (b) demonstrates the magnetic field which is strongly related to the iron particle concentration and does not change considerably with the oxidation of the specimens. For coated particles the magnetic field is 9.35% lower on average since the coating layer occupies space and reduces the amount of iron particles per unit volume. In the case of the pure elastomer specimens, there

is 150mT magnetic flux density at 5amps; but as it is shown in Figure 3.8, the effect of magnetic field, when iron particles are not present, is minimal.

(a)

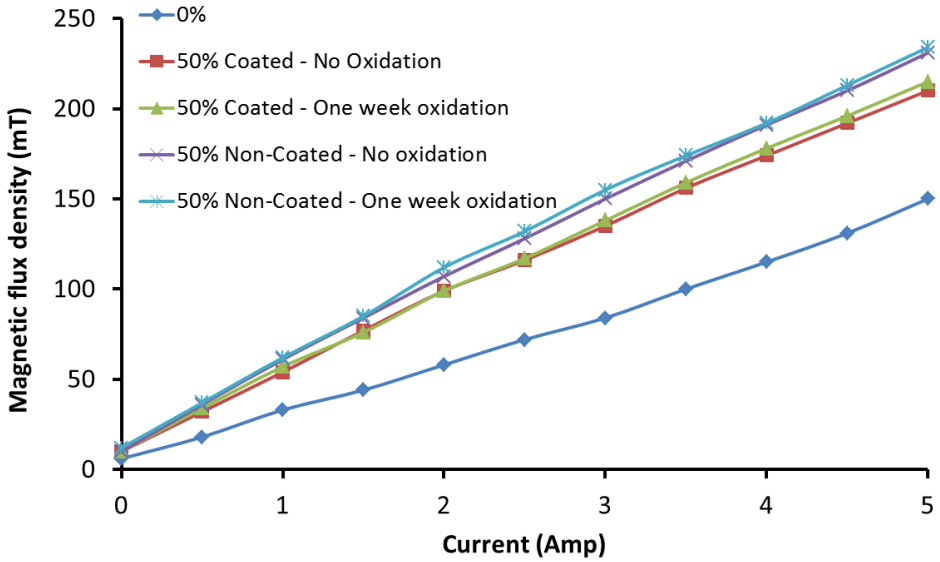

(b)

Figure 3.6. (a) Magnetic flux density measurement test set up, and (b) magnetic flux density for different specimens at different amps.

To investigate the effect of coating and oxidation on MRE specimens, double lap shear tests are performed on an Instron electromechanical testing system (model 4210), as shown in Figure 3.7. Shear test setup is consisted of two thick steel plates, and an electromagnet that can generate a closed-loop magnetic field, when the specimen is installed. Shear test specimens are bolted to the Instron actuator and the shear test setup. All parts are parallel to ensure pure shear test condition. A 500lbf Lebow load cell (model number 3132-500) and a RDP Electronics LVDT (model number DCTH100AG) DC to DC displacement transducer with ±2.5mm range and 1494mV/mm is used to measure force and displacement, respectively.

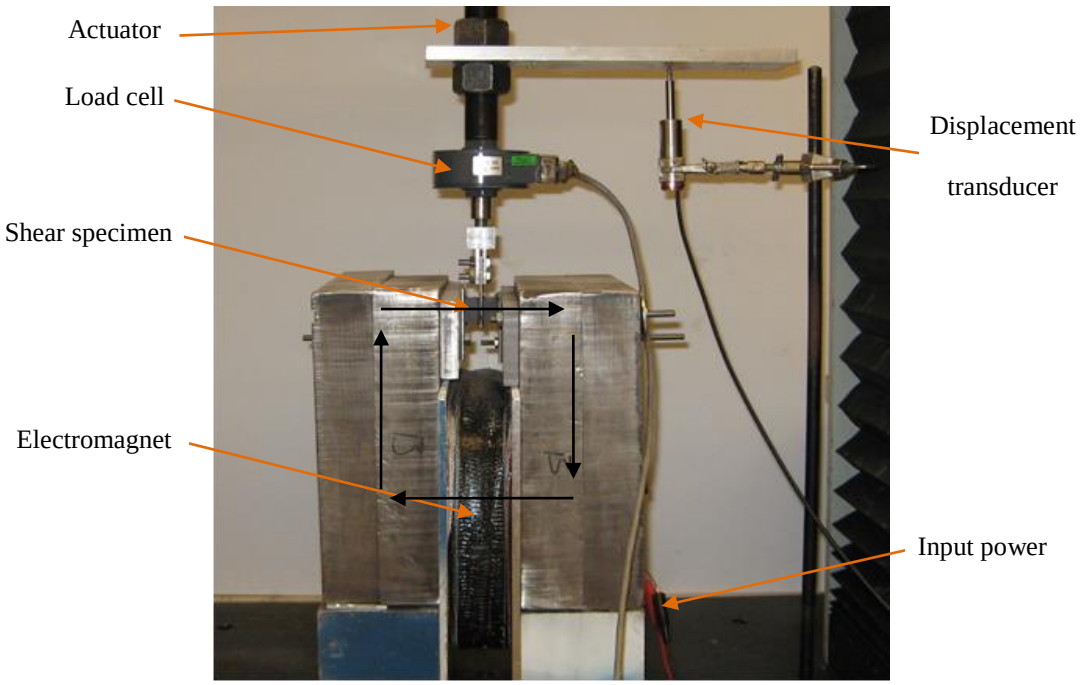

Figure 3.7. Double lap shear test setup and INSTRON dynamic testing system.

Shear experiments are performed on pure elastomer and 50%wt coated and non-coated specimens with the input frequency of 0.1Hz and 17.5% strain amplitude. The input electric current is increased from zero to 4 amps to observe the effect of induced magnetic field within MREs. The applied magnetic field within MREs is parallel with the iron particle chains to achieve highest possible MR effect. Each test has been performed four times to ensure the consistency of the results and to obtain the standard deviation. Figure 3.8 (a) demonstrates shear test results of the pure elastomer specimens. As can be seen, the magnetic field does not affect the shear test results. As shown in Figure 3.8 (b), oxidation for a period of one week significantly reduces the shear modulus of the elastomer.

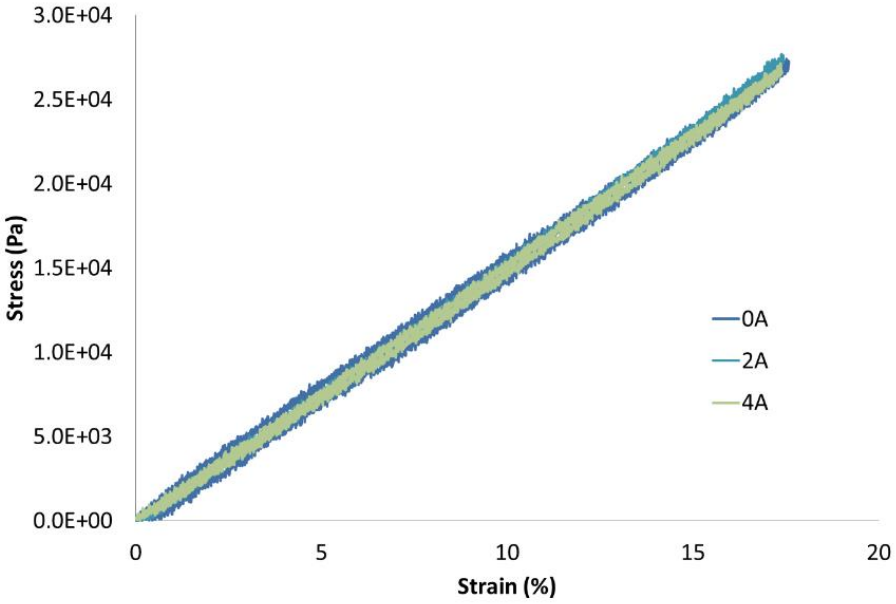

(a)

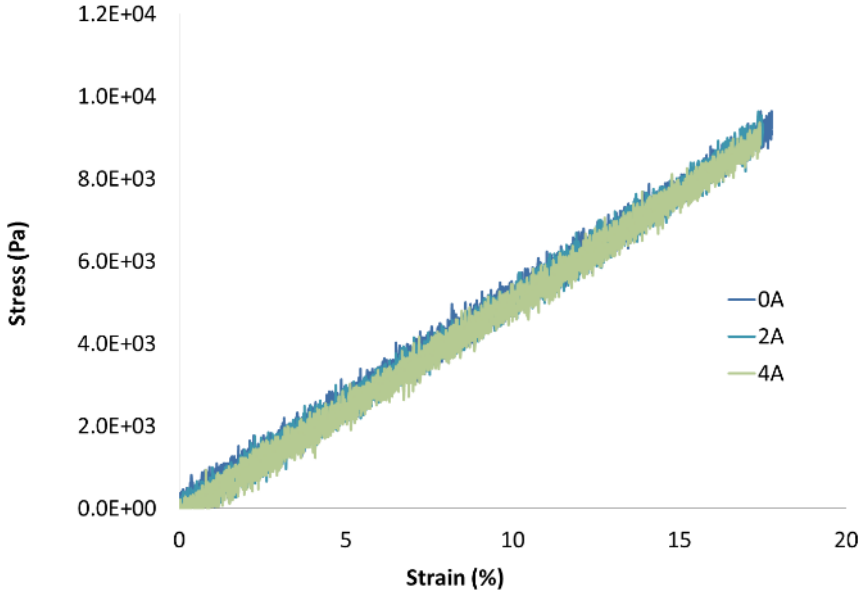

(b)

Figure 3.8. Pure elastomer (a) without oxidation, and (b) after one week of oxidation.

Figure 3.9 shows the stress-strain loop of the shear MRE specimens with 50%wt non-coated particle concentration. As can be seen, by increasing the input electric current the maximum stress in the loop increases, which corresponds to increase in the stiffness. However, area of the loop stays almost unchanged; thus, the change in the damping is minimal. On the other hand, since the base stiffness decreases after oxidation, then the relative change of the stiffness increases. This occurs since the stiffness change remains constant, but the off-state stiffness is reduced.

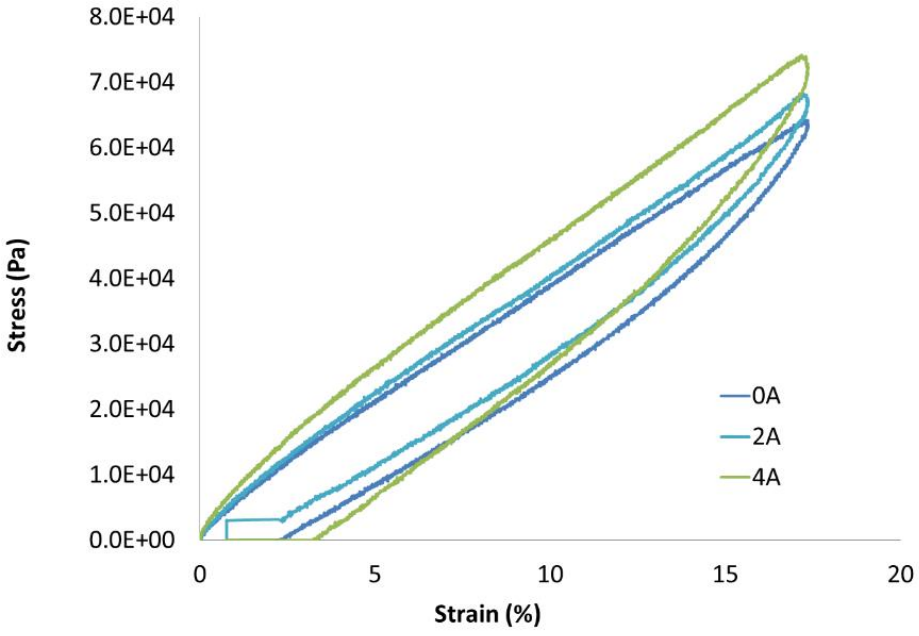

(a)

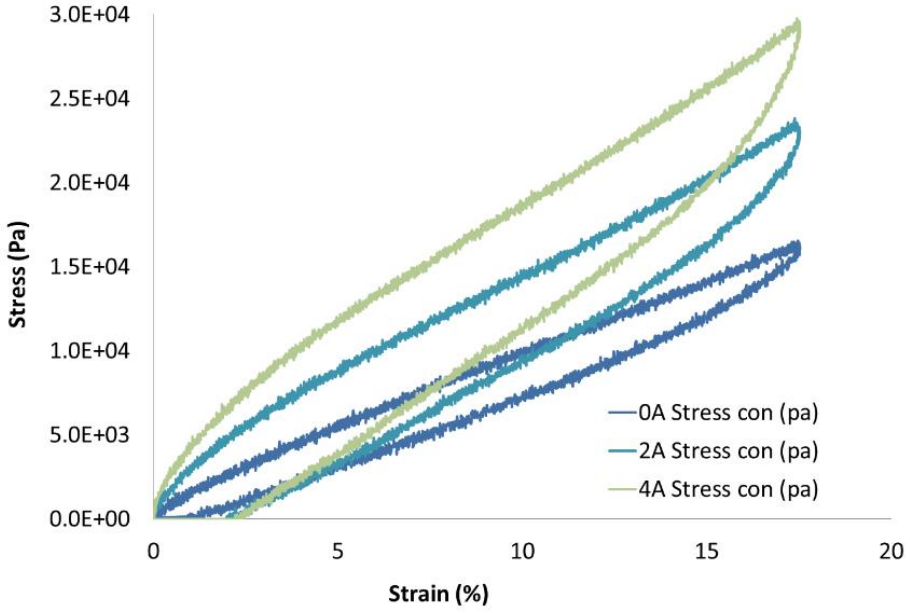

(b)

Figure 3.9. Stress-strain results for 50%wt non-coated MRE specimens (a) without oxidation, and (b) after one week of oxidation.

Figure 3.10 shows similar results for MREs with 50%wt coated particles. Comparing the two Figures shows that the off-state stiffness does not change with coating of the iron particles, but after oxidation the off-state stiffness is less reduced as compared to the non-coated particles. This suggests that the coating preserves the stiffness better under oxidation.

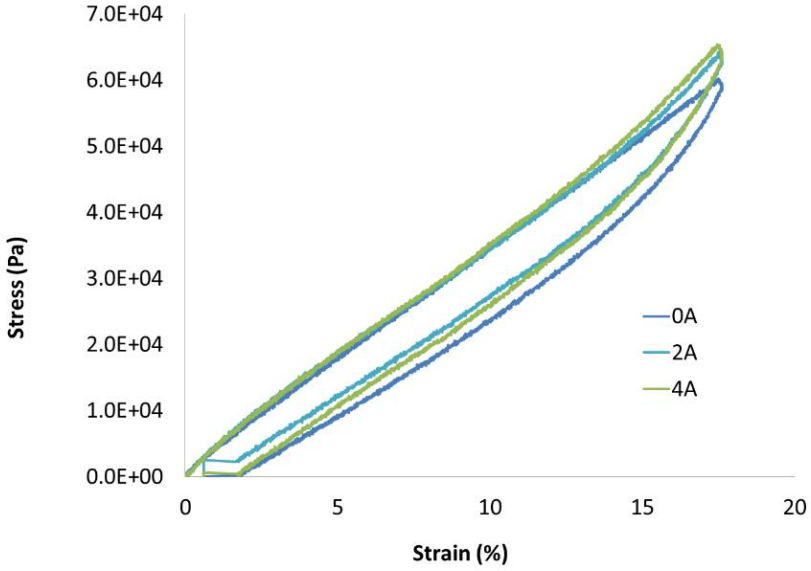

(a)

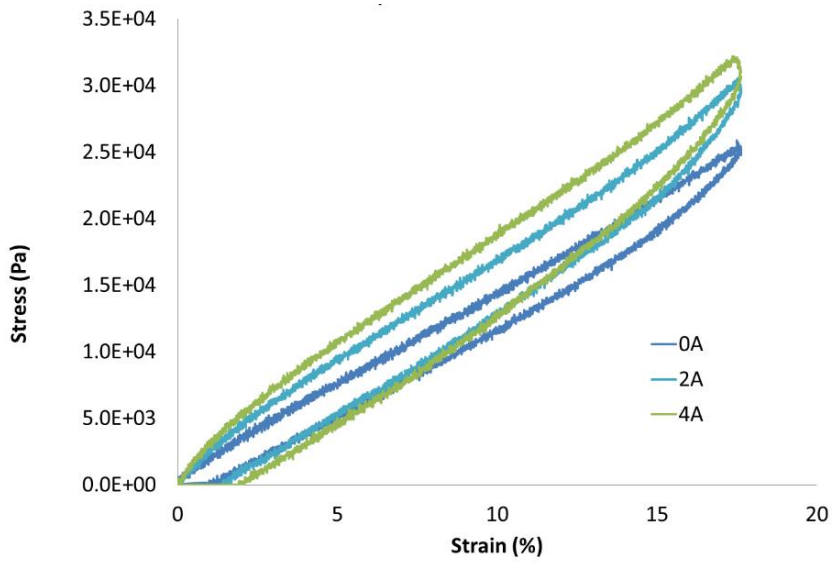

(b)

Figure 3.10. Stress-strain results for 50%wt coated MRE specimens (a) without oxidation, and (b) after one week of oxidation.

The effective shear modulus helps to understand the MR effect under polymerization. The effective shear modulus is obtained based on maximum strain and maximum stress [101]. The MR effect is calculated using Equation (1). MR effect for pure elastomer and 50% wt. coated and non-coated MRE is presented in Table 3. 1. along with the standard deviation of the effective shear modulus. As can be seen from Table 3. 1., oxidized coated specimens tend to preserve the MRE properties compared to non-coated specimens.

$$MR\,effect = 100 \times \frac{G_{on} - G_{off}}{G_{off}} \tag{1}$$

Table 3. 1. Effective Shear Modulus and Percentage of MR Effect.

			Input current (A)	Effective shear's modulus (kPa)	Standard deviation	MR effect (%)
0%wt		Non-oxidized	0	152.6	1.21	
			2	153.6	0.65	0.6
			4	156.9	2.32	2.8
		Oxidized	0	51.5	0.8	
			2	51.6	0.32	0.2
			4	51.7	0.26	0.4
50%wt	Coated	Non-oxidized	0	342.9	7.37	
			2	365.7	7.12	6.7
			4	374.3	5.41	9.2
		Oxidized	0	145.7	1.35	
			2	171.4	2.11	17.6
			4	182.9	2.47	25.5
	Non-coated	Non-oxidized	0	365.7	6.67	
			2	388.6	5.42	6.2
			4	422.9	6.22	15.6
		Oxidized	0	94.3	1.17	
			2	134.3	1.54	42.4
			4	168.6	2.17	78.8

3.4. Summary and Conclusions

In this study iron particles are polymerized using a combination of RAFT and click chemistry techniques. Shear MRE specimens are prepared based on the ASTM standard using coated and non-coated particles. Some MRE specimens are oxidized and their shear properties are examined utilizing double-lap shear tests to observe the effect of coating on performance of MREs.

Results show that oxidation significantly reduces the shear modulus of the pure elastomer as well as the MREs. The shear modulus of the pure elastomer is reduced three times while shear modulus of non-coated MREs is reduced nearly four times. This demonstrates that oxidation mainly affects the elastomer matrix, and also affects the bonding among particles and the matrix. It is shown that the effective modulus of coated MREs reduces 2.3 times, and that coating particles preserves the stiffness of MREs in oxidative environments.

CHAPTER 4

MODELING OF A NEW SEMI-ACTIVE/PASSIVE MAGNETORHEOLOGICAL ELASTOMER VIBRATION ABSORBER*

4.1. Introduction

Protecting civil structures from hazardous vibrations can play a key role in saving lives and resources. Various active, passive and semi-active vibration devices have been proposed to protect civil structures from seismic or severe storm events [58]. Each system has its own advantages and disadvantages. Semi-active vibration absorbers have received attention because they consume less power than active devices and controllability over passive systems [58, 59]. A recent study has shown that a semi-active/passive absorber using magnetorheological elastomers (MREs) could potentially improve traditional base isolation systems in seismic control of structures [77].

MREs are composed of micron-sized magnetic particles embedded in an elastomeric medium and are analogous to magnetorheological fluids (MRFs). For MRFs, the yield stress can be altered by an external magnetic field, while MREs have controllable stiffness that is a function of applied magnetic field. MREs do not leak and their ferrous particles do not sediment as opposed to MRFs. MREs are solid, flexible, can operate in a wide range of frequencies and can tolerate large deformations in tension, compression and shear. Both MREs and MRFs have fast response time (in the order of milliseconds) under an applied magnetic field.

**This chapter is published in the Journal of Smart Materials and Structures. Behrooz, M., Wang, X., & Gordaninejad, F. (2014). Modeling of a new semi-active/passive magnetorheological elastomer absorber. Smart Materials and Structures, 23(4), 045013.*

Previous studies have shown potential applications of MREs for vibration control. For example, MREs can be used in automobile engine variable stiffness suspension system [66, 85, 120] or vehicle seat suspension system [73]. MREs have also been shown in applications such as adaptive tuned vibration absorbers (ATVAs) [83, 84, 87, 91, 92]. ATVAs can shift the natural frequency of the system by changing the shear modulus of MREs [86]. ATVAs with a real time controller can potentially suppress the response of a building compared to passive dynamic vibration absorber [95].

Variable Stiffness and Damping Absorbers (VSDAs) have been suggested in structural control. With appropriate control strategy, the VSDAs can suppress and avoid system resonant response. Kobori et al. [60] proposed and implemented an effective and low power VSDA in braces of a seismic response controlled structure. Yang et al. [62] implemented a variable stiffness system based on bypass dampers and showed its performance depending on the type of the structure. Most of the conventional VSDAs are mechanical or hydraulic systems and have inherent disadvantages, such as, complex structure, slow response and leakage [64]. A VSDA employing MRE, which may provide a solution to overcome these issues, has been proposed and investigated by the authors [64]. In other studies, modification of traditional lead rubber bearing with MREs led to a new controllable bearing device [96] and a small-scale MRE-based bearing was studied as base absorber for structural applications[97]. Previous works by authors [64, 93, 96, 97] have shown a design and test results in modifying traditional steel rubber bearings into a semi-active device using MREs. To use VSDAs for vibration control, the shear force deformation needs to be identified. Shear force deformation of MREs have been

experimentally investigated [98] and models have been proposed to predict behavior of MRE devices under various mechanical deformation and applied magnetic fields [99, 100].

In this study, a new VSDA device for vibration control is investigated. The proposed VSDA system consists of a traditional steel-rubber vibration absorber, as the passive element, and MREs with a controllable stiffness and damping behavior, as the semi-active elements. The device is a transition between traditional passive absorbers and active absorbers. It features a novel fail-safe design because of the integration of semi-active MRE and passive rubber elements. This means that if MREs or electrical system fail to function, the rubber parts retain the minimum functionally of a passive steel rubber base absorber. In this work, a VSDA prototype is designed, fabricated and tested. The performance of the device under shear deformation is explored by using a double lap shear test setup to obtain the force-displacement relationship. Four VSDA prototypes have been manufactured and tested with significant stiffness and damping changes when activated with an input electric current. Performance of an integrated system consisting of four VSDAs, a connecting plate and a controlled mass is investigated using shake table tests. By measuring the frequency response of the integrated system, the capability of the VSDAs in shifting the natural frequency of the system is observed using frequency sweep technique for different input electric currents.

4.2. Design of the MRE-Based VSDA

Figure 4.1 a shows a cross section view of the proposed VSDA. It includes two steel caps each embedded with two coils. The size of the absorber is 128×64×110 mm. Rubber elements, MREs and shims are 12, 10 and 2 mm thick, respectively. Diameter of the MRE is 60

mm and the size of each cap is 128×64×42 mm. Coils embrace the steel core and steel top and the bottom circular plates which retain windings. The number of turns for each coil is 800 and the power for each VSDA is 234.2 W at 4 Amps. Two MREs and one elastomer layer on each side are placed on the top of each cap such that the MREs are placed on the top plate. Positive and negative power cords are configured so that a closed loop magnetic field is guaranteed in the device to generate the highest possible magnetic field in the MREs. In Figure 4.1a perpendicular magnetic fields are in the same direction as the particle chains in MREs where they were cured and aligned. The steel shim plays two roles; first it makes a channel for the passage of the magnetic flux resulting in higher magnetic field in MREs, and second it prevents elastomeric layers from tearing upon the application of large strains. For the electromagnetic design ANSOFT finite element package is utilized. The electromagnetic simulation and optimized results shows that the MREs in conical shape design combining with certain thickness shim would achieve highly effective magnetic field to activate the device. In this design, two thick low-carbon steel plates embedded with four electromagnets generate a closed-loop magnetic field. The steel shims, rubbers and MREs are placed between the two thick steel plates. Figure 4.1 b shows the prototype of the VSDA and input power cords.

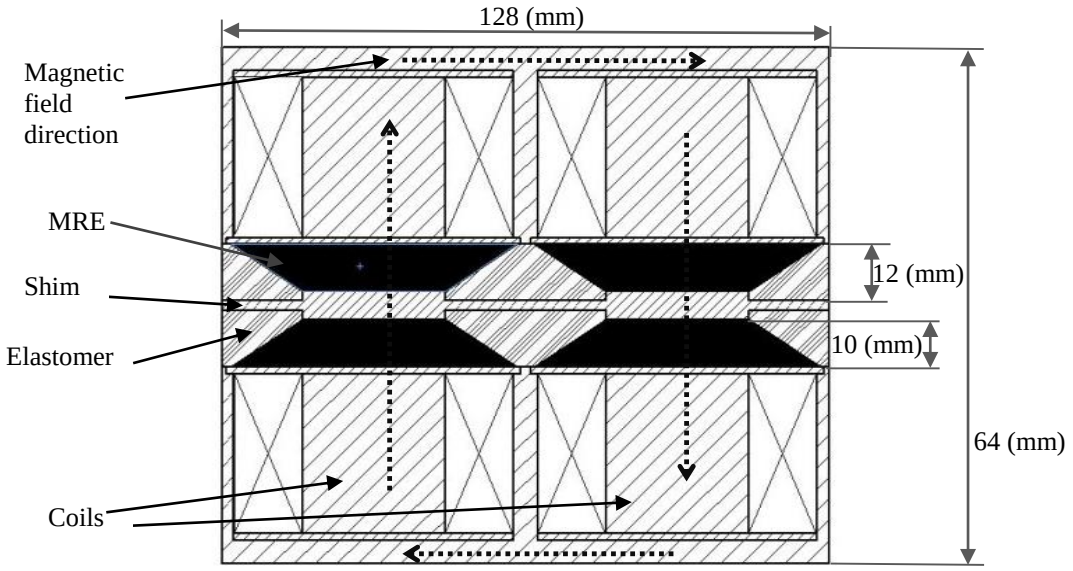

(a)

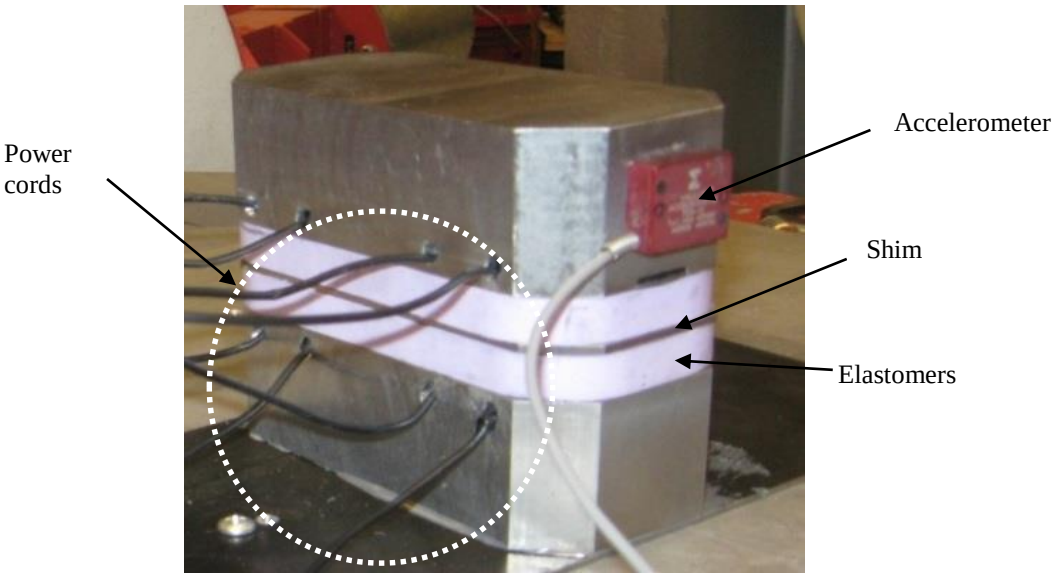

(b)

Figure 4.1. (a) Schematic of the cross section of VSDA, and (b) photo of the VSDA.

The magnetic field distribution inside the VSDA is analyzed using the ANSOFT finite element package. A quarter-model is constructed to obtain the magnetic field distribution. The

simulation results in cross section area of A-B are presented in Figure 4.2. Based on these results, a relation between the applied electric current (*I*) and the magnetic field strength (*B*) is developed. As shown in Figure 2, when the current approaches 5 Amps, the magnetic field approaches saturation. An average magnitude of 0.65 Tesla can be achieved to activate the device with an applied electric current of 4 Amps.

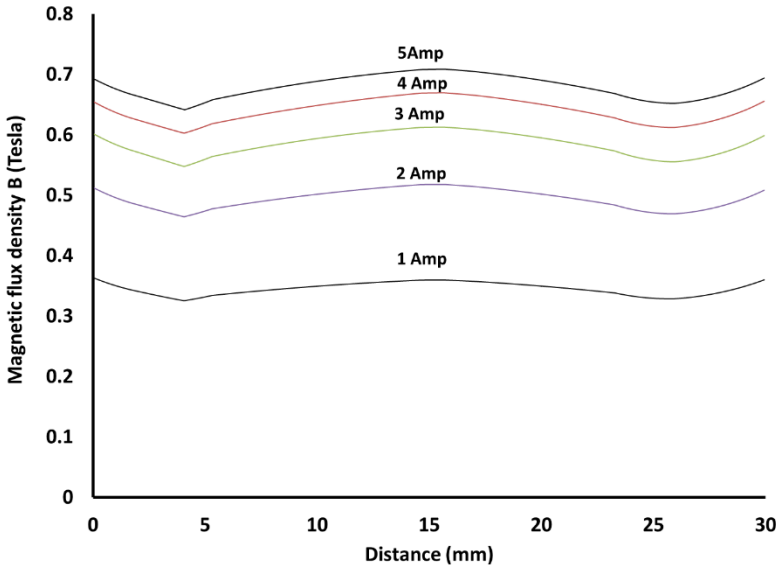

Figure 4.2. Magnetic field distribution inside the VSDA for different input currents.

Elastomer support is fabricated from a mixture of QM 113A and QM 113B from Quantum Silicones. The two components were mixed at a weight ratio of 10:1 with a high speed mixer for 5-10 minutes. The pre-cured polymer was degassed at 25 in-Hg vacuum for 30 minutes to remove the bubbles, and cured in the oven at 70^{o}C for approximately 24 hours, and then the elastomer was demolded. Silicone MRE was synthesized using QM107A, QM107A (hardness 7 durometer) and iron particles with average diameter of 10 µm. The two components

were mixed at a weight ratio 10:1 with a high speed mixer for 5-10 minutes. Iron particles were added at 80wt%, mixed completely. Then, the pre-cured polymer was degassed at 25 in-Hg vacuum for 30 minutes to remove the bubbles. The formation of chainlike structures of iron particles within MREs is important to their performance. Thus, the chains are formed by placing the pre-cured silicone–RTV MRE mixture in an electromagnet under 1 Tesla magnetic flux density inside MREs for 5 hours. The chains are formed during chemical cross linking of the elastomer. The curing process is continued in an oven at 70^{o}C overnight.

4.3. Double Lap Shear Experiments

To characterize the MRE-based VSDA, a double lap shear test setup is designed, fabricated and installed on a 5 kip Instron dynamic testing system (Figure 4.3). The top plate of the setup is connected to the Instron load cell and the middle plate is connected to the actuator. Two VSDA devices are mounted between the vertical plates of the shear test setup. The movement of the actuator which is connected to the middle plate of the two VSDAs shears the MREs as well as the elastomers inside the devices. All parts are installed in parallel to ensure the movement in pure shear. The force and displacement are measured directly by the Instron load cell and a LVDT, respectively. To obtain the effect of the magnetic field on the stiffness and damping change of the VSDAs, the input electric current is increased from 0 to 4 Amps with step increment of 1.0 Amp for each test. The shear strain is obtained based on the ratio of the shear displacement to the thickness of two elastomeric layers of the devices which is 20 mm in this design. The maximum shear strain of 2%, 5%, and 10% is considered for this test based on input shear displacements.

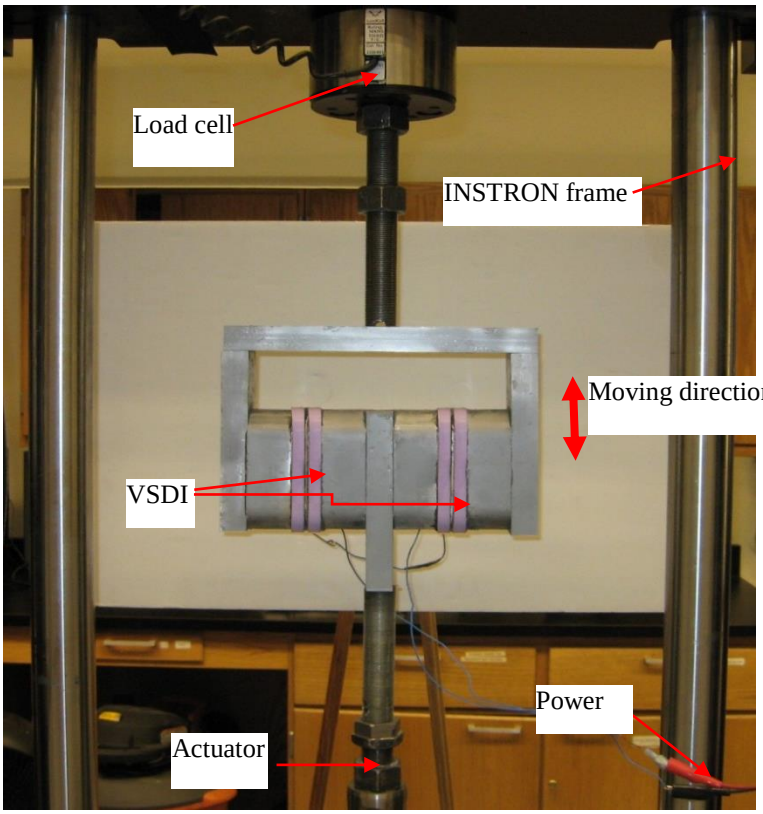

Figure 4.3. Double lap shear test setup on the INSTRON dynamic testing system.

Figure 4.4 shows a typical result of the force-deformation curves of the VSDA for different applied electric currents and the maximum shear displacement of 1.0 mm which corresponds to 5% strain. As can be seen, by increasing the input electric current, the slope of the curve increases. This means that the stiffness of the VSDA can be altered by the applied magnetic field. The area under the hysteresis loop, which represents increasing the damping capacity, also increases by increasing the applied electric current.

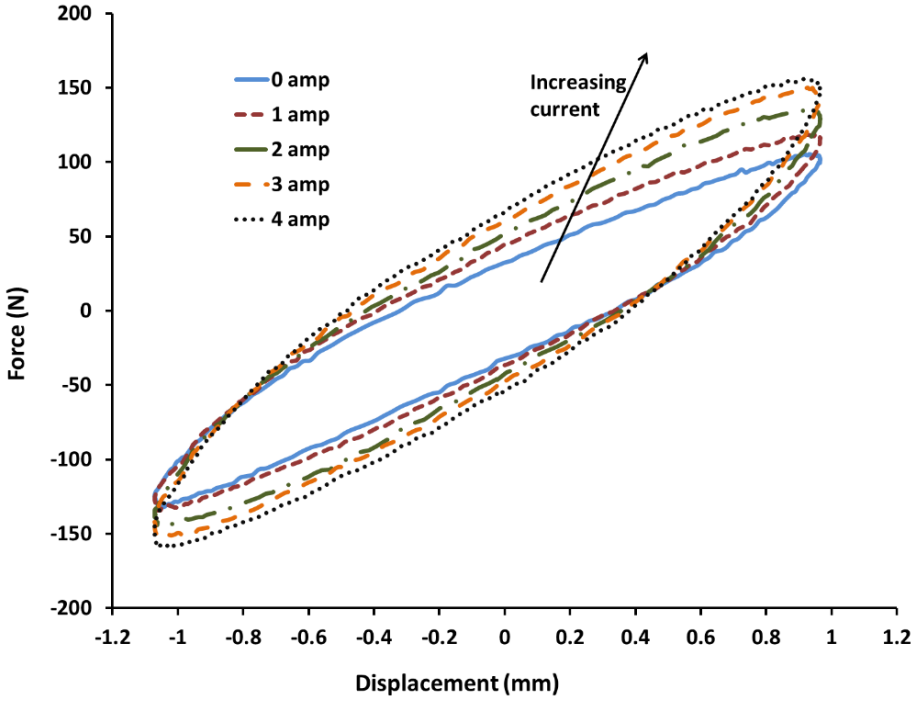

Figure 4.4. Shear deformation test results of VSDA at 0.1 Hz

In a study by Isaković et. al. [96] on the full-scale magnetic base absorber, the maximum shear force exerted by the absorber was shown to increase for about 39%, and 34% in another prototype study [97]. A full-scale base absorber with MREs was shown to be able to increase the maximum force 33-45 % depending on the input frequency [101]. Also, using soft MREs in base absorber, Li. et. al. [148] have increased the maximum load over 15 fold. As shown in Figure 4.4, 57% increase in the maximum load is attainable with the application of 4 Amps. Higher-force performance in this study is attributed to the closed loop magnetic design and optimization.

4.4. Theoretical Study and Parameter Identification

To use the VSDA along with a control system, its vibratory behavior needs to be modeled in terms of a force-displacement relationship. Eem et. al. used a combination of Maxwell and Ramberg-Osgood models as a phenomenological model for shear deformation of MREs [99] and Li et. al. used another phenomenological model based on Koh-Kelly model to predict the behavior of MRE base absorber [148].

Bouc-Wen model [149] is employed in this study. The VSDA is expected to show stiffness, damping and hysteresis behaviors; therefore, a phenomenological model with springs, viscous dampers and a hysteretic Bouc-Wen element is proposed as shown in Figure 4.5. In this model, increasing the magnetic field increases stiffness, damping and hysteresis effect of the device with a current dependent spring, k_m, a current dependent damping coefficient, c_m and a current dependent Bouc-Wen coefficient. The control force of the VSDA device is:

$$f_{VSDI} = \alpha z + k_2(x - y) + c_2(\dot{x} - \dot{y}) + k_m x + c_m \dot{x} \tag{1}$$

where, α is a constant and z is the evolutionary variable to introduce hysteretic behavior of the Bouc-Wen model defined as [26]:

$$\dot{z} = -\gamma|\dot{x}|z|\dot{z}|^{n-1} - \beta(\dot{x})|z|^n + A(x) \tag{2}$$

where, β, γ, n and A can be found from fitting the experimental data and y is a dependent variable calculated from the balance of forces:

$$k_1 y = k_2(x - y) + c_2(\dot{x} - \dot{y}) \tag{3}$$

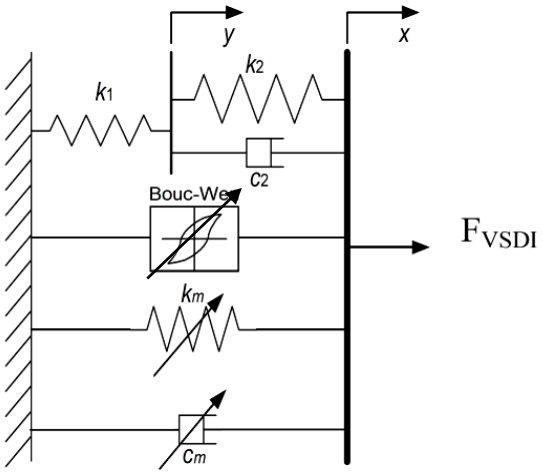

Figure 4.5. The proposed phenomenological model.

The stiffness and damping elements are assumed to have a linear relation with the applied current, as follows:

$$\mathrm{k_m} = \mathrm{k_{m1}I} + \mathrm{k_{m0}} \tag{4}$$

$$\mathrm{c_m} = \mathrm{c_{m1}I} + \mathrm{c_{m0}} \tag{5}$$

$$\mathrm{c_m} = \mathrm{c_{m1}I} + \mathrm{c_{m0}} \tag{6}$$

where, I is the applied current, k_{m1}, c_{m1} and α_{m1} are the stiffness, damping and hysteresis effect changes per Amp and k_{m0}, c_{m0} and α_{m0} are the off-state stiffness, damping and hysteresis effect. A SIMULINK model has been developed to incorporate the equations and to obtain the shear force-displacement characteristics of the VSDA based on the proposed model. The model constants are found and optimized by comparing experimental and simulation results using

SIMULINK and MATLAB. The constant parameters of the phenomenological model are shown in Table 4. 1. These parameters define the shape of the hysteresis loop and do not change with current and strain amplitude.

Table 4. 1. Constant Parameters Used for VSDA Modeling.

Parameter	Value	Parameter	Value
N	1.14	k_1 (N/m)	40,000
β (1/m^2)	70	k_2 (N/m)	25,000
γ (1/m^2)	3,000	c_2 (N/s.m)	80
A	150	c_{m1} (N/s.m)	2
		c_{m0} (N/s.m)	40

Figure 4.6 shows the force-displacement results of the VSDA from experimental results and reconstructed theoretical modeling for on-state and off-state. The stiffness, damping, hysteresis effect, and their respective changes are captured accurately with this model. The sharp corners are created by the absolute function in the Bouc-Wen model. Theoretical results show that the error is less than 5%. Figure 4.7 shows the results of the off-state shear force deformation of the VSDA from experimental and theoretical results for various displacement inputs. It is shown that the shape of the curves changes with different displacement amplitudes. Such behavior suggests that the model proposed above should have strain-dependent parameters, as well. The strain-dependent parameters are obtained and presented in Table 4. 2.

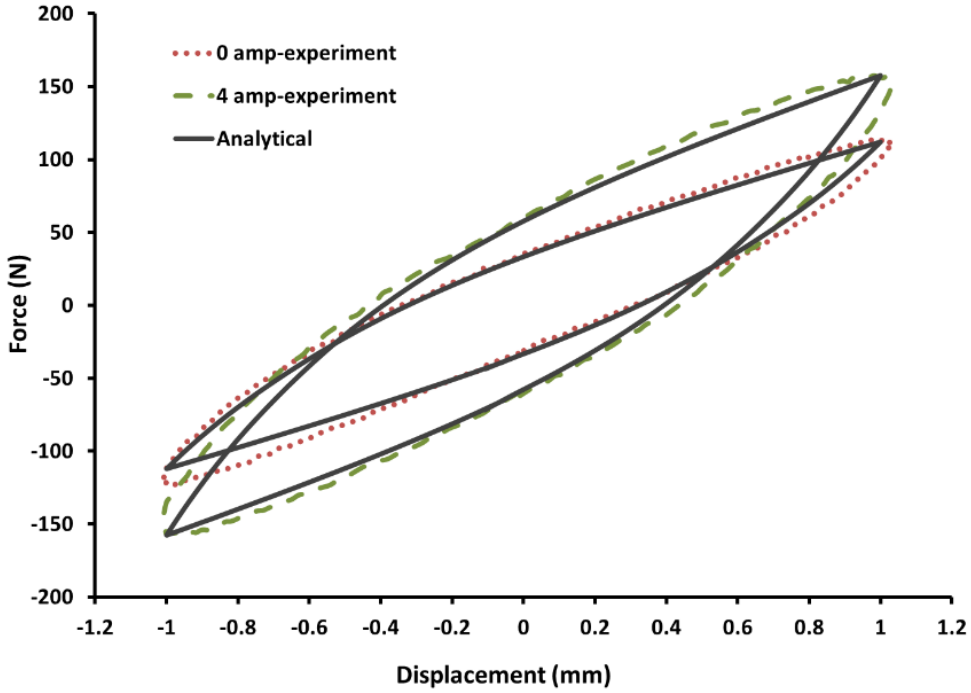

Figure 4.6. On-state and off-state shear force deformation characteristics of VSDAs for 5% strain at 0.1 Hz.

Table 4. 2. Strain-Dependent Parameters Used for VSDA Modeling.

Strain %	α_{m0} (N/m)	α_{m1} (N/m)	k_{m0} (N/m)	k_{m1} (N/m)
2	700	125	45000	3000
5	600	110	25000	3750
10	720	75	50000	1250

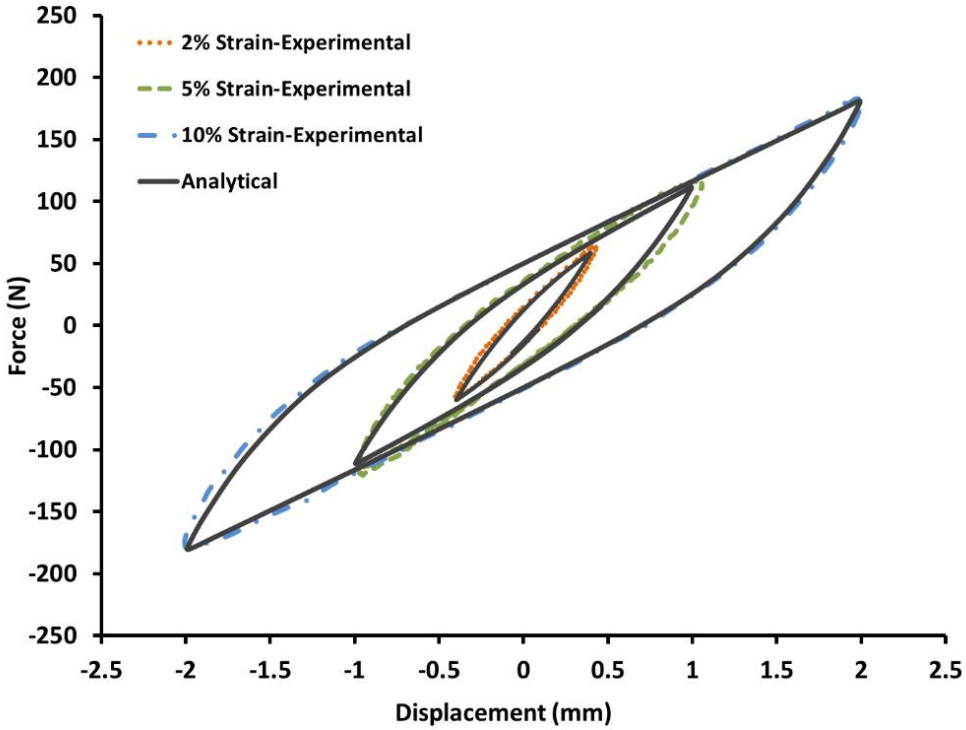

Figure 4.7. Off-state strain-dependent behavior of VSDAs at 0.1 Hz.

Figure 4.8 shows the on-state results of the shear force deformation of VSDAs from the experiments and the proposed model. It is shown that the defined constants can capture changes in the stiffness, damping and hysteresis of the VSDAs for each strain level and each input current.

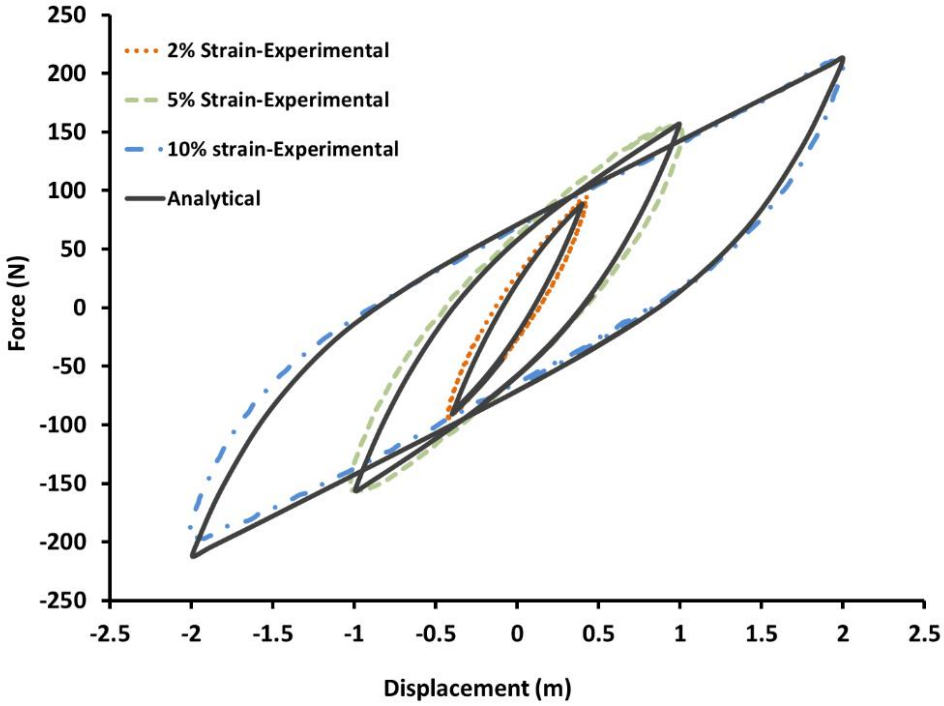

Figure 4.8. On-state strain-dependent behavior of VSDAs at 4 Amps and 0.1 Hz.

In this study, the proposed model is verified for the strain ranges of up to 10%. Increasing loading frequency also affects the load exerted by the VSDAs as expected for viscoelastic materials. The parameters of the proposed model are identified based on dynamic testing of an integrated system to consider this effect.

4.5. The Integrated System

To demonstrate feasibility for vibration control, an integrated system consisting of four VSDAs, a connecting plate and a controlled mass is designed and built. The performance of the integrated system is studied under various vibration conditions using the LDS shake table, as shown in Figure 4.9. Four prototypes of the VSDA device are manufactured and tested with significant stiffness and damping changes, when the applied electric current is increased. The

VSDAs are installed on a horizontal LDS-Dactron shaking table. VSDAs are secured to on the slip plate and a connecting plate is glued on top. A mass is introduced to the system, as the controlled mass. Two accelerometers are calibrated and installed on the slip plate and upper mass to measure the input and output accelerations, respectively. The total weight of the mass component in the integrated system is 135.7 Kg, which consists of four VSDA top caps, a connecting plate and the supported mass. The system is considered a single-degree-of-freedom (SDOF) vibration system with a mass, controllable spring and variable damping dashpot. The experiments were carried out using constant 0.1 g input acceleration and applied electric current ranging from 0 to 2 Amps. The frequency was swept from 5 to 25 Hz to obtain the transmissibility function. Laser USB data acquisition system is used to collect both input and output accelerations and the transmissibility function is calculated by the shake table software.

In a previous work it has been shown how the properties of a single VSDA could be used to predict the performance of integrated systems [22]. In this study, a SIMULINK model along with signal processing is developed to model the behavior of the integrated systems as shown in Figure 4.10. In this model the input current is changed to determine the integrated system's response with different input electric current. The input to the phenomenological model, which is shown in Figure 4.5, is the relative displacement and the output is the force exerted by four VSDAs

Figure 4.11 a shows the transmissibility function and increased stiffness from the experimental results and Figure 4.11 b shows the same data from theoretical modeling results. From the insert in Figure 4.11 a, it can be seen that natural frequency increases almost linearly with the input current. This verifies that the linear assumption of stiffness increase with current

is valid. Also the parameters of the model are identified for these dynamic experiments to consider the effect of increased frequency on VSDAs.

In the current test range, the performance of the integrated system of the VSDAs did not show saturation with 2 Amps which means the VSDA devices have the potential to induce more changes in the stiffness and the damping of the system, if more electric current is applied. Comparing Figure 4.11 a and Figure 4.11 b demonstrates the capability of the proposed model for predicting dynamic behavior of VSDAs in the integrated system. The model predicts the stiffness change accurately which can be seen from the peak frequency in both figures. However the damping prediction which is related to the peak transmissibility has 11 to 31% error depending on the input current. This may be due to higher damping that occurs at higher frequencies. The results shows less damping occurs in quasi-static case compared to the dynamic testing; therefore, the damping obtained from quasi-static case needs to be modified for the prediction of the dynamic behavior of VSDAs.

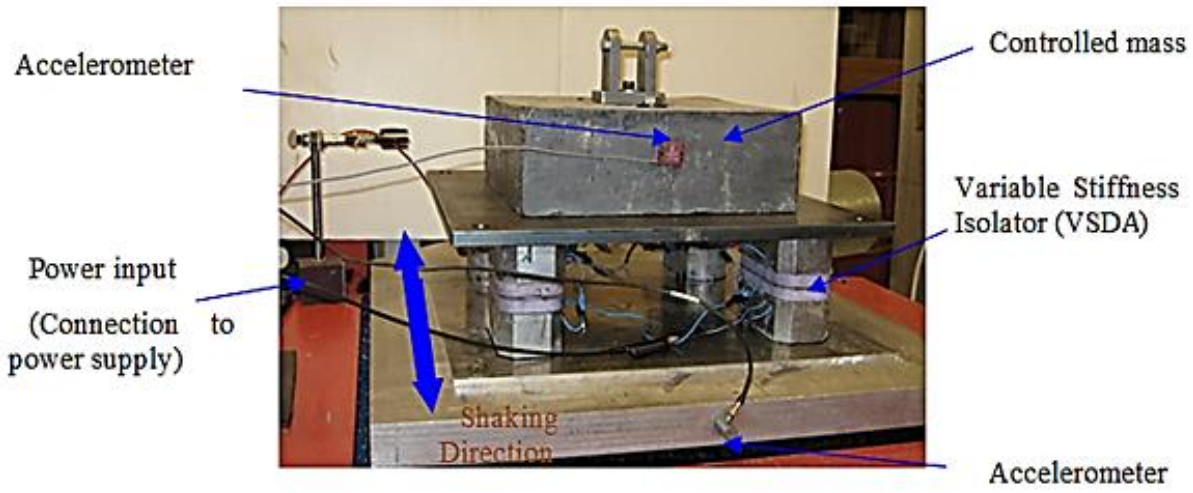

Figure 4.9. Photo of the experimental setup for the integrated system with four VSDAs.

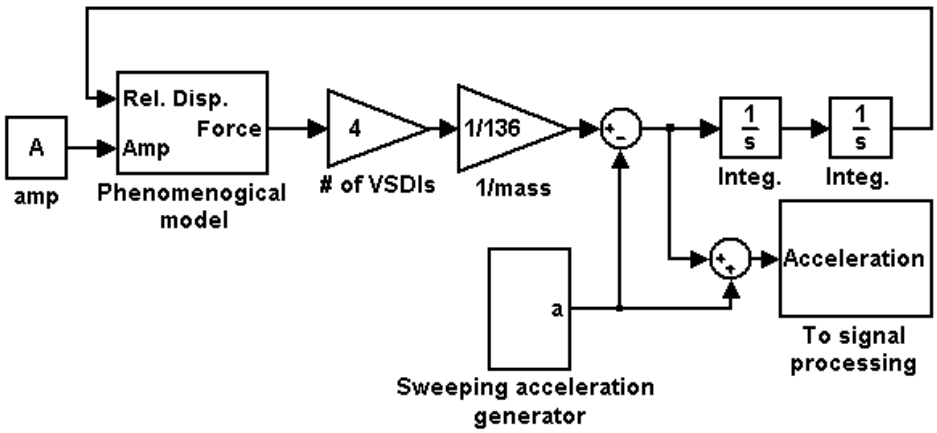

Figure 4.10. SIMULINK model of the integrated system.

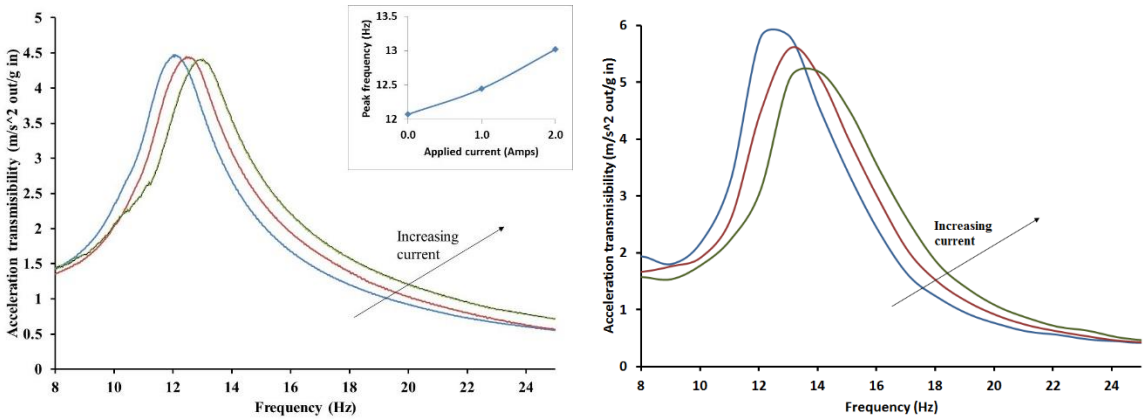

(a) Experimental (b) Theoretical

Figure 4.11. Transmissibility results of the integrated system of VSDAs for various input currents.

4.6. Summary and Conclusions

A prototype VSDA is designed, built, and tested under quasi-static and dynamic shear loads. To model the behavior of the system, quasi-static shear tests are performed. Increase in the area of the hysteresis loop shows the increase in damping and increase in the slope of the force deformation curve shows the stiffness increase. A phenomenological model which can capture the behavior of the VSDA is developed and the respective parameters are identified using experimental data from the double lap shear tests. The model is able to predict the behavior of VSDA with different input electric current and strain amplitude. The model will be used for future control applications.

The performance of an integrated system of VSDAs is investigated with shake table vibration experiments to demonstrate their functionality to isolate a scaled structure from ground vibrations. Results of the integrated system reconfirm that VSDAs are able to alter damping and stiffness of a scaled building with an applied electric current. While increasing the supported mass will decrease the absolute natural frequency change of the system, VSDAs are still able to increase stiffness and damping of the system. Moreover, when applied to the integrated system and its parameters are tuned, the model is able to capture the natural frequency of the integrated system. This verifies that the model can be used for control applications with modification of some constants from quasi-static testing.

CHAPTER 5

PERFORMANCE OF A NEW MAGNETORHEOLOGICAL ELASTOMER ISOLATION SYSTEM*

5.1. Introduction

Base isolation can reduce the seismic vibration and prevent damage to structures. Semi-active vibration absorbers can potentially outperform other forms of absorbers, if their mechanical properties are tuned with a controller [60]. Most semi-active absorbers are intended to mitigate vibrations by changing either stiffness or damping or both in the structures. Semi-active vibration absorbers could potentially be an option in structural control [59, 61, 104–106]. Controllable, semi-active isolation systems can simultaneously reduce the acceleration and displacements of a structure [107], but reliability issues may limit their application for civil structures [108]. Most conventional variable stiffness devices are mechanical devices [58, 60] or hydraulic systems [61–63] with inherent disadvantages, such as delayed response, complex structure and liquid leakage. A magnetorheological elastomer (MRE)-based isolation system may address some of these issues.

MRE is a composite material composed of dispersed micron-size magnetizable particles embedded in an elastomeric medium. MREs can operate in a wide range of frequencies and

---

** This chapter is published in the Journal of Smart Materials and Structures. Behrooz, M., Wang, X., & Gordaninejad, F. (2014). Performance of a new magnetorheological elastomer isolation system. Smart Materials and Structures, 23(4), 045014.*

tolerate large shear deformations. MREs have a very fast response time on the order of milliseconds [66]. Furthermore, MRE-based devices do not have leakage and sedimentation issues. MREs have theoretically been shown to be effective is vibration isolation of structures [76]. MRE-based devices have been used as the controllable semi-active elements in vibration isolation applications including Adaptive Tuned Vibration Absorbers (ATVAs) [79–81], dynamic vibration absorbers for multiple story building structure [83], vehicle seat vibration absorber [150] and engine vibration absorber [151] since they can increase the natural frequency of the system over 100% [82]. Recently MREs have been used for base isolation of structures as a prototype [78] and in a full scale absorber with 38% stiffness increase with application of 5 Amps [101].

Utilizing MRE-base device without a controller may not be beneficial for all frequency bands. A controller can tune performance based on the input vibration and minimize the transferred shock or vibration to the structure. Different control strategies, including optimal control [109, 110, 152], maximized energy dissipation with discretized on-off control [111], skyhook [110], LQG controller[153], Lyapunov-based strategies [111, 113, 154] and a turbo-Lyapunov controller [155] have been implemented for controlling MRF dampers, but limited studies have been conducted on control of MRE-based systems. Different active and semi-active control strategies for structural control of a benchmark building have been proposed for design purposes [114]. Jansen et al. [111] compared different control strategies and found Lyapunov and clipped optimal control are effective strategies for semi-active structural control. In a recent theoretical work, a MRE isolation system has been implemented to a scaled structure

with a fuzzy logic control strategy [78]. Also, it is shown that on-off control is effective for MRE base isolation systems [91].

In the present study, a two-story scaled building isolated with four VSDAs is theoretically and experimentally investigated. A previously developed model along with the state-space equations of the scaled building are used to develop a feedback control loop. The Lyapunov-based control strategy is suggested for this work and control parameters are tuned using simulation of the controlled isolated scaled building. Simulation results demonstrate the advantage of using VSDAs for the base isolation of the scaled building. Finally, a two-story scaled building supported by four VSDA absorbers is designed, built and tested under the scaled El-Centro EW seismic input. The control strategy is applied to the base absorbers to verify the applicability of the proposed model and the control strategy for reducing the acceleration and displacement response of the scaled structure.

5.2. Dynamic Performance of the VSDA

The fail-safe design of the VSDA consists of two thick low-carbon steel caps each embedded with two electromagnets to generate a closed-loop magnetic field. There are 800 turns in each coil and the input power to each VSDAs is 234.2 W at 4 Amps. The steel shims, rubbers and MREs are placed between the two thick steel plates to maintain the resemblance with traditional steel rubber bearings and provide the fail-safe feature. The shear stiffness of MREs increases due to an increase in the magnetic field; thus, increasing the stiffness of the VSDA. To demonstrate the capability of the VSDAs for the base isolation, dynamic shear experiments are performed using shake table tests as shown in Figure 5.1. Constant acceleration

tests with sinusoidal swept frequency technique are used to study the dynamic stiffness and damping change of the VSDA. By measuring the frequency response of the VSDA, the transmissibility and phase angle difference of the input and output acceleration versus sweeping frequency for different input electric currents is obtained.

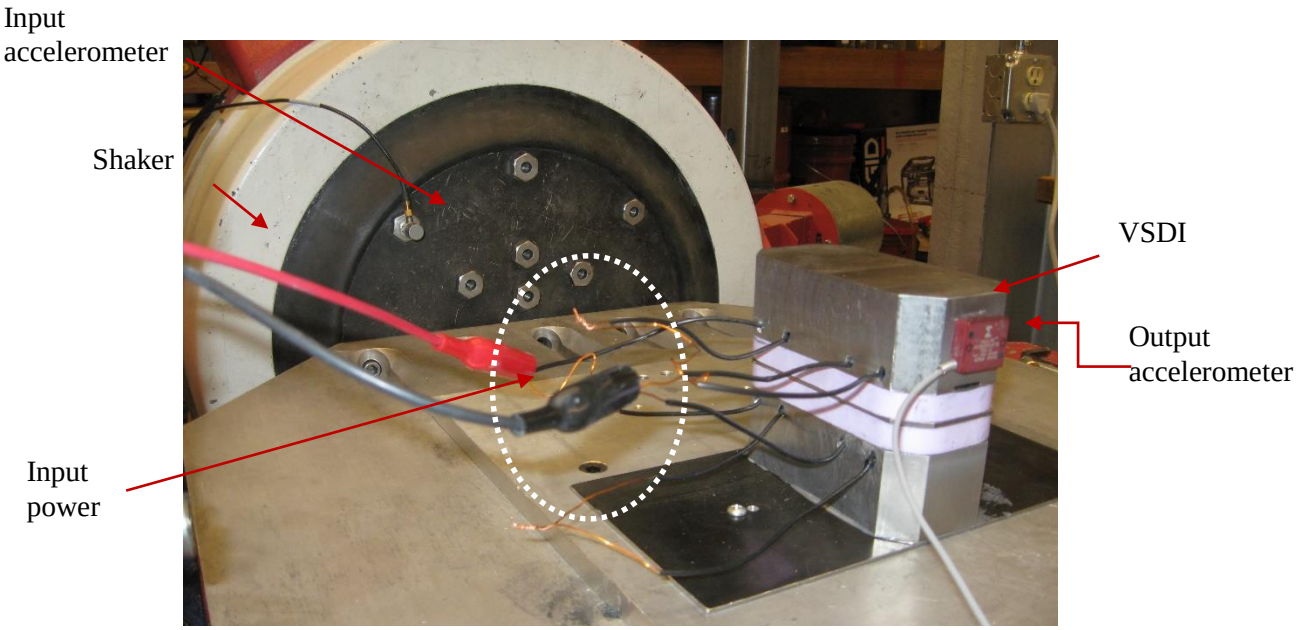

Figure 5.1. Photo of the dynamic shear test experiments

The transmissibility and phase angle difference of input and output acceleration under different input currents are shown in Figure 5.2. As shown in Figure 5.2 a, increasing the input electric current, increases the natural frequency, and hence, the stiffness of the VSDA. Figure 5.2 b shows the increase in the phase angle with input electric current which shows the damping increase in the VSDA. The experimental results demonstrate that the VSDAs are capable of simultaneously increasing their dynamic stiffness and damping 30%, and 10%, respectively [34].

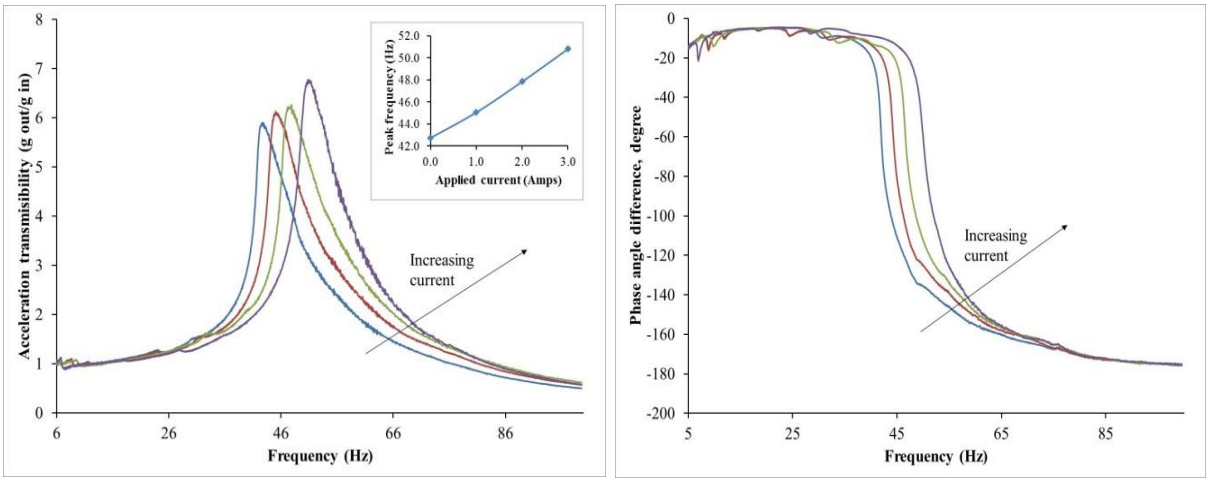

(a) (b)

Figure 5.2. (a) Transmissibility, and (b) Phase angle of 0.1g sinusoidal constant amplitude acceleration input for input electric currents ranging from 0 to 3 Amps. The insert in Figure 2 (a) represents peak frequency vs. input electric current.

To use the VSDAs along with a control system, their force-displacement relationship is developed using a phenomenological model [156]. The model is used to predict the force exerted by VSDAs and parameters of the model are identified from experimental data. The model can take into account the effect of the field-dependent stiffness along with the damping and hysteresis behavior of the MREs.

5.3. The Isolated Scaled Building

To demonstrate feasibility of utilizing the proposed VSDA for structural control, four prototype VSDAs and a 1:16 scaled two-story building with adjustable mass are fabricated. The two-story scaled building is fixed on the upper part of the VSDAs and the VSDAs are installed

on a Ling Dynamic Systems shake table. The total weight of the structure and the four top caps of the VSDAs is 68 kg. All masses and dimensions are scaled down with appropriate scaling factors based on the design procedures [157]. The first mode frequency of the isolated scaled building can be shifted from 11.59 Hz to 13.39 Hz with 2 Amps input current; which corresponds to 32.78 % increase in the stiffness of the system. A photo of the experimental setup is shown in Figure 5.3. Four accelerometers with a maximum range of ±2g are calibrated and installed on the three floors of the scaled building and the slip plate.

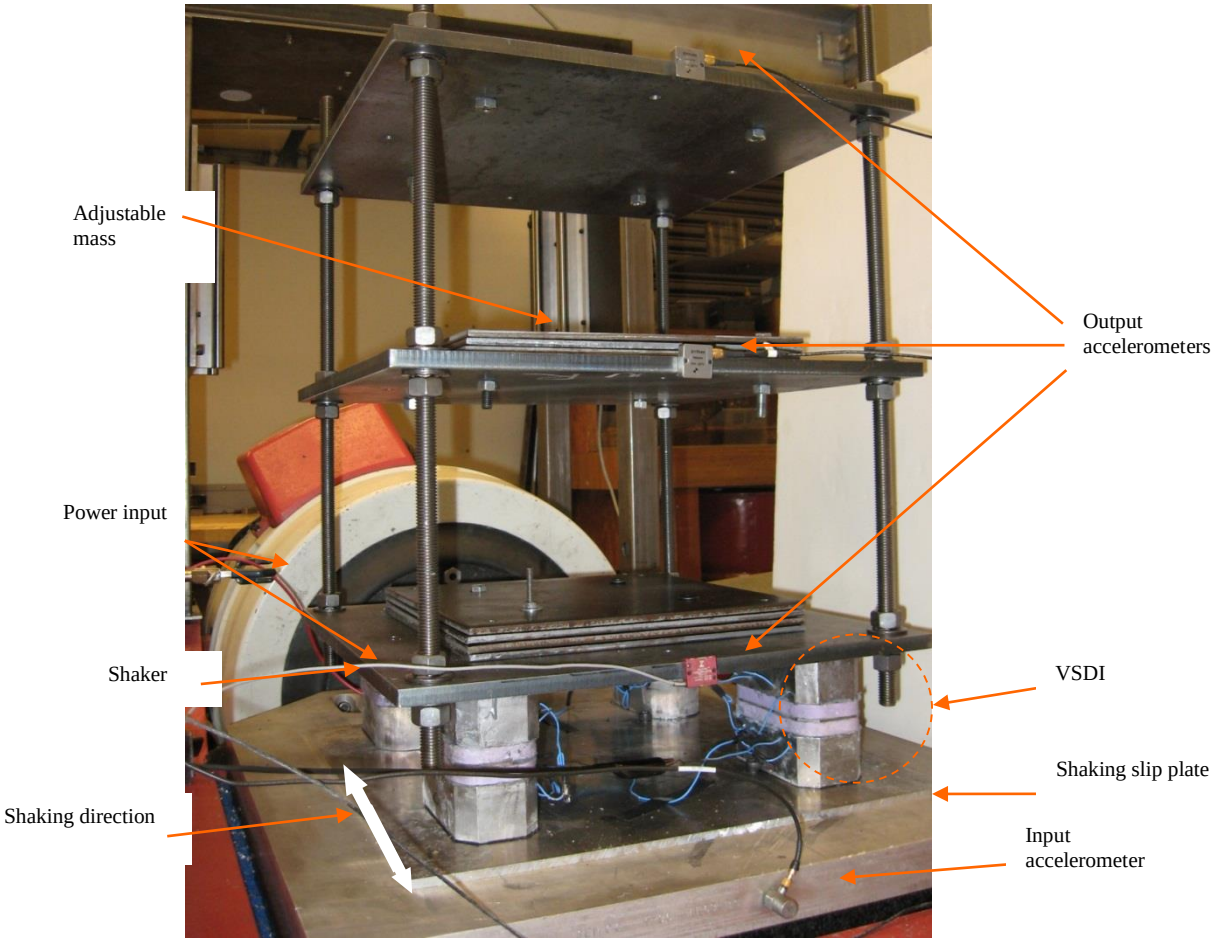

Figure 5.3. Photo of the experimental setup.

The governing equations of the system are:

$$m_1\ddot{x}_1 + (c_1 + c_2)\dot{x}_1 - c_2\dot{x}_1 + (k_1 + k_2)x_1 - k_1x_1 = -m_1\ddot{x}_g + f_{VSDI}$$

$$\mathrm{m_1\ddot{x}_1 + (c_1 + c_2)\dot{x}_1\text{-}c_2\dot{x}_1 + (k_1 + k_2)x_1\text{-}k_1x_1 = \text{-}m_1\ddot{x}_g + f_{VSDI}}$$

$$m_2\ddot{x}_2 - c_2\dot{x}_1 + (c_2 + c_3)\dot{x}_2 - c_3\dot{x}_3 - k_3x_1 + (k_2 + k_3)x_2 - k_3x_3 = -m_2\ddot{x}_g$$

$$m_3\ddot{x}_3 - c_3\dot{x}_2 + c_3\dot{x}_3 - k_3x_2 + k_3x_3 = -m_3\ddot{x}_g$$

$$M\ddot{X} + C\dot{X} + KX = M\ddot{x}_g + LF_{VSDI} \quad \mathrm{M\ddot{X} + KX + C\dot{X} = M\ddot{x}_g + LF_{VSDI}} \tag{6}$$

where:

$$X = [x_1, x_2, x_3]^T, M = \begin{bmatrix} m_1 & 0 & 0 \\ 0 & m_2 & 0 \\ 0 & 0 & m_3 \end{bmatrix}, C = \begin{bmatrix} c_2 & -c_2 & 0 \\ -c_2 & c_2 + c_3 & -c_3 \\ 0 & -c_3 & c_3 \end{bmatrix}, K = \begin{bmatrix} k_2 & -k_2 & 0 \\ -k_2 & k_2 + k_3 & -k_3 \\ 0 & -k_3 & k_3 \end{bmatrix},$$

$$L = [1,0,0]^T \tag{7}$$

where M is the mass matrix, C is the damping matrix, K is the stiffness matrix of the building and $\ddot{x}_g$ is the ground acceleration. The mass of the first floor with the four VSDAs' top parts is $m_1 = 28kg$ $\mathrm{m_1 = 28kg}$ and the rest of the floors are $m_2 = m_3 = 20kg$ $\mathrm{m_2 = m_3 = 20kg}$. k_1 $\mathrm{k_1}$

is zero since it is already considered in the force modeling of VSDAs. k_2 and k_3 are equal to $1.01e6N/m$. Similarly, the damping c_1 is considered to be zero and damping $c_2 = c_3 = 18N.s/m$ $c_2 = c_3 = 18$ is obtained from the damping of the structural steel.

5.4. Lyapunov-Based Controller

Increasing the damping and stiffness of the VSDAs in a passive manner may not be beneficial for the seismic response reduction of the scaled building during all types of seismic events. An appropriate control strategy with the ability to tune the properties of VSDAs may ensure better response for different seismic conditions. Acceleration inputs are selected as inputs for the controller since acceleration measurement is more manageable than displacement measurement especially during a seismic event [109]. The remaining variables for the control application including displacements and forces can be computed from the acceleration measurements using appropriate data acquisition and filtering techniques. Before testing, accuracy of the derived variables is verified with displacement sensors. The state-space equation of the two-story scaled building can be written, as follows:

$$\dot{z} = Az + Bf_{VSDI} + E\ddot{x}_g \tag{8}$$

where:

$$A=\begin{bmatrix} 0 & I \\ -M^{-1}K & -M^{-1}C \end{bmatrix} \text{A} = \begin{bmatrix} 0 & \text{I} \\ \text{-M}^{-1}\text{K} & \text{-M}^{-1}\text{C} \end{bmatrix},\ B=\begin{bmatrix} 0 \\ -M^{-1}L \end{bmatrix},\ E=\begin{bmatrix} 0 \\ \Lambda \end{bmatrix} \qquad \text{B} = \begin{bmatrix} 0 \\ \Lambda \end{bmatrix} \tag{9}$$

The state vector z is defined as $z=[x_1, x_2, x_3, \dot{x}_1, \dot{x}_2, \dot{x}_3]^T$ $\text{z} = [\text{z}_1, \text{z}_2, \text{z}_3, \dot{\text{z}}_1, \dot{\text{z}}_2, \dot{\text{z}}_3]^{\text{T}}$ and $\Lambda=[1,1,1]^T$ $\Lambda = [1,1,1]^{\text{T}}$..

For the present application, a Lyapunov-based control strategy is used since it is robust and time delay does not affect it [158], it can minimize transferred energy to the structure and can be used for both linear and nonlinear systems. The Lyapunov function can be expressed as:

$$V(z)=z^T Rz \tag{10}$$

where, R is the solution of the following equation:

$$AR+A^T R=-Q \tag{11}$$

Therefore, the derivative of the Lyapunov function for the isolated scaled building can be written as:

$$\dot{V}(z)=-0.5z^T Qz+z^T RBf_{VSDI}+z^T RE\ddot{x}_g \tag{12}$$

The following equation, which defines the input voltage base on the force measurement, can minimize the$\dot{V}(z)$[111].

$$v_{control} = V_{\max} H\left(-z^T RBf_{VSDI}\right) \tag{13}$$

where, *H* is the Heaviside step function and matrix *R* contains the control tuning factors. The scaled building equations along with the VSDA force modeling in the SIMULINK is used to simulate the control testing. The control voltage from Equation (13) is fed to the current-dependent stiffness, damping and hysteresis sub-models to control the VSDA behavior.

5.5. Simulation of Controlled Isolated Scaled Building

A SIMULINK model combined with a MATLAB code is developed to implement the state-space equations of the building. The SIMULINK model shown in Figure 5.4 is used both for simulation and experiments. The difference is in the acceleration time history which is generated by computer for the simulation and is measured via accelerometers for the experiments. Also, the control signal is fed to the power supplies in the experiments. The Lyapunov control strategy is implemented in the controller part of the model. The controller needs to be tuned with appropriate *R* values to achieve the largest reduction in accelerations and displacements.

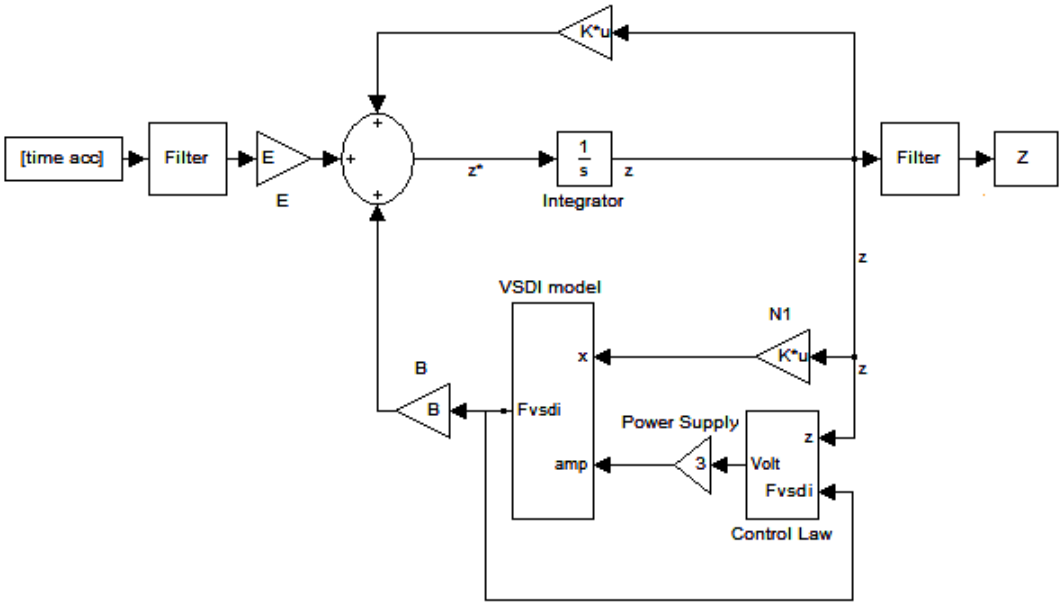

Figure 5.4. SIMULINK model of the controlled isolated scaled building.

To obtain the appropriate R values through simulation, the scaled El Centro EW seismic excitation is applied as the input to the model. The El Centro earthquake is selected since it consists of a wide frequency range. Using a MATLAB code, the 1:16 scaled seismic acceleration excitation and its power spectrum density are obtained for input to the simulation and experiments, as shown in Figure 5.5. As can be seen, the maximum power spectrum density of the scaled El Centro EW excitation occurs about 7Hz which is close to the frequency of the first mode of the isolated structure (11.59Hz). An appropriate control strategy has the potential to significantly reduce the response of the scaled building and potentially a full-scale structure.

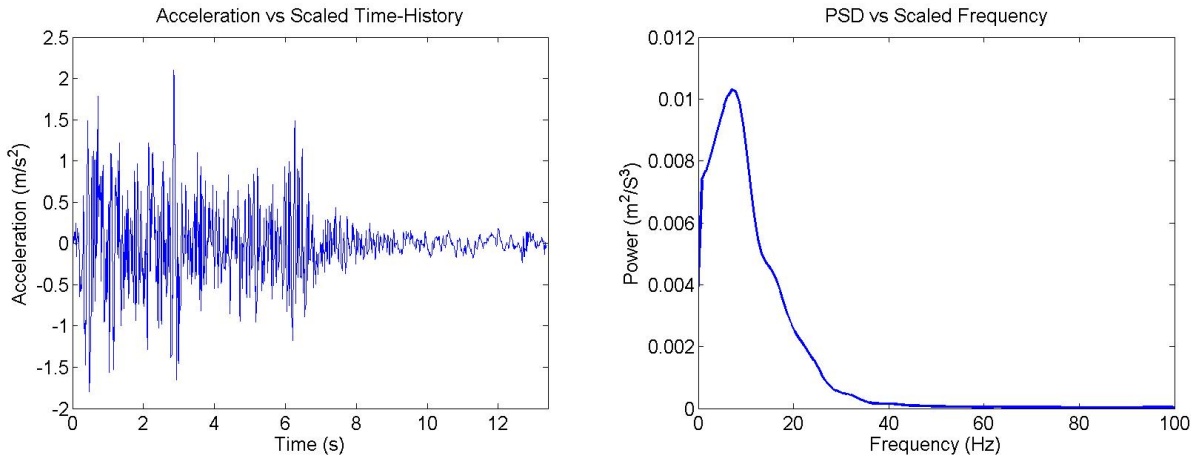

(a) (b)

Figure 5.5. The scaled El Centro earthquake EW (a) acceleration, (b) power spectrum density.

The simulation results of the comparison between controlled and passive absorbers are shown in Figure 5.6. Since the highest floor usually has the maximum acceleration and displacement, only the third floor results are presented here. It is demonstrated that controlling the VSDAs can simultaneously reduce the maximum displacement and acceleration of the third floor, and hence the entire scaled building. With the present controller design, the maximum acceleration of the third floor is reduced by 22% while the maximum displacement is reduced by 58%, theoretically.

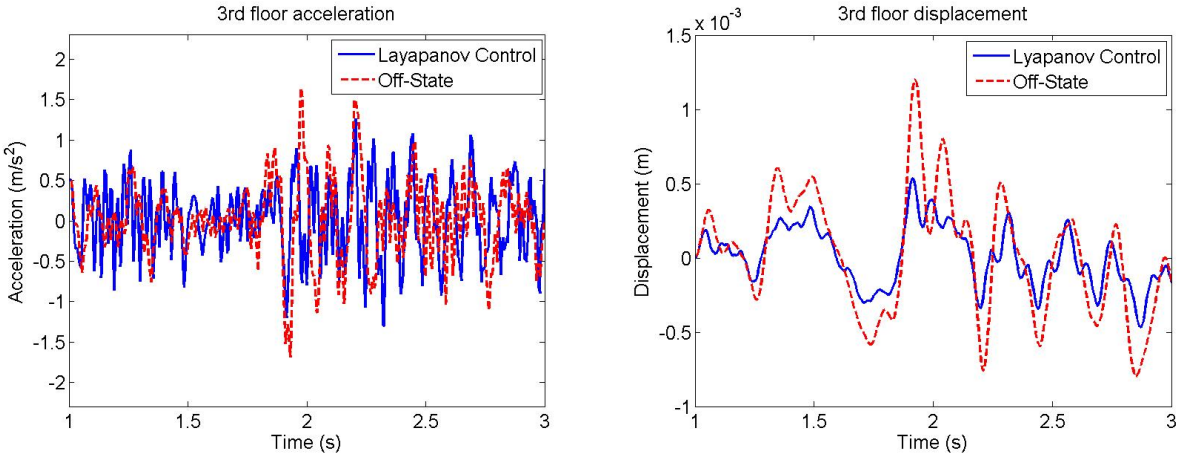

(a) (b)

Figure 5.6. Passive and controlled: (a) acceleration, and (b) displacement of the third floor.

5.6. Experimental Study

The controller design, which is derived from the control simulation, is used to control the VSDAs. The control signal turns on and off the power supplies and controls the mechanical properties of the VSDAs. The scaled El-Centro EW is inputted to the shake table. The calculated Power Spectrum Density (PSD) for the shake table input may generate slightly different acceleration in the shake table. Also, the results of the experiments can vary from the simulation because of the VSDAs and the scaled building fabrication process. As shown in Figure 5.7 and Figure 5.8 the applications of passive VSDAs reduce the maximum acceleration of the third floor of the scaled building while it increases the maximum displacement compared to the fixed base condition. The on-state VSDAs reduce the maximum acceleration and displacement compared to the passive state. Finally, controlling VSDAs

reduces the maximum acceleration while increasing the maximum displacement compared to the on state. This indicates that the controlled state results in reduction of acceleration and displacement. Another advantage of using the control strategy is less power consumption compared to the on state, since the integration of the control signal shows that 17% less power is consumed by the controlled VSDAs compared to on-state. The present control strategy absorbs the transferred energy by slightly increaing the dispalcement of the stucture.

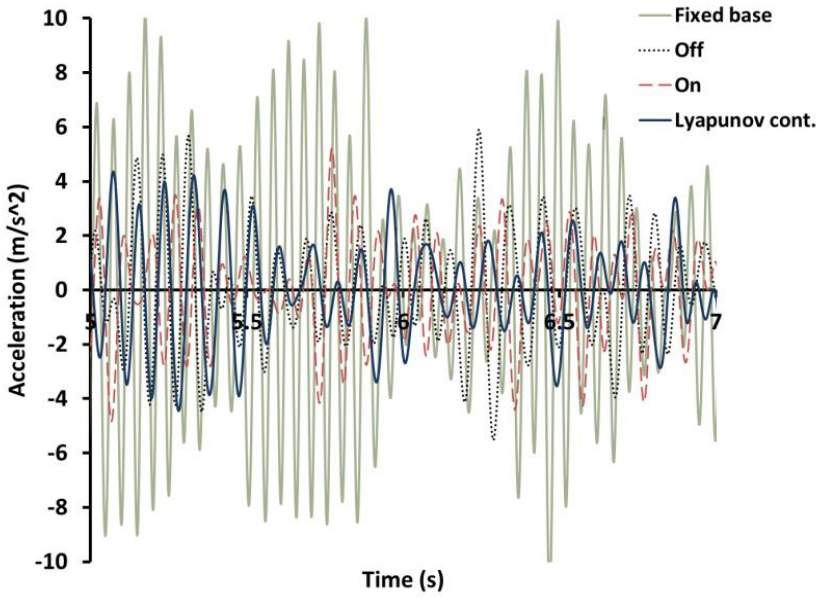

Figure 5.7. Typical results of the effect of VSDAs and control strategy on the third floor acceleration.

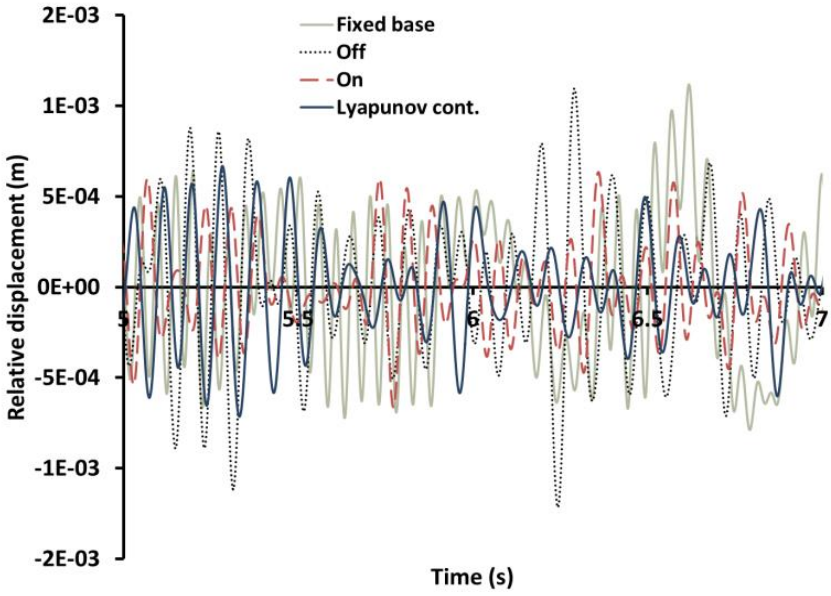

Figure 5.8. Typical results of the effect of VSDAs and control strategy on the relative displacement of the third floor.

To better understand the performance of the VSDAs and the control strategy, acceleration and displacement PSD of the third floor are explored. PSD can be used to demostrate the absorption of energy in different VSDA conditions. The PSD of the third floor acceleration is shown in Figure 5.9 (a), and Figure 5.9 (b) shows the PSD of the third floor displacement. As can be seen, the on-state reduces the transferred power compared to other cases, because VSDAs consume and absorb maximum power and energy in this case.

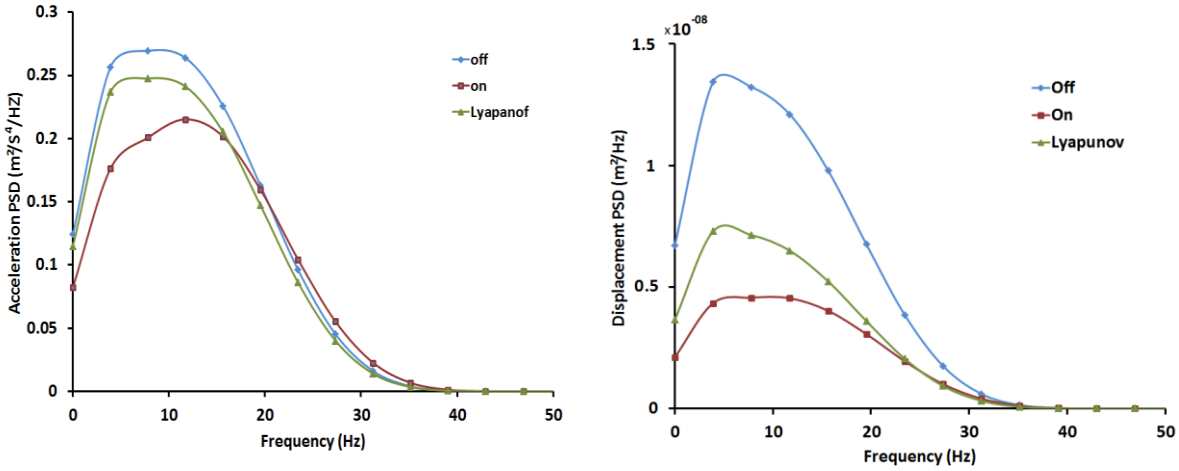

(a) (b)

Figure 5.9. Power spectrum density of acceleration and displacement.

Maximum relative acceleration and displacement as well as absolute acceleration and displacement also help to understand how the controller functions. Figure 5.10 (a) demonstrates that the control strategy reduces the maximum relative acceleration of the floors and Figure 5.10 (b) shows that this is possible by slightly increasing the maximum relative displacement of the floors. As can be seen in Figure 5.11 (a), as the floor number increases, the controlled condition shows better results of absolute acceleration reduction while in Figure 5.11 (b) absolute displacements of the floors remain almost constant for on-state and controlled condition.

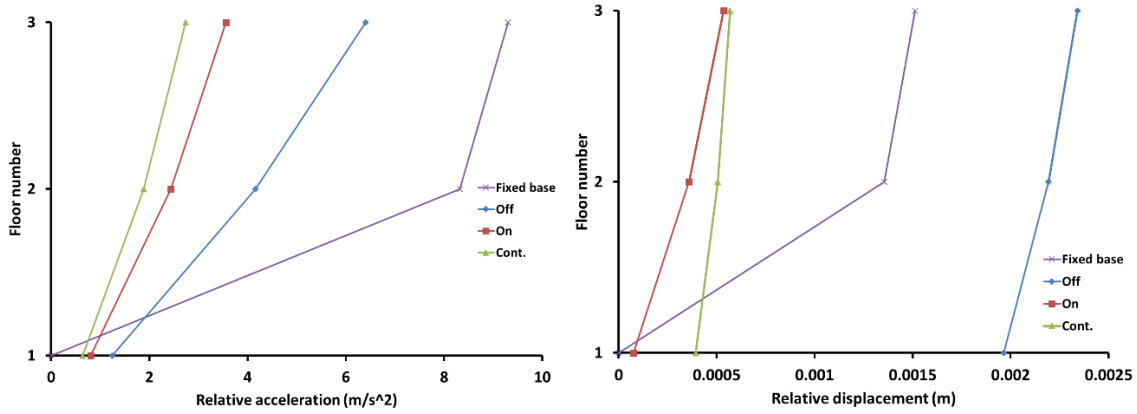

(a) (b)

Figure 5.10. Maximum relative (a) acceleration and (b) displacement of the scaled building.

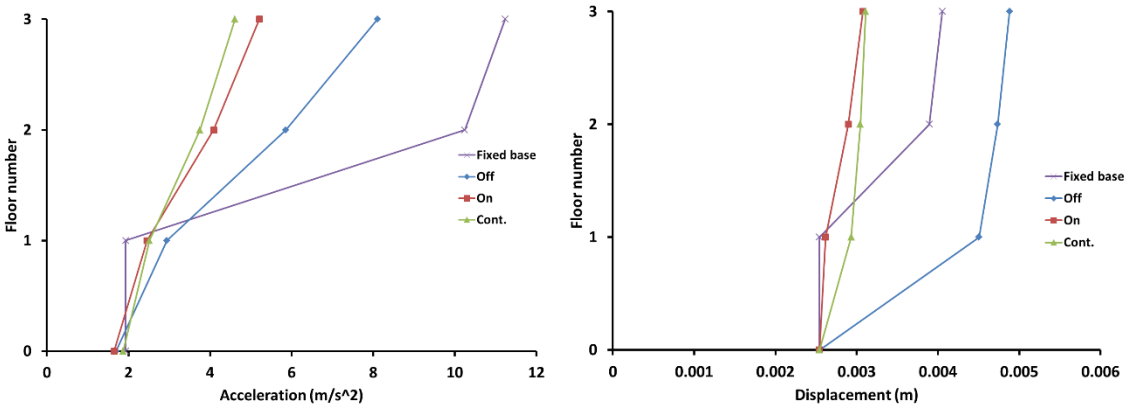

(a) (b)

Figure 5.11. Maximum absolute (a) acceleration and (b) displacement of the scaled building.

To summarize, Table 5.1 lists the maximum acceleration and desplacement reduction in percentage. It should be noted that sizes, number of floors and the control strategy is different in this research than the one that is compared to [78].

Table 5.1. Comparison of the scaled building percentage of maximum absolute acceleration and displacement changes.

	Passive to fixed base	On to passive	Controlled to on	Controlled to passive	Controlled to passive [78]
Top floor acceleration	27.8	35.8	11.5	47.3	39
Top floor displacement	-20.4	35.4	0	35.4	41

5.7. Summary and Conclusions

A previously developed phenomenological model is used to predict the behavior of MRE-based VSDAs. In this study that model along with the equations of motion is utilized to develop a Lyapunov-based control strategy for seismic control of a 1:16 scaled two-story structure. The scaled building response is simulated using a model of the semi-actively isolated scaled building to tune the controller. The feedback controller is optimized to achieve maximum reduction in acceleration and displacement of the scaled building using simulations. Simulation results demonstrate reduction in both acceleration and displacement of the structure by implementing the designed controller. A 1:16 scaled two-story building supported by four VSDA absorbers is designed and fabricated for the experimental study. The control scheme with the tuned values is utilized for the VSDAs subjected to the scaled El Centro EW input motion. Comparisons of fixed-base, off-state, on-state and controlled VSDAs conditions show that passive VSDAs significantly reduce the acceleration while slightly increase the

displacement. Therefore, the fail-safe characteristic of the VSDAs ensures that in the event of a power outage, the VSDAs operate in the passive mode. The on and controlled states reduce the maximum acceleration and displacement more than passive state. Moreover, less power is consumed by the controlled VSDAs compared to passive on-state. Therefore, the controlled VSDAs can be desirable since its performance is close to on-state while it is more energy efficient. Comparison of maximum acceleration and displacement of different floors show that by controlling VSDAs, the acceleration is reduced at the cost of a small increase in the displacement.

CHAPTER 6

SUMMARY, CONCLUSIONS AND FUTURE WORK

6.1. Summary and Conclusions of CFMFTS

A unique controllable flexible magnetically-actuated fluid transport system (CFMFTS) was modeled, and numerically analyzed. The flexible microchannel is made of a soft magnetorheological elastomer membrane. A model with combined magnetic, elastic, and fluid domains was created and was numerically solved using COMSOL multi-physics finite element package. The results for the passive system (no magnetic field applied) showed good agreement with a published analytical solution. Using two-dimensional analyses, the effect of magnetic induced force on the microchannel's wall was investigated for valveless and valved configurations to examine the volume flow rate that such a system can propel. The effect of each system parameter was investigated on the performance of the system individually and finally three-dimensional analyses were performed to account for asymmetric deflection of the tube. Results successfully demonstrated the capability of the system to propel fluid, when the parameters are designed appropriately.

6.2. Future Work for CFMFTS

All studies for this dissertation were carried out using 1 Hz loading frequency. Since the operating frequency is important for micropumps [159], the effect of frequency on the propulsion capability of CFMFTS can be investigated. The effect of large deformation on the

moving mesh method also needs to be investigated. Performance and flow resistance of the valves should be investigated in more detail. A comprehensive experimental study needs to be conducted to study the system parameters to validate the numerical results.

6.3. Summary and Conclusions of VSDA

A novel variable stiffness and damping absorber (VSDA) was designed, built and tested under quasi-static and dynamic shear loading. Results of the dynamic experiments showed that both stiffness and damping of the system changes under the application of a magnetic field. Significant variations in stiffness and damping of the VSDA were observed due to changes in properties of MREs under a magnetic field. The increased stiffness results in shifting natural frequency to the right, and the increased damping results in a decrease in peak amplitude of the transmissibility. A phenomenological model that can capture the behavior of the VSDA was developed and related parameters were identified using experimental data through shake table experiments. This model was implemented into a 1:16 scaled two-story building system to develop a Lyapunov-based control strategy for the seismic control of the structure. Predictions of the scaled building responses utilizing VSDAs and the proposed controller were investigated. Simulation results showed that reduction in both acceleration and displacement of the structure relative to off-state is possible using the designed controller based on Lyapunov control strategy for El Centro EW scaled acceleration input. In addition, a two-story scaled building supported by four VSDA absorbers was designed, built and tested. The proposed control strategy was used to semi-actively control the VSDA behavior under seismic El-Centro EW vibrations.

Controlled testing results show that less power is consumed and maximum acceleration is reduced further when the VSDAs are controlled compared to on-state.

6.4. Future Work for VSDA

For future works, arrangement of the VSDAs and the thickness of the VSDAs for a full-scale building can be investigated. The possibility of utilizing more VSDAs but smaller in size vs. fewer VSDAs but larger in size can have a significant effect on the rocking of the building that may be considered.

References

1. Hirata, Y., Kaneko, N., Moriwaki, M., & Oura, K. (1996, August 27). Artificial blood vessel. Retrieved from http://www.google.com/patents?id=lF8hAAAAEBAJ

2. Shimizu, Y. (2000, October 24). Artificial blood vessel. Retrieved from http://www.google.com/patents?id=y3kFAAAAEBAJ

3. Wakabayashi, S., Hashimukai, T., Katakura, T., & Takano, Y. (1996, August 13). Artificial blood vessel. Retrieved from http://www.google.com/patents?id=OgEaAAAAEBAJ

4. Jones, P. A. (1979). Construction of an artificial blood vessel wall from cultured endothelial and smooth muscle cells. *Proceedings of the National Academy of Sciences, 76*(4), 1882–1886. Retrieved from http://www.pnas.org/content/76/4/1882

5. Kakisis, J. D., Liapis, C. D., Breuer, C., & Sumpio, B. E. (2005). Artificial blood vessel: The Holy Grail of peripheral vascular surgery. *Journal of Vascular Surgery*, *41*(2), 349–354. doi:10.1016/j.jvs.2004.12.026

6. Kim, D.-J., Baek, I.-S., Gim, C.-S., & Kim, S.-H. (2011, July 21). Implantable Tube And Coating Method Thereof. Retrieved from http://www.google.com/patents?id=UfLoAQAAEBAJ

7. Margaris, K. N., & Black, R. A. (2012). Modelling the lymphatic system: challenges and opportunities. *Journal of The Royal Society Interface*, *9*(69), 601–612. doi:10.1098/rsif.2011.0751

8. Dixon, J. B., Greiner, S. T., Gashev, A. A., Cote, G. L., Moore, J. E., & Zawieja, D. C. (2006). Lymph flow, shear stress, and lymphocyte velocity in rat mesenteric prenodal

lymphatics. *Microcirculation (New York, N.Y.: 1994)*, *13*(7), 597–610. doi:10.1080/10739680600893909

9. Rahbar, E., & Moore, J. E., Jr. (2011). A model of a radially expanding and contracting lymphangion. *Journal of biomechanics*, *44*(6), 1001–1007. doi:10.1016/j.jbiomech.2011.02.018

10. Jamalian, S., Bertram, C. D., Richardson, W. J., & Moore, J. E. (2013). Parameter sensitivity analysis of a lumped-parameter model of a chain of lymphangions in series. *American Journal of Physiology - Heart and Circulatory Physiology*, *305*(12), H1709–H1717. doi:10.1152/ajpheart.00403.2013

11. Galie, P., & Spilker, R. L. (2009). A Two-Dimensional Computational Model of Lymph Transport Across Primary Lymphatic Valves. *Journal of Biomechanical Engineering*, *131*(11), 111004–111004. doi:10.1115/1.3212108

12. Leung, J. H., Wright, A. R., Cheshire, N., Crane, J., Thom, S. A., Hughes, A. D., & Xu, Y. (2006). Fluid structure interaction of patient specific abdominal aortic aneurysms: a comparison with solid stress models. *BioMedical Engineering OnLine*, *5*(1), 33. doi:10.1186/1475-925X-5-33

13. Gerbeau, J.-F., & Vidrascu, M. (2003). A Quasi-Newton Algorithm Based on a Reduced Model for Fluid-Structure Interaction Problems in Blood Flows. Retrieved from http://hal.inria.fr/inria-00071895

14. Torii, R., Oshima, M., Kobayashi, T., Takagi, K., & Tezduyar, T. E. (2006). Fluid–structure Interaction Modeling of Aneurysmal Conditions with High and Normal Blood Pressures. *Computational Mechanics*, *38*(4-5), 482–490. doi:10.1007/s00466-006-0065-6

15. Bazilevs, Y., Calo, V. M., Zhang, Y., & Hughes, T. J. R. (2006). Isogeometric Fluid–structure Interaction Analysis with Applications to Arterial Blood Flow. *Computational Mechanics*, *38*(4-5), 310–322. doi:10.1007/s00466-006-0084-3

16. Bathe, M., & Kamm, R. D. (1999). A Fluid-Structure Interaction Finite Element Analysis of Pulsatile Blood Flow Through a Compliant Stenotic Artery. *Journal of Biomechanical Engineering*, *121*(4), 361. doi:10.1115/1.2798332

17. Di Martino, E. S., Guadagni, G., Fumero, A., Ballerini, G., Spirito, R., Biglioli, P., & Redaelli, A. (2001). Fluid–structure interaction within realistic three-dimensional models of the aneurysmatic aorta as a guidance to assess the risk of rupture of the aneurysm. *Medical Engineering & Physics*, *23*(9), 647–655. doi:10.1016/S1350-4533(01)00093-5

18. Kalinowski, A. J. (1975). Fluid structure interaction. *Shock Vibration Information Center Shock Vibration Computer Programs*, *-1*, 405–452. Retrieved from http://adsabs.harvard.edu/abs/1975SVICP.....405K

19. Belytschko, T. (1980). Fluid-structure interaction. *Computers & Structures*, *12*(4), 459–469. doi:10.1016/0045-7949(80)90121-2

20. Mathews, I. C. (1986). Numerical techniques for three-dimensional steady-state fluid–structure interaction. *The Journal of the Acoustical Society of America*, *79*(5), 1317–1325. doi:10.1121/1.393711

21. Dowell, E. H., & Hall, K. C. (2001). Modeling of Fluid-Structure Interaction. *Annual Review of Fluid Mechanics*, *33*(1), 445–490. doi:10.1146/annurev.fluid.33.1.445

22. Hübner, B., Walhorn, E., & Dinkler, D. (2004). A monolithic approach to fluid–structure interaction using space–time finite elements. *Computer Methods in Applied Mechanics and Engineering*, *193*(23–26), 2087–2104. doi:10.1016/j.cma.2004.01.024

23. Heil, M. (2004). An efficient solver for the fully coupled solution of large-displacement fluid–structure interaction problems. *Computer Methods in Applied Mechanics and Engineering*, *193*(1–2), 1–23. doi:10.1016/j.cma.2003.09.006

24. Souli, M., Ouahsine, A., & Lewin, L. (2000). ALE formulation for fluid–structure interaction problems. *Computer Methods in Applied Mechanics and Engineering*, *190*(5–7), 659–675. doi:10.1016/S0045-7825(99)00432-6

25. Hron, J., & Turek, S. (2006). A Monolithic FEM/Multigrid Solver for an ALE Formulation of Fluid-Structure Interaction with Applications in Biomechanics. In H.-J. Bungartz & M. Schäfer (Eds.), *Fluid-Structure Interaction* (pp. 146–170). Springer Berlin Heidelberg. Retrieved from http://link.springer.com/chapter/10.1007/3-540-34596-5_7

26. Zhang, Q., & Hisada, T. (2001). Analysis of fluid–structure interaction problems with structural buckling and large domain changes by ALE finite element method. *Computer Methods in Applied Mechanics and Engineering*, *190*(48), 6341–6357. doi:10.1016/S0045-7825(01)00231-6

27. Farhat, C., Lesoinne, M., & Le Tallec, P. (1998). Load and motion transfer algorithms for fluid/structure interaction problems with non-matching discrete interfaces: Momentum and energy conservation, optimal discretization and application to aeroelasticity. *Computer Methods in Applied Mechanics and Engineering*, *157*(1–2), 95–114. doi:10.1016/S0045-7825(97)00216-8

28. Le Tallec, P., & Mouro, J. (2001). Fluid structure interaction with large structural displacements. *Computer Methods in Applied Mechanics and Engineering*, *190*(24–25), 3039–3067. doi:10.1016/S0045-7825(00)00381-9

29. Wall, W. A., Gerstenberger, A., Gamnitzer, P., Förster, C., & Ramm, E. (2006). Large Deformation Fluid-Structure Interaction – Advances in ALE Methods and New Fixed Grid Approaches. In H.-J. Bungartz & M. Schäfer (Eds.), *Fluid-Structure Interaction* (pp. 195–232). Springer Berlin Heidelberg. Retrieved from http://link.springer.com/chapter/10.1007/3-540-34596-5_9

30. Barham, M., Steigmann, D. J., McElfresh, M., & Rudd, R. E. (2007). Finite deformation of a pressurized magnetoelastic membrane in a stationary dipole field. *Acta Mechanica*, *191*(1-2), 1–19. doi:10.1007/s00707-007-0445-9

31. Raikher, Y. L., Stolbov, O. V., & Stepanov, G. V. (2008). Shape instability of a magnetic elastomer membrane. *Journal of Physics D: Applied Physics*, *41*(15), 152002. doi:10.1088/0022-3727/41/15/152002

32. Laser, D. J., & Santiago, J. G. (2004). A review of micropumps. *Journal of Micromechanics and Microengineering*, *14*(6), R35. doi:10.1088/0960-1317/14/6/R01

33. Amirouche, F., Zhou, Y., & Johnson, T. (2009). Current micropump technologies and their biomedical applications. *Microsystem Technologies*, *15*(5), 647–666. doi:10.1007/s00542-009-0804-7

34. Iverson, B. D., & Garimella, S. V. (2008). Recent advances in microscale pumping technologies: a review and evaluation. *Microfluidics and Nanofluidics*, *5*(2), 145–174. doi:10.1007/s10404-008-0266-8

35. Khoo, M., & Liu, C. (2001). Micro magnetic silicone elastomer membrane actuator. *Sensors and Actuators A: Physical*, *89*(3), 259–266. doi:10.1016/S0924-4247(00)00559-8

36. Santra, S., Holloway, P., & Batich, C. D. (2002). Fabrication and testing of a magnetically actuated micropump. *Sensors and Actuators B: Chemical*, *87*(2), 358–364. doi:10.1016/S0925-4005(02)00272-1

37. Yamahata, C., Lotto, C., Al-Assaf, E., & Gijs, M. a. M. (2005). A PMMA valveless micropump using electromagnetic actuation. *Microfluidics and Nanofluidics*, *1*(3), 197–207. doi:10.1007/s10404-004-0007-6

38. Shen, M., Dovat, L., & Gijs, M. A. M. (2011). Magnetic active-valve micropump actuated by a rotating magnetic assembly. *Sensors and Actuators B: Chemical*, *154*(1), 52–58. doi:10.1016/j.snb.2009.10.033

39. Wang, Y.-H., Tsai, Y.-W., Tsai, C.-H., Lee, C.-Y., & Fu, L.-M. (2010). Design and Analysis of Impedance Pumps Utilizing Electromagnetic Actuation. *Sensors*, *10*(4), 4040–4052. doi:10.3390/s100404040

40. Hatch, A., Kamholz, A. E., Holman, G., Yager, P., & Böhringer, K. F. (2001). A ferrofluidic magnetic micropump. *Journal of Microelectromechanical Systems*, *10*(2), 215–221. doi:10.1109/84.925748

41. Hartshorne, H., Backhouse, C. J., & Lee, W. E. (2004). Ferrofluid-based microchip pump and valve. *Sensors and Actuators B: Chemical*, *99*(2–3), 592–600. doi:10.1016/j.snb.2004.01.016

42. Lee, C.-Y., Leong, J.-C., Wang, Y.-N., Fu, L.-M., & Chen, S.-J. (2012). A Ferrofluidic Magnetic Micropump for Variable-Flow-Rate Applications. *Japanese Journal of Applied Physics*, *51*(4R), 047201. doi:10.1143/JJAP.51.047201

43. Ullakko, K., Wendell, L., Smith, A., Müllner, P., & Hampikian, G. (2012). A magnetic shape memory micropump: contact-free, and compatible with PCR and human DNA profiling. *Smart Materials and Structures*, *21*(11), 115020. doi:10.1088/0964-1726/21/11/115020

44. LaRocque, J., Meehan, E., Wentling, C., Jenkins, C., & Woo, K. (n.d.). Membrane Reflector Shape Control Using a Bio-Inspired MRF-Foam Actuator. In *51st AIAA/ASME/ASCE/AHS/ASC Structures, Structural Dynamics, and Materials Conference*. American Institute of Aeronautics and Astronautics. Retrieved from http://arc.aiaa.org/doi/abs/10.2514/6.2010-2910

45. Gray, B. L. (2014). A Review of Magnetic Composite Polymers Applied to Microfluidic Devices. *Journal of The Electrochemical Society*, *161*(2), B3173–B3183. doi:10.1149/2.023402jes

46. Cheng, C.-H., Chao, C., Cheung, Y.-N., Xiao, L., Yang, M., & Leung, W. (2008). A transcutaneous controlled magnetic microvalve based on iron-powder filled PDMS for implantable drug delivery systems. In *3rd IEEE International Conference on Nano/Micro Engineered and Molecular Systems, 2008. NEMS 2008* (pp. 1160–1163). Presented at the 3rd IEEE International Conference on Nano/Micro Engineered and Molecular Systems, 2008. NEMS 2008. doi:10.1109/NEMS.2008.4484523

47. Oh, K. W., & Ahn, C. H. (2006). A review of microvalves. *Journal of Micromechanics and Microengineering*, *16*(5), R13. doi:10.1088/0960-1317/16/5/R01

48. Chu, X. (2004, June 24). Prosthetic valves and methods of manufacturing. Retrieved from http://www.google.com/patents/US20040122515

49. Andersen, H. R., Hasenkam, J. M., & Knudsen, L. L. (2003, June 24). Valve prosthesis for implantation in the body and a catheter for implanting such valve prosthesis. Retrieved from http://www.google.com/patents/US6582462

50. Bergheim, B., Meyers, K., DuMontelle, J., & Nguyen, C. (2006, February 2). Implantable prosthetic valve. Retrieved from http://www.google.com/patents/US20060025857

51. Mohammadi, H., & Mequanint, K. (2011). Prosthetic aortic heart valves: Modeling and design. *Medical Engineering & Physics*, *33*(2), 131–147. doi:10.1016/j.medengphy.2010.09.017

52. Daebritz, S. H., Sachweh, J. S., Hermanns, B., Fausten, B., Franke, A., Groetzner, J., … Messmer, B. J. (2003). Introduction of a Flexible Polymeric Heart Valve Prosthesis With Special Design for Mitral Position. *Circulation*, *108*(10 suppl 1), II–134–II–139. doi:10.1161/01.cir.0000087655.41288.dc

53. Bertram, C. D., Macaskill, C., & Moore, J. E. (2013). Incorporating measured valve properties into a numerical model of a lymphatic vessel. *Computer Methods in Biomechanics and Biomedical Engineering*, *17*(14), 1519–1534. doi:10.1080/10255842.2012.753066

54. De Hart, J., Peters, G. W. M., Schreurs, P. J. G., & Baaijens, F. P. T. (2000). A two-dimensional fluid–structure interaction model of the aortic value. *Journal of Biomechanics*, *33*(9), 1079–1088. doi:10.1016/S0021-9290(00)00068-3

55. De Hart, J., Peters, G. W. M., Schreurs, P. J. G., & Baaijens, F. P. T. (2003). A three-dimensional computational analysis of fluid–structure interaction in the aortic valve. *Journal of Biomechanics*, *36*(1), 103–112. doi:10.1016/S0021-9290(02)00244-0

56. Marom, G., Peleg, M., Halevi, R., Rosenfeld, M., Raanani, E., Hamdan, A., & Haj-Ali, R. (2013). Fluid-Structure Interaction Model of Aortic Valve With Porcine-Specific Collagen Fiber Alignment in the Cusps. *Journal of Biomechanical Engineering*, *135*(10), 101001–101001. doi:10.1115/1.4024824

57. http://www.taiwanpillar.com.tw/. (n.d.).

58. Nagarajaiah, S., & Sahasrabudhe, S. (2006). Seismic response control of smart sliding isolated buildings using variable stiffness systems: an experimental and numerical study. *Earthquake Engineering & Structural Dynamics*, *35*(2), 177–197. doi:10.1002/eqe.514

59. Symans, M. D., & Constantinou, M. C. (1999). Semi-active control systems for seismic protection of structures: a state-of-the-art review. *Engineering Structures*, *21*(6), 469–487. doi:10.1016/S0141-0296(97)00225-3

60. Kobori, T., Takahashi, M., Nasu, T., Niwa, N., & Ogasawara, K. (1993). Seismic response controlled structure with Active Variable Stiffness system. *Earthquake Engineering & Structural Dynamics*, *22*(11), 925–941. doi:10.1002/eqe.4290221102

61. Symans, M. D., & Constantinou, M. C. (1997). Seismic testing of a building structure with a semi-active fluid damper control system. *Earthquake Engineering and Structural Dynamics*, *26*(7), 759–777. doi:10.1002/(SICI)1096-9845(199707)26:7<759::AID-EQE675>3.0.CO;2-E

62. Yang, J. N., Kim, J.-H., & Agrawal, A. K. (2000). Resetting Semiactive Stiffness Damper for Seismic Response Control. *Journal of Structural Engineering*, *126*(12), 1427–1433. doi:10.1061/(ASCE)0733-9445(2000)126:12(1427)

63. Niwa, N., Kobori, T., Takahashi, M., Midorikawa, H., Kurata, N., & Mizuno, T. (2000). Dynamic loading test and simulation analysis of full-scale semi-active hydraulic damper for structural control. *Earthquake Engineering & Structural Dynamics*, *29*(6), 789–812. doi:10.1002/(SICI)1096-9845(200006)29:6<789::AID-EQE933>3.0.CO;2-A

64. Behrooz, M., Sutrisno, J., Wang, X., Fyda, R., Fuchs, A., & Gordaninejad, F. (2011). A new isolator for vibration control. In *Proc. SPIE* (p. 79770Z–79770Z). Presented at the SPIE Smart Structures and Materials+ Nondestructive Evaluation and Health Monitoring. Retrieved from http://proceedings.spiedigitallibrary.org/proceeding.aspx?articleid=729231

65. Carlson, J. D., & Jolly, M. R. (2000). MR fluid, foam and elastomer devices. *Mechatronics*, *10*(4–5), 555–569. doi:10.1016/S0957-4158(99)00064-1

66. Ginder, J. M., Nichols, M. E., Elie, L. D., & Clark, S. M. (2000). Controllable-stiffness components based on magnetorheological elastomers. *Proceedings of SPIE*, *3985*(1), 418–425. doi:10.1117/12.388844

67. Gong, X. L., Chen, L., & Li, J. F. (2007). Study of Utilizable Magnetorheological Elastomers. *International Journal of Modern Physics B*, *21*, 4875–4882. doi:DOI: 10.1142/S0217979207045785

68. Zhang, X., Li, W., & Gong, X. L. (2008). An effective permeability model to predict field-dependent modulus of magnetorheological elastomers. *Communications in Nonlinear Science and Numerical Simulation*, *13*(9), 1910–1916. doi:10.1016/j.cnsns.2007.03.029

69. Carlson, J. (2000). MR fluid, foam and elastomer devices. *Mechatronics*, *10*(4-5), 555–569. doi:10.1016/S0957-4158(99)00064-1

70. Yang, J., Gong, X., Deng, H., Qin, L., & Xuan, S. (2012). Investigation on the mechanism of damping behavior of magnetorheological elastomers. *Smart Materials and Structures*, *21*(12), 125015. doi:10.1088/0964-1726/21/12/125015

71. Chen, L., Gong, X., & Li, W. (2008). Damping of Magnetorheological Elastomers. *Chinese Journal of Chemical Physics*, *21*(6), 581. doi:10.1088/1674-0068/21/06/581-585

72. Hoang, N., Zhang, N., & Du, H. (2011). An adaptive tunable vibration absorber using a new magnetorheological elastomer for vehicular powertrain transient vibration reduction. *Smart Materials and Structures*, *20*(1), 015019. doi:10.1088/0964-1726/20/1/015019

73. Du, H., Li, W., & Zhang, N. (2011). Semi-active variable stiffness vibration control of vehicle seat suspension using an MR elastomer isolator. *Smart Materials and Structures*, *20*(10), 105003. doi:10.1088/0964-1726/20/10/105003

74. Böse, H., Rabindranath, R., & Ehrlich, J. (2012). Soft magnetorheological elastomers as new actuators for valves. *Journal of Intelligent Material Systems and Structures*, *23*(9), 989–994. doi:10.1177/1045389X11433498

75. Guðmundsson, Í. (2011). *A Feasibility Study of Magnetorheological Elastomers for a Potential Application in Prosthetic Devices*. University of Iceland.

76. Usman, M., Sung, S. H., Jang, D. D., Jung, H. J., & Koo, J. H. (2009). Numerical investigation of smart base isolation system employing MR elastomer. *Journal of Physics: Conference Series*, *149*, 012099. doi:10.1088/1742-6596/149/1/012099

77. Koo, J. H., Jang, D. D., Usman, M., & Jung, H. J. (2009). A feasibility study on smart base isolation systems using magneto-rheological elastomers. *Structural Engineering and Mechanics*, *32*(6), 755–770.

78. Jung, H.-J., Eem, S.-H., Jang, D.-D., & Koo, J.-H. (2011). Seismic Performance Analysis of A Smart Base-isolation System Considering Dynamics of MR Elastomers. *Journal of Intelligent Material Systems and Structures*, *22*(13), 1439–1450. doi:10.1177/1045389X11414224

79. Ginder, J. M., Schlotter, W. F., & Nichols, M. E. (2001). Magnetorheological elastomers in tunable vibration absorbers. *Proceedings of SPIE*, *4331*(1), 103–110. doi:10.1117/12.432694

80. Deng, H., Gong, X., & Wang, L. (2006). Development of an adaptive tuned vibration absorber with magnetorheological elastomer. *Smart Materials and Structures*, *15*(5), N111–N116. doi:10.1088/0964-1726/15/5/N02

81. Kim, Y.-K., Koo, J.-H., Kim, K.-S., & Kim, S. (2011). Developing a real time controlled adaptive MRE-based tunable vibration absorber system for a linear cryogenic cooler. In *2011 IEEE/ASME International Conference on Advanced Intelligent Mechatronics (AIM)* (pp. 287–290). Presented at the 2011 IEEE/ASME International Conference on Advanced Intelligent Mechatronics (AIM). doi:10.1109/AIM.2011.6026978

82. Lerner, A. A., & Cunefare, K. A. (2008). Performance of MRE-based Vibration Absorbers. *Journal of Intelligent Material Systems and Structures*, *19*(5), 551–563. doi:10.1177/1045389X07077850

83. Collette, C., Kroll, G., Saive, G., Guillemier, V., & Avraam, M. (2010). On Magnetorheologic Elastomers for Vibration Isolation, Damping, and Stress Reduction in Mass-

varying Structures. *Journal of Intelligent Material Systems and Structures*, *21*(15), 1463–1469. doi:10.1177/1045389X09357973

84. DONG, X., YU, M., LIAO, C., & CHEN, W. (2009). A new variable stiffness absorber based on magneto-rheological elastomer. *Transactions of Nonferrous Metals Society of China*, *19, Supplement 3*(0), s611–s615. doi:10.1016/S1003-6326(10)60118-5

85. Hoang, N., Zhang, N., & Du, H. (2009). A dynamic absorber with a soft magnetorheological elastomer for powertrain vibration suppression. *Smart Materials and Structures*, *18*(7), 074009. doi:10.1088/0964-1726/18/7/074009

86. Deng, H. X., & Gong, X. L. (2007). Adaptive Tuned Vibration Absorber based on Magnetorheological Elastomer. *Journal of Intelligent Material Systems and Structures*, *18*(12), 1205–1210. doi:10.1177/1045389X07083128

87. Deng, H., & Gong, X. (2008). Application of magnetorheological elastomer to vibration absorber. *Communications in Nonlinear Science and Numerical Simulation*, *13*(9), 1938–1947. doi:10.1016/j.cnsns.2007.03.024

88. Collette, C., Kroll, G., Saive, G., Guillemier, V., Avraam, M., & Preumont, A. (2009). Isolation and damping properties of magnetorheologic elastomers. *Journal of Physics: Conference Series*, *149*, 012091. doi:10.1088/1742-6596/149/1/012091

89. Ni, Z. C., Gong, X. L., Li, J. F., & Chen, L. (2009). Study on a Dynamic Stiffness-tuning Absorber with Squeeze-strain Enhanced Magnetorheological Elastomer. *Journal of Intelligent Material Systems and Structures*, *20*(10), 1195–1202. doi:10.1177/1045389X09104790

90. Opie, S., & Yim, W. (2009). Design and control of a real-time variable stiffness vibration isolator. In *IEEE/ASME International Conference on Advanced Intelligent*

Mechatronics, 2009. AIM 2009 (pp. 380 –385). Presented at the IEEE/ASME International Conference on Advanced Intelligent Mechatronics, 2009. AIM 2009. doi:10.1109/AIM.2009.5229983

91. Liao, G. J., Gong, X. L., Kang, C. J., & Xuan, S. H. (2011). The design of an active–adaptive tuned vibration absorber based on magnetorheological elastomer and its vibration attenuation performance. *Smart Materials and Structures*, *20*(7), 075015. doi:10.1088/0964-1726/20/7/075015

92. Opie, S., & Yim, W. (2011). Design and Control of a Real-Time Variable Modulus Vibration Isolator. *Journal of Intelligent Material Systems and Structures*, *22*(2), 113–125. doi:10.1177/1045389X10389204

93. Behrooz, M., Wang, X., & Gordaninejad, F. (2012). Control of structures featuring a new MRE isolator system. In *Proc. SPIE* (p. 83411I–83411I–9). Presented at the SPIE Smart Structures and Materials+ Nondestructive Evaluation and Health Monitoring. doi:10.1117/12.915828

94. Eem, S. H., Jung, H. J., & Koo, J. H. (2013). Seismic performance evaluation of an MR elastomer-based smart base isolation system using real-time hybrid simulation. *Smart Materials and Structures*, *22*(5), 055003. doi:10.1088/0964-1726/22/5/055003

95. Popp, K. M., Zhang, X. Z., Li, W. H., & Kosasih, P. B. (2009). MRE properties under shear and squeeze modes and applications. *Journal of Physics: Conference Series*, *149*, 012095. doi:10.1088/1742-6596/149/1/012095

96. Isaković, T., Zevnik, J., & Fischinger, M. (2011). Floor response spectra in isolated structures, subjected to earthquakes weaker than the design earthquake—Part II: Isolation with

magnetically controlled elastomeric bearings. *Structural Control and Health Monitoring*, *18*(5), 540–553. doi:10.1002/stc.391

97. Seung-Hyun Eem, Hyung-Jo Jung, & Jeong-Hoi Koo. (2011). Application of MR Elastomers for Improving Seismic Protection of Base-Isolated Structures. *IEEE Transactions on Magnetics*, *47*(10), 2901–2904. doi:10.1109/TMAG.2011.2156771

98. Jung, H.-J., Lee, S.-J., Jang, D.-D., Kim, I.-H., Koo, J.-H., & Khan, F. (2009). Dynamic Characterization of Magneto-Rheological Elastomers in Shear Mode. *IEEE Transactions on Magnetics*, *45*(10), 3930–3933. doi:10.1109/TMAG.2009.2024886

99. Eem, S.-H., Jung, H.-J., & Koo, J.-H. (2012). Modeling of Magneto-Rheological Elastomers for Harmonic Shear Deformation. *IEEE Transactions on Magnetics*, *48*(11), 3080 –3083. doi:10.1109/TMAG.2012.2205140

100. Zhu, J.-T., Xu, Z.-D., & Guo, Y.-Q. (2012). Magnetoviscoelasticity parametric model of an MR elastomer vibration mitigation device. *Smart Materials and Structures*, *21*(7), 075034. doi:10.1088/0964-1726/21/7/075034

101. Li, Y., Li, J., Li, W., & Samali, B. (2013). Development and characterization of a magnetorheological elastomer based adaptive seismic isolator. *Smart Materials and Structures*, *22*(3), 035005. doi:10.1088/0964-1726/22/3/035005

102. Dyke, S. J. (1996). *Acceleration Feedback Control Strategies for Active and Semi-Active Control Systems: Modeling, Algorithm Development, and Experimental Verification*. University of Notre Dame, Notre Dame, IL.

103. Asai, T., Chang, C., & Spencer, B. (0). Real-Time Hybrid Simulation of a Smart Base-Isolated Building. *Journal of Engineering Mechanics*, *0*(0), 04014128. doi:10.1061/(ASCE)EM.1943-7889.0000844

104. Yi, F., Dyke, S. J., Caicedo, J. M., & Carlson, J. D. (1999). Seismic response control using smart dampers (pp. 1022 –1026). Presented at the 1999 American Control Conference, San Diego, CA. doi:10.1109/ACC.1999.783195

105. Pinkaew, T., & Fujino, Y. (2001). Effectiveness of semi-active tuned mass dampers under harmonic excitation. *Engineering Structures*, *23*(7), 850–856. doi:10.1016/S0141-0296(00)00091-2

106. Yoshida, O., & Dyke, S. (2004). Seismic Control of a Nonlinear Benchmark Building Using Smart Dampers. *Journal of Engineering Mechanics*, *130*(4), 386–392. doi:10.1061/(ASCE)0733-9399(2004)130:4(386)

107. Ramallo, J. C., Johnson, E. A., & Spencer, B. F. (2002). "Smart" Base Isolation Systems. *Journal of Engineering Mechanics*, *128*(10), 1088–1099. doi:10.1061/(ASCE)0733-9399(2002)128:10(1088)

108. Spencer, B., & Nagarajaiah, S. (2003). State of the Art of Structural Control. *Journal of Structural Engineering*, *129*(7), 845–856. doi:10.1061/(ASCE)0733-9445(2003)129:7(845)

109. Dyke, S. J., Spencer, B. F., Sain, M. K., & Carlson, J. D. (1996). Modeling and control of magnetorheological dampers for seismic response reduction. *Smart Materials and Structures*, *5*(5), 565–575. doi:10.1088/0964-1726/5/5/006

110. Hiemenz, G. J., Choi, Y. T., & Wereley, N. M. (2003). Seismic Control of Civil Structures Utilizing Semi–Active MR Braces. *Computer-Aided Civil and Infrastructure Engineering*, *18*(1), 31–44. doi:10.1111/1467-8667.t01-1-00297

111. Jansen, L. M., & Dyke, S. J. (2000). Semiactive control strategies for MR dampers: comparative study. *Journal of Engineering Mechanics*, *126*(8), 795–803.

112. Yi, F., Dyke, S. J., Caicedo, J. M., & Carlson, J. D. (1999). Experimental verification of multi-input seismic control strategies for smart dampers. *Mechanics*.

113. Wang, X., & Gordaninejad, F. (2002). Lyapunov-Based Control of a Bridge Using Magneto-Rheological Fluid Dampers. *Journal of Intelligent Material Systems and Structures*, *13*(7-8), 415–419. doi:10.1106/104538902025939

114. Nagarajaiah, S., & Narasimhan, S. (2006). Smart base-isolated benchmark building. Part II: phase I sample controllers for linear isolation systems. *Structural Control and Health Monitoring*, *13*(2-3), 589–604. doi:10.1002/stc.100

115. Breslin, J. W. (n.d.). Mechanical forces and lymphatic transport. *Microvascular Research*. doi:10.1016/j.mvr.2014.07.013

116. Angel, M. (2006). Eight-inch f5 deformable magnetic-membrane mirror (Vol. 6273, p. 62732A–62732A–9). SPIE. doi:10.1117/12.669700

117. Akbari, M., Bahrami, M., & Sinton, D. (2010). Analytical and Experimental Characterization of Flow in Slowly-Varying Cross-Section Microchannels. In *ASME*.

118. Fuchs, A., Zhang, Q., Elkins, J., Gordaninejad, F., & Evrensel, C. (2007). Development and characterization of magnetorheological elastomers. *Journal of Applied Polymer Science*, *105*(5), 2497–2508. doi:10.1002/app.24348

119. Gong, X. L., Zhang, X. Z., & Zhang, P. Q. (2005). Fabrication and characterization of isotropic magnetorheological elastomers. *Polymer Testing*, *24*(5), 669–676. doi:10.1016/j.polymertesting.2005.03.015

120. Ginder, J. M., Nichols, M. E., Elie, L. D., & Tardiff, J. L. (1999). Magnetorheological elastomers: properties and applications. *Proceedings of SPIE*, *3675*(1), 131–138. doi:10.1117/12.352787

121. Wu, J., Gong, X., Fan, Y., & Xia, H. (2010). Anisotropic polyurethane magnetorheological elastomer prepared through in situ polycondensation under a magnetic field. *Smart Materials and Structures*, *19*(10), 105007. doi:10.1088/0964-1726/19/10/105007

122. Chertovich, A. V., Stepanov, G. V., Kramarenko, E. Y., & Khokhlov, A. R. (2010). New Composite Elastomers with Giant Magnetic Response. *Macromolecular Materials and Engineering*, *295*(4), 336–341. doi:10.1002/mame.200900301

123. Davis, L. C. (1999). Model of magnetorheological elastomers. *Journal of Applied Physics*, *85*(6), 3348. doi:10.1063/1.369682

124. Dong, X., Ma, N., Qi, M., Li, J., Chen, R., & Ou, J. (2012). The pressure-dependent MR effect of magnetorheological elastomers. *Smart Materials and Structures*, *21*(7), 075014. doi:10.1088/0964-1726/21/7/075014

125. Behrooz, M., Wang, X., & Gordaninejad, F. (2013). Modeling of a new magnetorheological elastomer-based isolator. In *Proc. SPIE* (p. 86880Z–86880Z). Presented at the SPIE Smart Structures and Materials+ Nondestructive Evaluation and Health Monitoring, San Diego, Ca. doi:10.1117/12.2009946

126. Shen, Y., Golnaraghi, M. F., & Heppler, G. R. (2004). Experimental Research and Modeling of Magnetorheological Elastomers. *Journal of Intelligent Material Systems and Structures*, *15*(1), 27–35. doi:10.1177/1045389X04039264

127. Lokander, M., Reitberger, T., & Stenberg, B. (2004). Oxidation of natural rubber-based magnetorheological elastomers. *Polymer Degradation and Stability*, *86*(3), 467–471. doi:10.1016/j.polymdegradstab.2004.05.019

128. Mrlik, M., Sedlacik, M., Pavlinek, V., Peer, P., Filip, P., & Saha, P. (2013). Magnetorheology of carbonyl iron particles coated with polypyrrole ribbons: The steady shear study. *Journal of Physics: Conference Series*, *412*(1), 012016. doi:10.1088/1742-6596/412/1/012016

129. Sedlacik, M., Pavlinek, V., Vyroubal, R., Peer, P., & Filip, P. (2013). A dimorphic magnetorheological fluid with improved oxidation and chemical stability under oscillatory shear. *Smart Materials and Structures*, *22*(3), 035011. doi:10.1088/0964-1726/22/3/035011

130. Li, J., Gong, X., Zhu, H., & Jiang, W. (2009). Influence of particle coating on dynamic mechanical behaviors of magnetorheological elastomers. *Polymer Testing*, *28*(3), 331–337. doi:10.1016/j.polymertesting.2009.01.008

131. Jiang, W., Yao, J., Gong, X., & Chen, L. (2008). Enhancement in Magnetorheological Effect of Magnetorheological Elastomers by Surface Modification of Iron Particles. *Chinese Journal of Chemical Physics*, *21*(1), 87–92. doi:10.1088/1674-0068/21/01/87-92

132. Fuchs, A., Sutrisno, J., Gordaninejad, F., Caglar, M. B., & Yanming, L. (2010). Surface polymerization of iron particles for magnetorheological elastomers. *Journal of Applied Polymer Science*, *117*(2), 934–942. doi:10.1002/app.31533

133. Yuan, K., Li, Z.-F., LÜ, L.-L., & Shi, X.-N. (2007). Synthesis and characterization of well-defined polymer brushes grafted from silicon surface via surface reversible addition–fragmentation chain transfer (RAFT) polymerization. *Materials Letters*, *61*(10), 2033–2036. doi:10.1016/j.matlet.2006.08.010

134. Pu, H., Jiang, F., Wang, Y., & Yan, B. (2010). Soft magnetic composite particles of reduced iron coated with poly(p-xylylene) via chemical vapor deposition polymerization. *Colloids and Surfaces A: Physicochemical and Engineering Aspects*, *361*(1–3), 62–65. doi:10.1016/j.colsurfa.2010.03.012

135. You, J. L., Park, B. J., Choi, H. J., Choi, S. B., & Jhon, M. S. (2007). Preparation and magnetorheological characterization of CI/PVB core/shell particle suspended MR fluids. *International Journal of Modern Physics B*, *21*(28n29), 4996–5002. doi:10.1142/S0217979207045943

136. Hu, B., Fuchs, A., Huseyin, S., Gordaninejad, F., & Evrensel, C. (2006). Supramolecular magnetorheological polymer gels. *Journal of Applied Polymer Science*, *100*(3), 2464–2479. doi:10.1002/app.23578

137. Rowe-Konopacki, M. D., & Boyes, S. G. (2007). Synthesis of Surface Initiated Diblock Copolymer Brushes from Flat Silicon Substrates Utilizing the RAFT Polymerization Technique. *Macromolecules*, *40*(4), 879–888. doi:10.1021/ma0623340

138. Odian, G. G. (2004). *Principles of polymerization*. Hoboken, N.J.: Wiley. Retrieved from http://public.eblib.com/EBLPublic/PublicView.do?ptiID=469767

139. Huang, Y., Liu, Q., Zhou, X., Perrier, S., & Zhao, Y. (2009). Synthesis of Silica Particles Grafted with Well-Defined Living Polymeric Chains by Combination of RAFT Polymerization and Coupling Reaction. *Macromolecules*, *42*(15), 5509–5517. doi:10.1021/ma900604v

140. Moad, G., Rizzardo, E., & Thang, S. H. (2006). Living Radical Polymerization by the RAFT Process—A First Update. *Australian Journal of Chemistry*, *59*(10), 669–692. Retrieved from http://dx.doi.org/10.1071/CH06250

141. Zhu, J., Zhu, X., Kang, E. T., & Neoh, K. G. (2007). Design and synthesis of star polymers with hetero-arms by the combination of controlled radical polymerizations and click chemistry. *Polymer*, *48*(24), 6992–6999. doi:10.1016/j.polymer.2007.10.004

142. Hua, D., Tang, J., Cheng, J., Deng, W., & Zhu, X. (2008). A novel method of controlled grafting modification of chitosan via RAFT polymerization using chitosan-RAFT agent. *Carbohydrate Polymers*, *73*(1), 98–104. doi:10.1016/j.carbpol.2007.11.008

143. http://www.sigmaaldrich.com/catalog/product/aldrich/371998?lang=en&region=US. (n.d.).

144. Ranjan, R., & Brittain, W. J. (2007). Combination of Living Radical Polymerization and Click Chemistry for Surface Modification. *Macromolecules*, *40*(17), 6217–6223. doi:10.1021/ma0705873

145. Stenzel, M. H., & Davis, T. P. (2002). Star polymer synthesis using trithiocarbonate functional β-cyclodextrin cores (reversible addition–fragmentation chain-transfer polymerization). *Journal of Polymer Science Part A: Polymer Chemistry*, *40*(24), 4498–4512. doi:10.1002/pola.10532

146. Sutrisno, J. (2011). *Surface polymerization of inorganic materials for renewable energy, intelligent materials, and bio-materials applications*. UNIVERSITY OF NEVADA, RENO. Retrieved from http://gradworks.umi.com/34/57/3457590.html

147. D11 Committee. (2012). *Test Methods for Rubber Properties in Compression or Shear (Mechanical Oscillograph)*. ASTM International. Retrieved from http://www.astm.org/Standards/D945.htm

148. Li, Y., & Li, J. (2013). Development and modeling of a highly adjustable base isolator utilizing magnetorheological elastomer. In *ASME 2013 Conference on Smart Materials, Adaptive Structures and Intelligent Systems, SMASIS 2013*. Presented at the ASME 2013 Conference on Smart Materials, Adaptive Structures and Intelligent Systems, SMASIS 2013, ASME.

149. Wen, Y.-K. (1976). Method for Random Vibration of Hysteretic Systems. *Journal of the Engineering Mechanics Division*, *102*(2), 249–263. Retrieved from http://cedb.asce.org/cgi/WWWdisplay.cgi?6630

150. Li, W., Zhang, X., & Du, H. (2012). Development and simulation evaluation of a magnetorheological elastomer isolator for seat vibration control. *Journal of Intelligent Material Systems and Structures*, *23*(9), 1041–1048. doi:10.1177/1045389X11435431

151. Alberdi-Muniain, A., Gil-Negrete, N., & Kari, L. (2013). Modelling energy flow through magneto-sensitive vibration isolators. *International Journal of Engineering Science*, *65*, 22–39. doi:10.1016/j.ijengsci.2013.02.003

152. Rodríguez, A., Pozo, F., Bahar, A., Acho, L., Vidal, Y., & Rodellar, J. (2012). Force-derivative feedback semi-active control of base-isolated buildings using large-scale MR fluid dampers. *Structural Control and Health Monitoring*, *19*(1), 120–145. doi:10.1002/stc.430

153. Wang, Y., & Dyke, S. (2013). Modal-based LQG for smart base isolation system design in seismic response control. *Structural Control and Health Monitoring*, *20*(5), 753–768. doi:10.1002/stc.1490

154. Yi, F., Dyke, S., Caicedo, J., & Carlson, J. (2001). Experimental Verification of Multiinput Seismic Control Strategies for Smart Dampers. *Journal of Engineering Mechanics*, *127*(11), 1152–1164. doi:10.1061/(ASCE)0733-9399(2001)127:11(1152)

155. Cha, Y.-J., & Agrawal, A. K. (2013). Velocity based semi-active turbo-Lyapunov control algorithms for seismically excited nonlinear smart structures. *Structural Control and Health Monitoring*, *20*(6), 1043–1056. doi:10.1002/stc.1517

156. Behrooz, M., Wang, X., & Gordaninejad, F. (2013). Modeling of a new semi-active/passive magnetorheological elastomer isolator. *Smart Materials and Structures*, *under review*.

157. Mills, R. S., Krawinkler, H., & Gere, J. M. (1979). *Model tests on earthquake simulators development and implementation of experimental procedures* (No. 39). John A. Blume Earthquake Engineering Center, Stanford University.

158. Cha, Y.-J., Agrawal, A. K., & Dyke, S. J. (2013). Time delay effects on large-scale MR damper based semi-active control strategies. *Smart Materials and Structures*, *22*(1), 015011. doi:10.1088/0964-1726/22/1/015011

159. Zhou, Y., & Amirouche, F. (2009). Study of fluid damping effects on resonant frequency of an electromagnetically actuated valveless micropump. *The International Journal of Advanced Manufacturing Technology*, *45*(11-12), 1187–1196. doi:10.1007/s00170-009-2053-4

Appendix A. Fabrication of Magnetorheological Elastomers

Figure A.1 (a) illustrates the electromagnetic system used for curing MREs to obtain directional properties i.e. enhanced stiffness change, and Figure A.1 b illustrates the mold used to produce conical MREs. A typical cured MRE is shown in Figure A.2. Figure A.3 demonstrates the picture of the mold used to make the passive rubber parts of the VSDA.

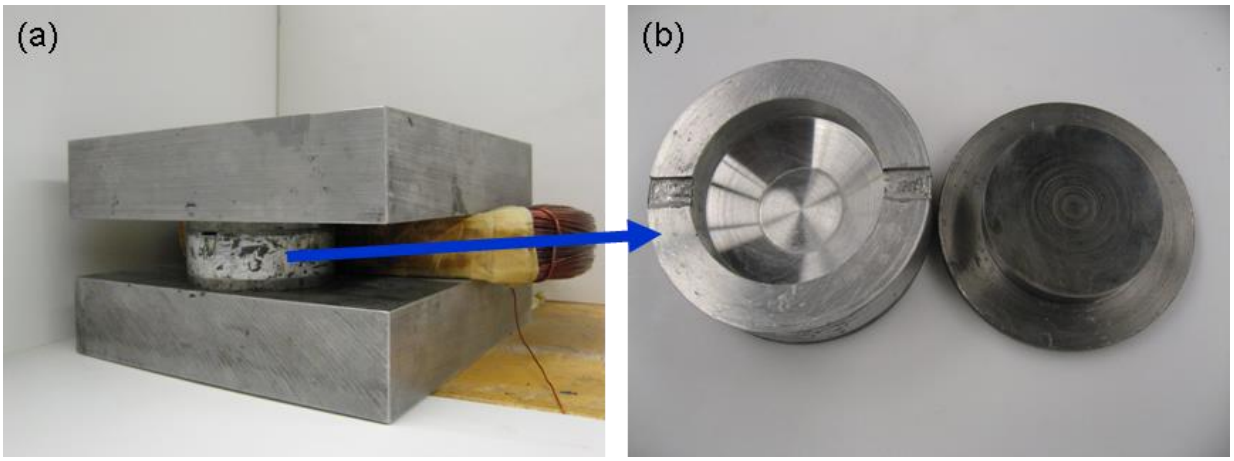

Figure A.1. Photo of: (a) Electromagnetic device, and (b) MREs mold.

Figure A.2. Silicone–RTV MRE with 70% wt. iron.

Figure A.3. The fabricated rubber support and mold.

The formation of chainlike structures of magnetic particles within MREs is important to their performance. The chains were formed by placing the pre-cured silicone–RTV MREs mixture in a magnetic field during the curing process. The chains were locked in place during chemical cross-linking of the elastomer. The chain distribution of iron particles within MREs was confirmed using optical or electron microscopy. The strength of the chainlike structure depends on the strength of the electromagnetic field. The cross-section of silicone–RTV MRE images from an optical microscope are shown in Figure A.4. The chainlike structure can be seen in the Figure A.4 a and aligned particles are shown in Figure A.4 b.

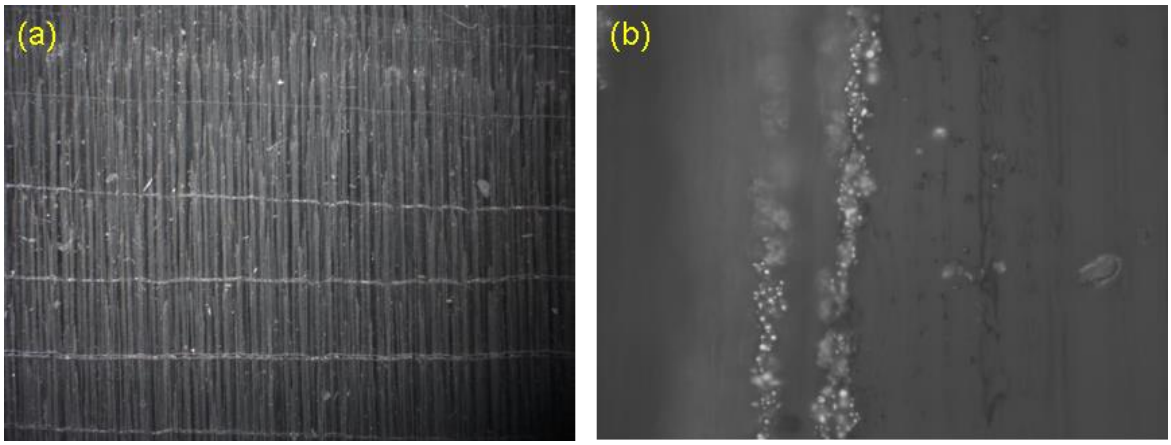

Figure A.4. The optical images of aligned iron particles in silicone–RTV MREs: (a) 2x, and (b) 20x in magnification.

Appendix B. Effect of Frequency on the Performance of the VSDAs

Increasing loading frequency also affects the amount of load exerted by the VSDAs, as expected for viscoelastic materials. From Figure B.1, the maximum force in off-state increased about 55% when the loading frequency was increased from 0.1 to 10 Hz and stayed almost constant for more than 10 Hz.

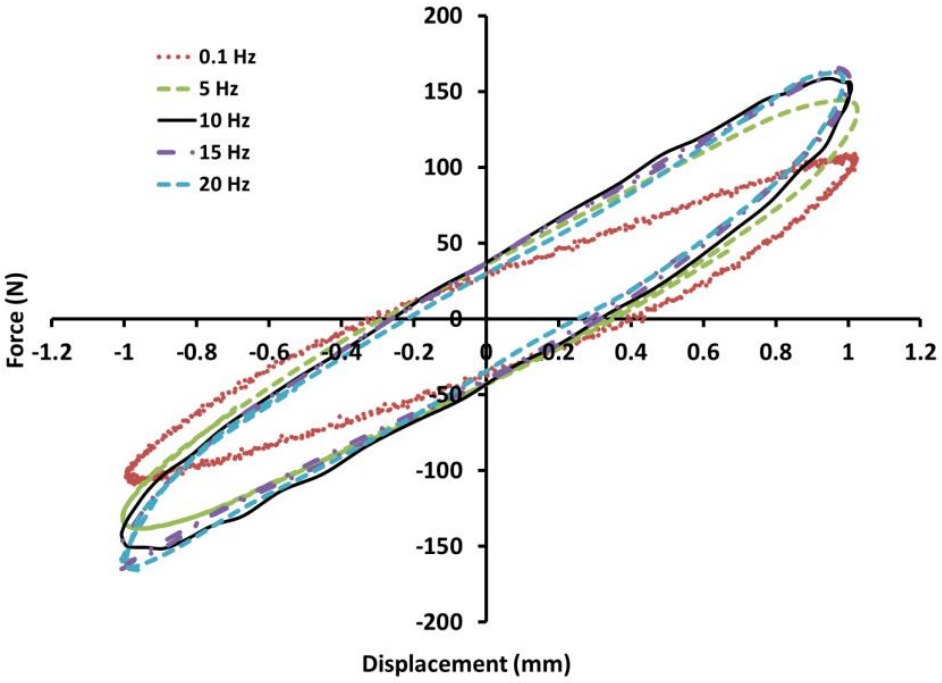

Figure B.1. Off-state frequency dependent behavior of VSDAs at 5% strain.

As shown in Figure B.2, the frequency effect is more pronounced for on-state since the maximum load continued increasing up to 60% when the loading frequency was increased from 0.1 to 20 Hz. The effect of the frequency is not directly modeled in this work, but it is considered in transmissibility experimental and theoretical study of an integrated system of VSDAs. The model was tuned for dynamic testing by slightly increasing parameters of the

model to fit the experimental data. The integrated system modeling demonstrated the performance of the VSDAs and the model when VSDAs are supporting a heavy load.

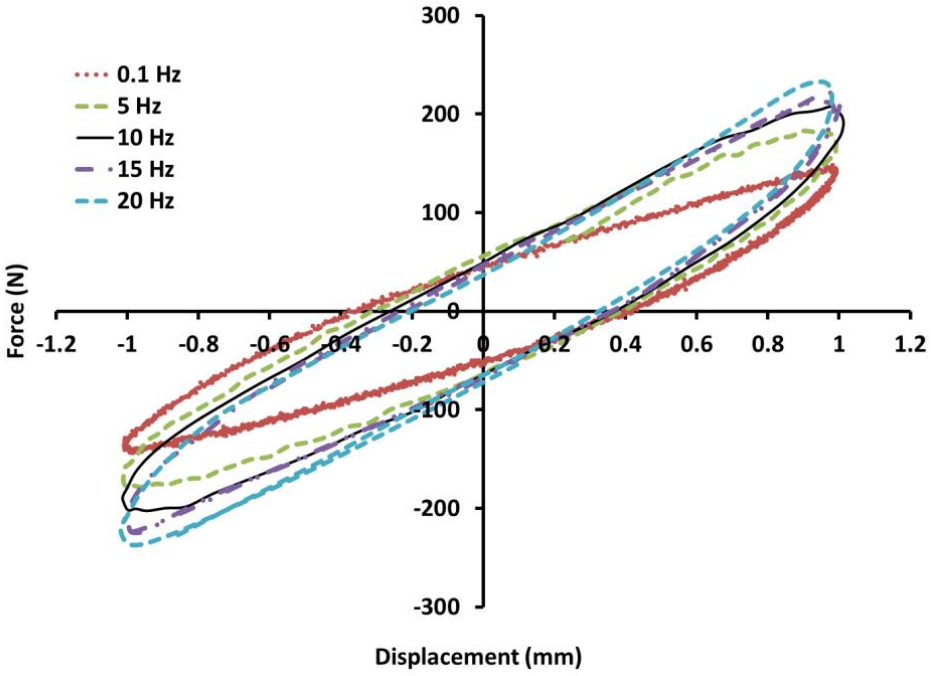

Figure B.2. On-state frequency dependent behavior of VSDAs at 5% strain.

Appendix C. Data Acquisition System

National Instrument PCI-1000 chassis along with SCXI-1120 modules were used to record the acceleration data. Simulink data acquisition tool box was used to record the data. Hardware filtering has been performed using the jumper settings of the PCI-1120 module. Data were also filtered and centered using bandpass filter and amplified using the signal processing toolbox of the SIMULINK.

Figure C.1 depicts the complete block diagram of the entire system with feedback control loops. PCI-MIO-16E-1 data acquisition card along with PCB-68 breakout board was used to read the accelerometers' signals in the computer. Four piezoelectric DC accelerometers, model number 4575 from Brüel & Kjær with a maximum range of ± 2 g and an accuracy of 1000 mV/g were used. One accelerometer was used as an input and rest of the accelerometers were used on the floors. The signals from accelerometers were converted to displacement and velocity via integration and were used in the control law. The control signal was sent to a current controller through the output channels of the same data acquisition system. The current controller is composed of a current mode controller PWM chip which can generate a PWM signal. The PWM signal was inputted to a power MOSFET to open and close the main power circuit. The control and PWM signals were checked with an oscilloscope to ensure the accuracy and the shape of the generated control signal in the data acquisition system vs. the signal observed. The power for four VSDAs was supplied with two controllable Genesis 150-10 power supplies.

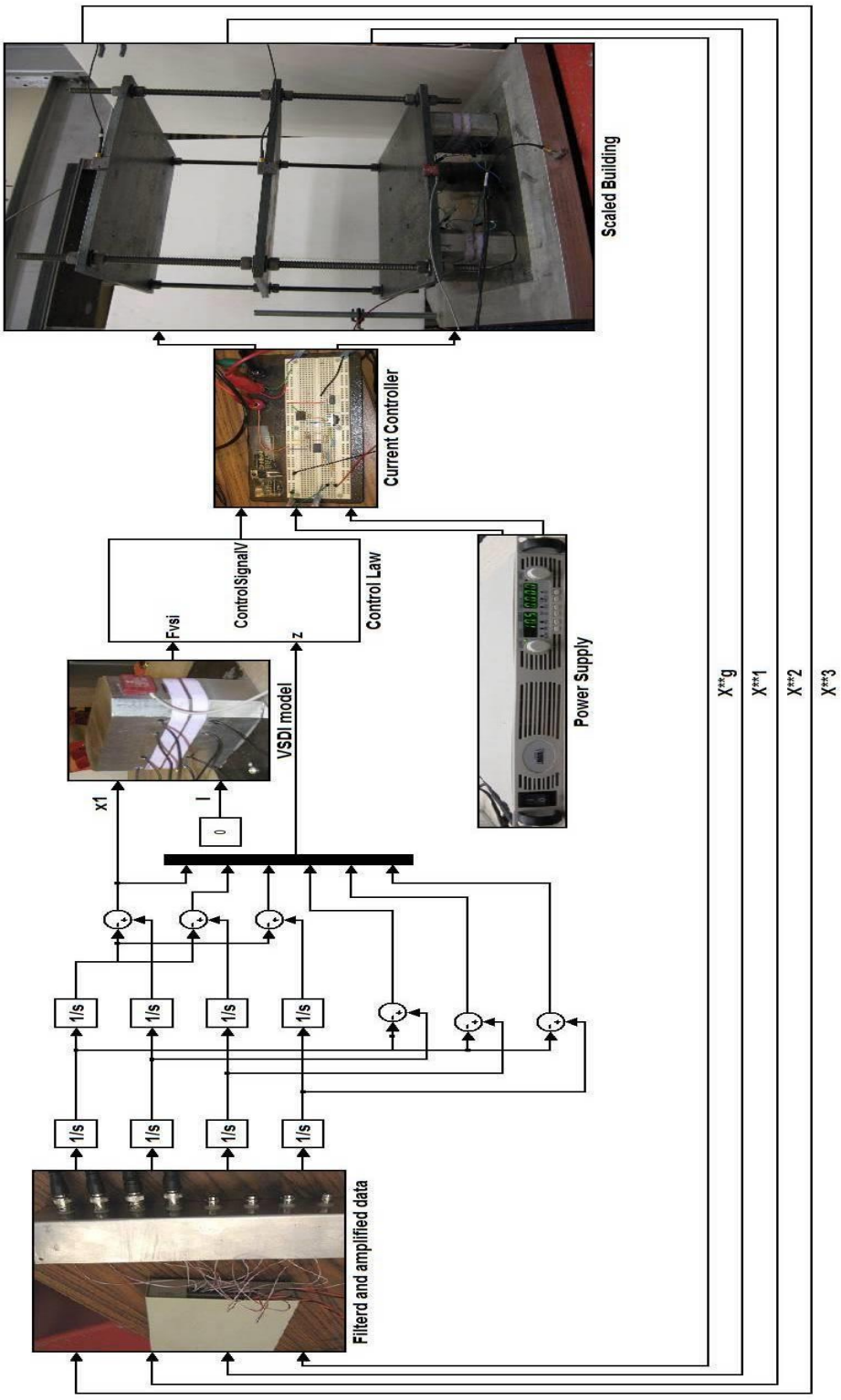

Figure C.1. Block diagram of the control of a two-story building with four VSDAs

Appendix D. Dynamic Performance of a Single VSDA

To utilize VSDA in a system for vibration control, its mechanical properties should be identified. Constant acceleration vibration experiments with sweeping frequency technique were used to measure the performance of each device and as well as the integrated system. By measuring the frequency response of the device, the transmissibility function versus sweeping frequency, and different control input electric currents are obtained.

The performance of the VSDA was examined by a 2 Kip shaking table Ling Dynamic System (LDS) under shear test. Figure D.1 shows a picture of the experimental setup. The transmissibility function and the phase angle plot were obtained by the LaserUSB data acquisition system. The transmissibility function is the ratio of magnitude of output acceleration to the input acceleration and the phase angle is the phase difference of input and output accelerations as a function of frequency. Two accelerometers were calibrated and installed, one on the shake table and another on the top cap of the VSDA. A DC power supply was used to supply the input power to the accelerometers and a TDK Lambda power supply was used to supply input power to the VSDAs.

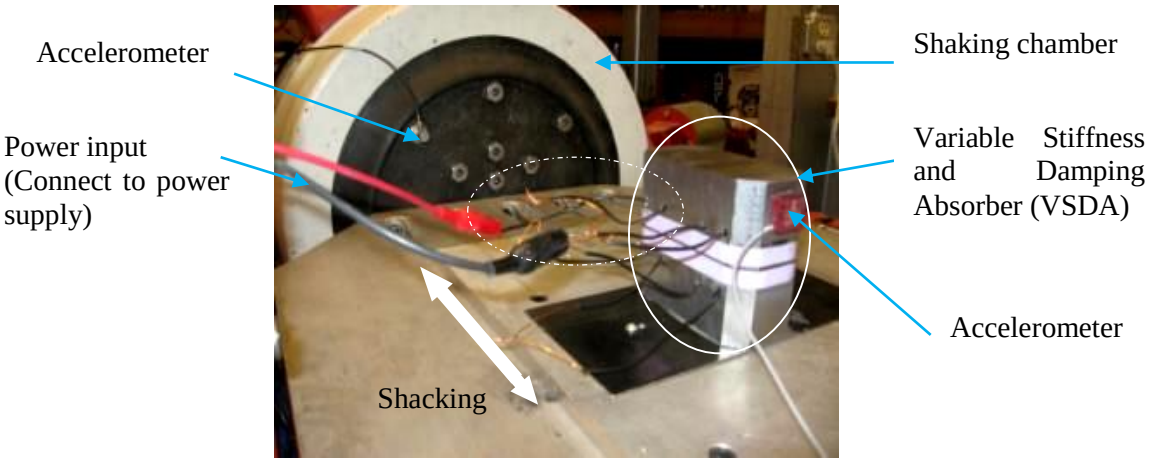

Figure D.1. Photo of the experimental setup.

The stiffness and damping of the VSDA can be obtained by considering the device as a single-degree-of-freedom (SDOF) system supporting the top part as a mass. The damped natural frequency and damping ratio was obtained from the measured transmissibility functions. The transmissibility function is generated using the following equation:

$$T_a = T_d = \frac{\sqrt{(2r\xi)^2+1}}{\sqrt{(2r\xi)^2+(1-r^2)^2}} \tag{B.1}$$

where $r = \frac{\omega}{\omega_n}$ and percentage of damping is calculated from quality factor, Q which is defined as:

$$Q = \frac{f_c}{f_2 - f_1} \tag{B.2}$$

where f_p is the peak frequency, f_1 and f_2 are the frequencies where half power is transmitted and computed at 3 dB below f_p. With the quality factor, one can calculate the damping coefficient percentage, ζ as follows:

$$\zeta = \frac{1}{2Q} \tag{B.3}$$

Therefore, the stiffness $K(I)$ as well as the damping coefficient $C(I)$ of the VSDA as a function of applied currents *I* can be obtained by Equations (B.4) and (B.5), where, *m* is the mass of the top cap, ζ is the damping ratio and f_{peak} is the resonant frequency. Equations (B.6) and (B.7) are used to determine the percentage changes in the stiffness and damping coefficient of VSDA, respectively; where $K(I)$ and $C(I)$ are the stiffness and damping coefficient in the activated state, whereas K_{off} and C_{off} are the stiffness and damping coefficient in the off-state.

$$K(I) = \frac{m(2\pi f_{peak})^2}{(1-2\xi^2)} \tag{B.4}$$

$$C(I) = 2\xi\sqrt{mK(I)} \tag{B.5}$$

$$\Delta\text{K}\% = \frac{K(I)-K_{off}}{K_{off}} \times 100 \tag{B.6}$$

$$\Delta\text{C}\% = \frac{C(I)-C_{off}}{C_{off}} \times 100 \tag{B.7}$$

Results of similar experiments are summarized in the following tables for different acceleration inputs. The peak transmissibility (T_{peak}) and corresponding peak frequency (f_{peak})

for different applied currents are listed in Table D.1, 0 and Table D.3 for three input accelerations of 0.2 g, 0.3 g and 0.4 g, respectively. The stiffness (*K*) and damping coefficient (*C*) as a function of applied electric current, as well as, their percentage changes compared to the off-state (no applied magnetic field) are also listed in these tables. Higher damping and higher stiffness changes under applied electric currents were obtained for acceleration input of 0.2 g. In all three cases, significant changes in stiffness and damping coefficients of the VSDA were observed. As can be seen, the proposed VSDA is capable of altering its stiffness and damping properties simultaneously up to 30% and 40%, respectively, with an applied electric current of 5 Amp.

Table D.1. Characterization Properties of VSDA for 0.2 g Acceleration Input.

Input Current (Amp)	f_{peak} (Hz)	T_{peak}	K (KN/m)	ΔK %	ζ%	C (KN.s/m)	ΔC %
0	30.31	6.05	74.49		6.37	1.56	
1	31.08	5.77	78.45	5.31	6.87	1.73	10.67
2	32.05	5.70	83.61	12.24	7.69	2.00	27.89
3	32.93	5.82	88.28	18.52	7.81	2.09	33.47
4	33.77	5.84	92.84	24.64	7.78	2.13	36.35
5	34.07	5.81	94.59	26.98	7.96	2.20	40.81

Table D.2. Characterization Properties of VSDA for 0.3 g Acceleration Input.

Input Current (Amp)	f_{peak} (Hz)	T_{peak}	K (KN/m)	ΔK %	ζ%	C (KN.s/m)	ΔC %
0	28.2	6.16	64.57		6.88	1.57	
1	28.87	5.81	67.72	4.87	7.15	1.67	6.42
2	29.98	5.72	73.15	13.28	7.62	1.86	17.88
3	31.14	5.83	78.89	22.17	7.58	1.92	21.77
4	31.82	5.82	82.42	27.64	7.75	2	27.26
5	32.17	5.79	84.25	30.46	7.83	2.05	29.99

Table D.3. Characterization Properties of VSDA for 0.4 g Acceleration Input.

Input Current (Amp)	f_{peak} (Hz)	T_{peak}	K (KN/m)	ΔK %	ζ%	C (KN.s/m)	ΔC %
0	27.45	6.23	61.09		6.38	1.42	
1	27.95	5.92	63.43	3.82	6.92	1.57	10.51
2	28.87	5.69	67.81	10.99	7.58	1.78	25.16
3	29.61	5.63	71.44	16.94	8.13	1.96	37.8
4	30.58	5.85	76.14	24.62	7.74	1.92	35.43
5	30.91	5.86	77.8	27.34	7.72	1.94	36.54

The next set of testing were performed while the temperature was kept constant. Every test were performed starting at room temperature to minimize the temperature effect. Characterization tests were carried out using constant input acceleration of 0.05, 0.1 and 0.2 g (1 g = 9.80 m/s) with a range of sweeping frequencies from 5 to 60Hz in sinusoidal motions.

In each test, the input electric current is kept at 0.0, 1.0, 2.0 and 3.0 Amps. The results of vibration experiments, presented in Table D.4., Figure D.2. and Figure D.3., show the transmissibility and phase angle difference for 0.1 g acceleration inputs.

Table D.4. Single VSDA Damping and Stiffness with 80%wt. Aligned MRE and for Different Input Electric Currents and Different Acceleration Inputs

	0.05 g		0.1 g		0.2 g	
Input Current (Amp)	K (KN/m)	C (N.s/m)	K (KN/m)	C (N.s/m)	K (KN/m)	C (N.s/m)
0	75.36	52.89	148.49	81.94	141.06	74.29
1	86.26	57.76	164.77	80.99	152.98	95.12
2	96.20	63.39	185.89	88.61	172.92	89.02
3	100.98	60.77	209.26	86.58	177.08	91.41

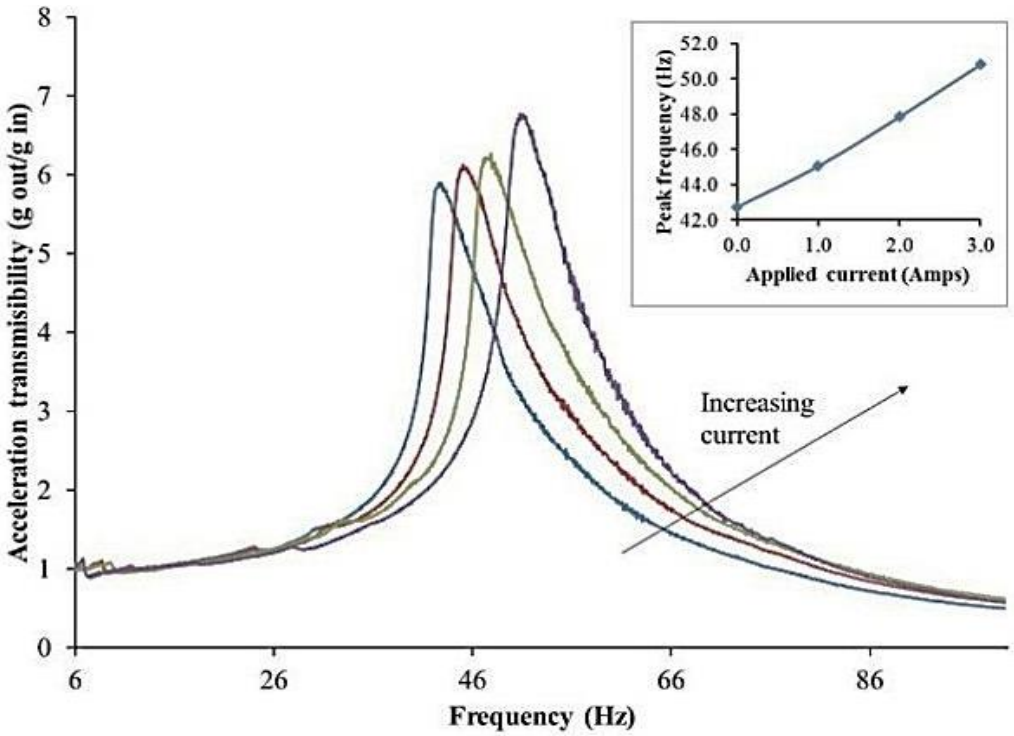

Figure D.2. Transmissibility of 0.1g sinusoidal constant amplitude acceleration input for different input electric currents ranging from 0 to 3 Amps. The insert in Figure 2(a) represents peak Dynamic performance of the VSDA in an Integrated System.

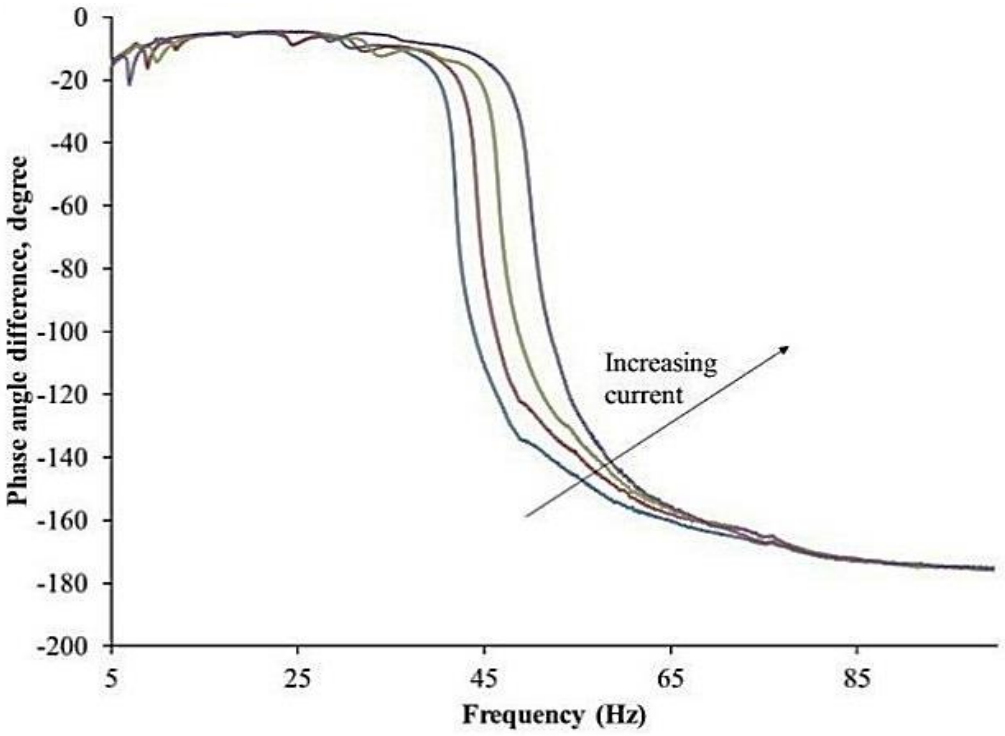

Figure D.3. Phase angle difference for 0.1 g sinusoidal constant amplitude acceleration input for different input electric currents ranging from 0 to 3 Amps.

Effect of iron particle alignment: During the curing process of the MRE, the iron particles align with the applied magnetic field. Aligning particles changes mechanical and electrical properties of MREs. To observe this effect 80% wt. MREs with aligned and homogenous configurations were fabricated. Silicon oil added to the MRE mixture to lower the stiffness and permit higher iron particle percentage. Figure D.4 demonstrates the typical transmissibility of the VSDA's upper cap response to the base motion with peak 0.2 g acceleration in sinusoidal excitations for 80% wt. Non-aligned MRE. It is clear that increasing the input electric current makes the VSDA stiffer and shifts the resonant (or peak) frequency to the right. One can also observe that the peak amplitude of the transmissibility decreases in

response to the applied input electric current as a result of damping increase. Figure D.5 shows the corresponding phase angle difference between input and output accelerations. Increasing the applied current also significantly shifts the phase angle, especially, at about the resonant frequency.

Similar results are presented in Figure D.6 and Figure D.7 for the change in stiffness and damping properties of the VSDA implementing 80% wt. aligned MRE subjected to various applied electric currents. Larger shift in natural frequency was observed when compared to the non-aligned MRE. This demonstrates that the MRE with an aligned particle structure has better performance in controlling stiffness and damping properties than the MRE without particle alignment.

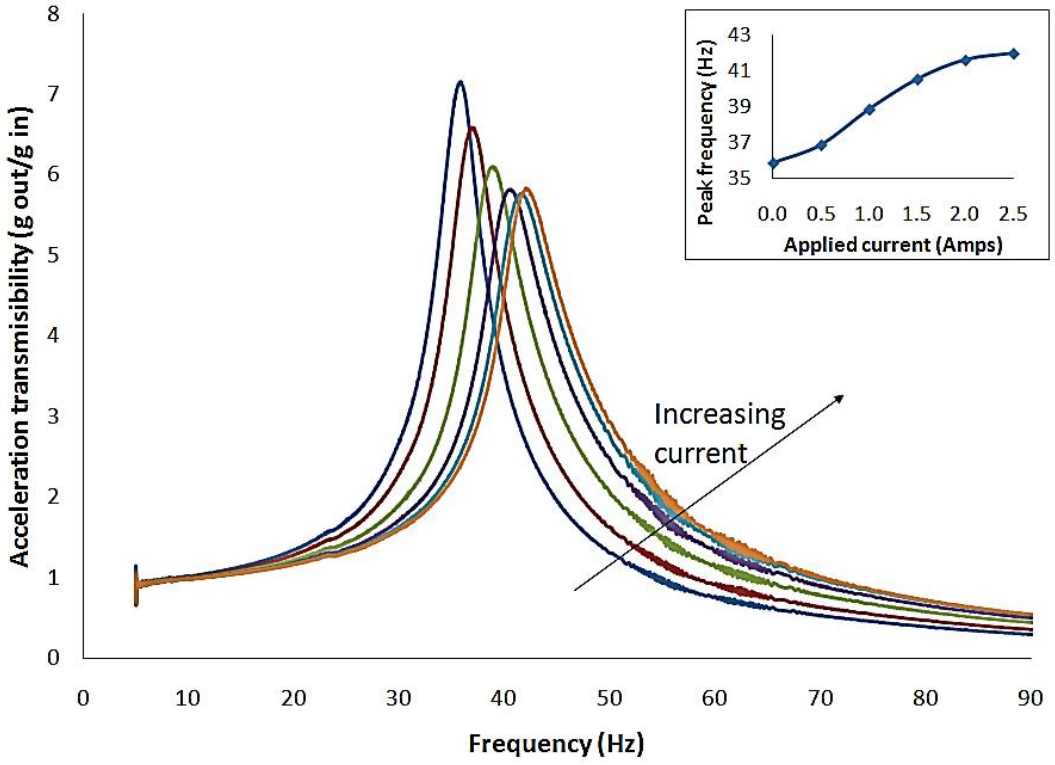

Figure D.4. Transmissibility of 0.2g sinusoidal constant amplitude acceleration input for different input electric currents ranging from 0 to 2.5 Amps, Insert in Figure: Peak frequency vs. change in input electric current for 80%wt. non-aligned MRE.

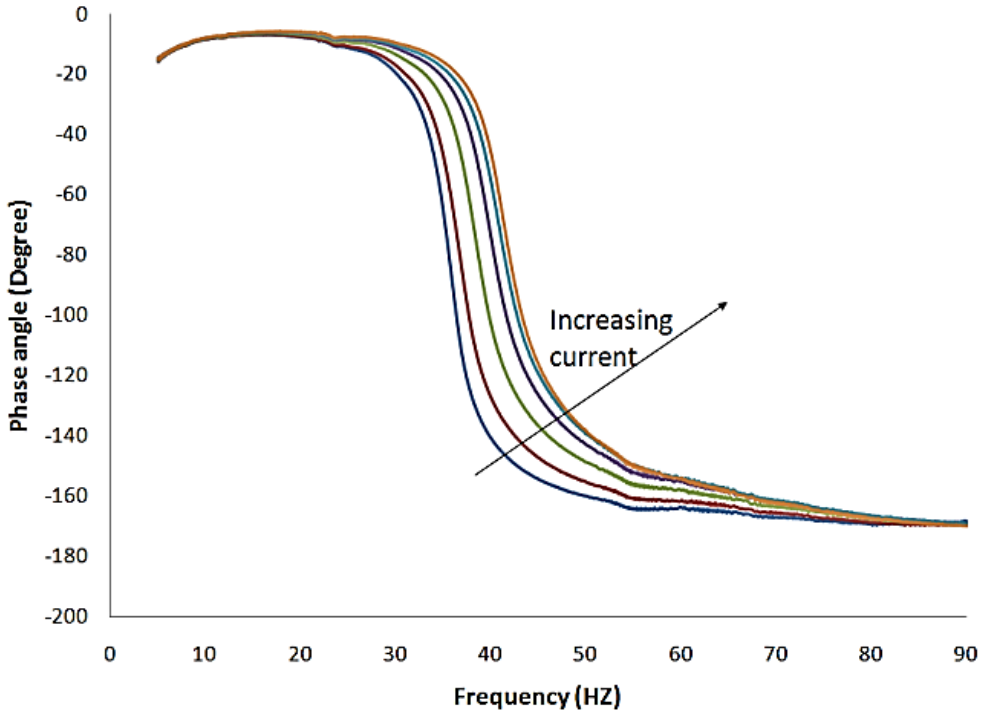

Figure D.5. Phase angle of 0.2g sinusoidal constant amplitude acceleration input for different input electric currents ranging from 0 to 2.5 Amps for 80%wt. non-aligned MRE.

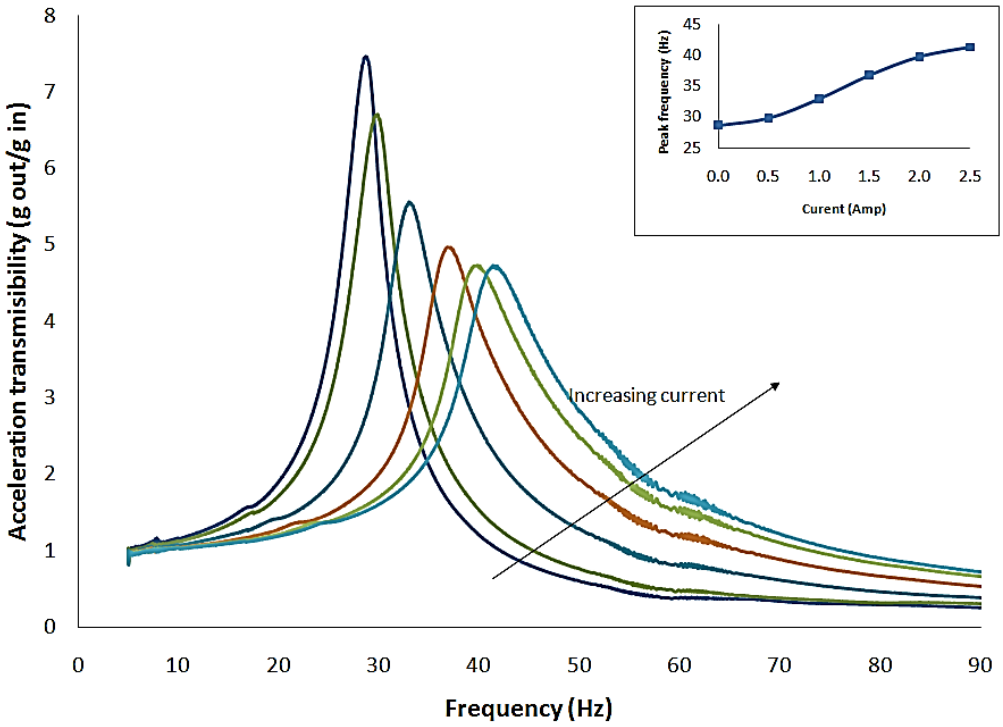

Figure D.6. Transmissibility of 0.2g sinusoidal constant amplitude acceleration input for different input electric currents ranging from 0 to 2.5 Amps, Insert in Figure: Peak frequency vs. change in input electric current for 80%wt. aligned MRE.

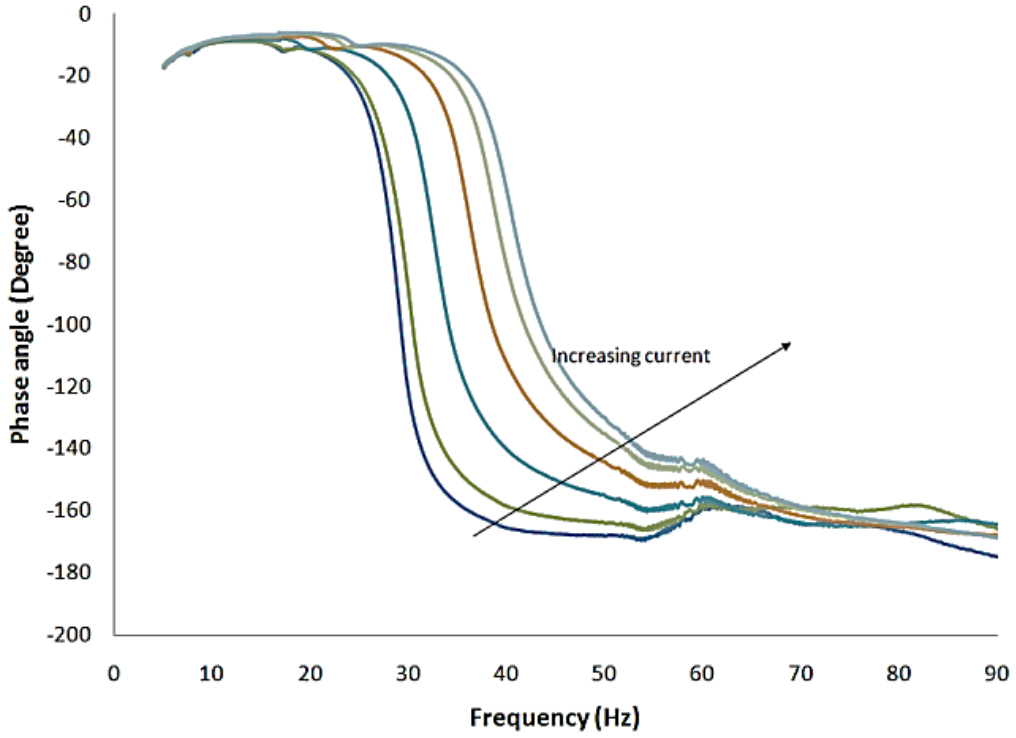

Figure D.7. Phase angle of 0.2g sinusoidal constant amplitude acceleration input for different input electric currents ranging from 0 to 2.5 Amps for 80%wt. aligned MRE.

The change in the stiffness and damping of the VSDA with both non-aligned and aligned MREs are shown in Figure D.8 and Figure D.9 for different applied currents. In both cases, significant changes in stiffness and damping of the VSDA are observed; however much higher changes are observed with the implementation of aligned MREs. As shown, the proposed VSDA is capable of altering its stiffness and damping properties simultaneously up to 110% and 150% with aligned MRE, respectively, with an applied electric current of 2.5 Amps.

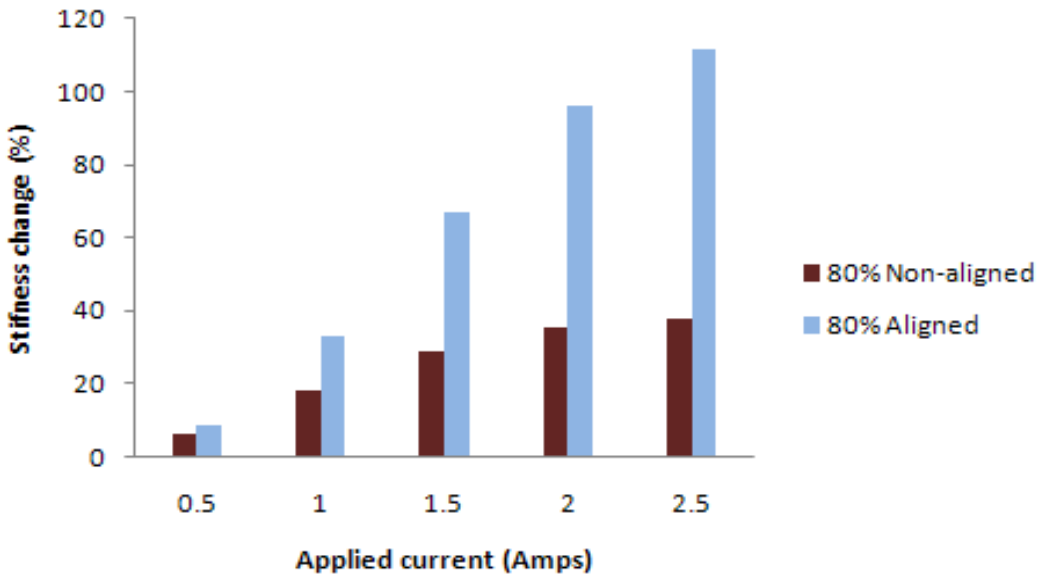

Figure D.8. Stiffness change of VSDA for 80%wt. aligned MRE compared to 80% wt. non-aligned MRE.

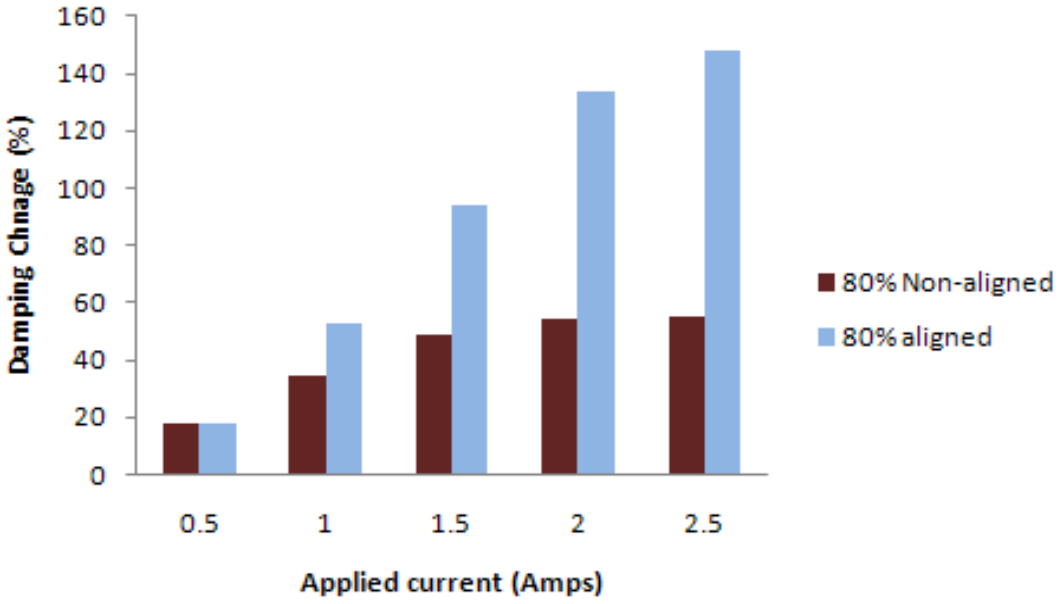

Figure D.9. Damping change of VSDA for 80%wt. aligned MRE compared to 80% wt. non-aligned MRE.

Experimental results prove that the VSDA with aligned MRE achieves much better performance in stiffness and damping changes than the one with non-aligned MRE. The VSDA with aligned MRE and 80%wt. iron particle concentration is capable of increasing its stiffness and damping properties significantly beyond that of homogenous MREs.

Effect of temperature on VSDA performance: Because each VSDA embeds fours electromagnetic coils, it produces heat and increases the temperature in MREs. Increasing heat in MREs will affect its mechanical properties such as the damping ratio. The temperature was monitored by a separate National instrument USB thermocouple. Figure D.10 shows how the temperature on the surface of MRE increases for 80 ^{o}C in twenty minutes only if the applied current is kept constant at 4 amps. Figure D.10 also depicts how MREs cool down once the electric current is removed. The temperature effect was much less in control and seismic tests because duration of seismic experiments was around 1 minute and also the devices were turned on and off continuously with the controller.

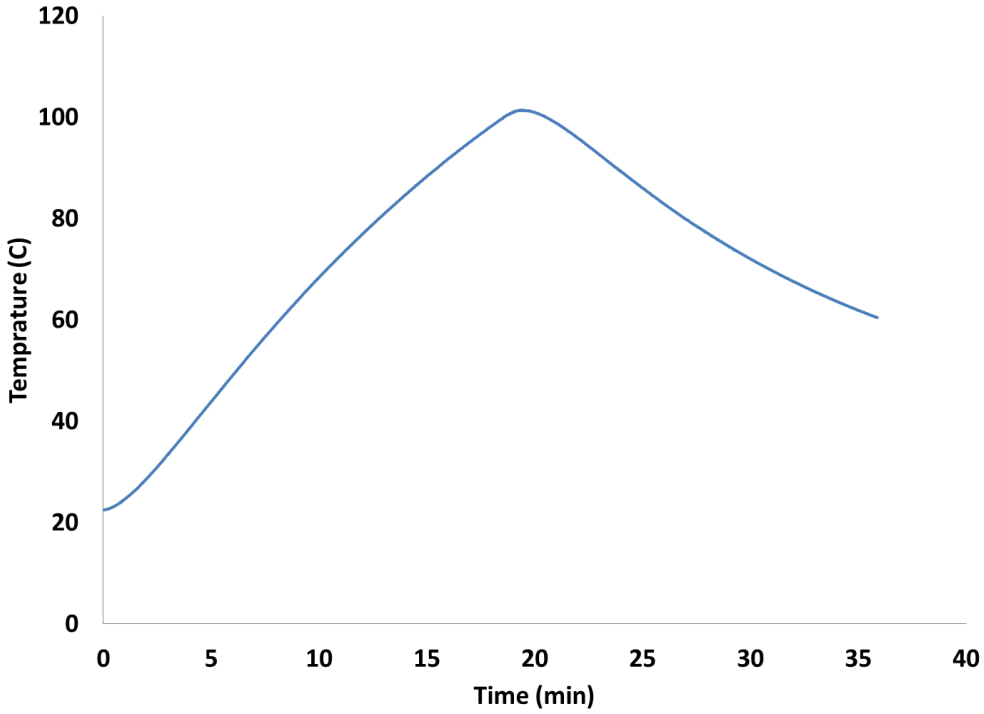

Figure D.10. Temperature increase in MREs with 4 Amps electric current input.

Figure D.11 shows the increase in stiffness with applied electric current for the VSDAs when tests are done continuously and temperature builds up in the VSDAs. It is shown that by applying higher currents natural frequency shifts to the right, which means stiffness is increased, but peak transmissibility decreases from 7.2 to 5.7 which means the damping of the MRE/rubber materials has increased due to increased temperature.

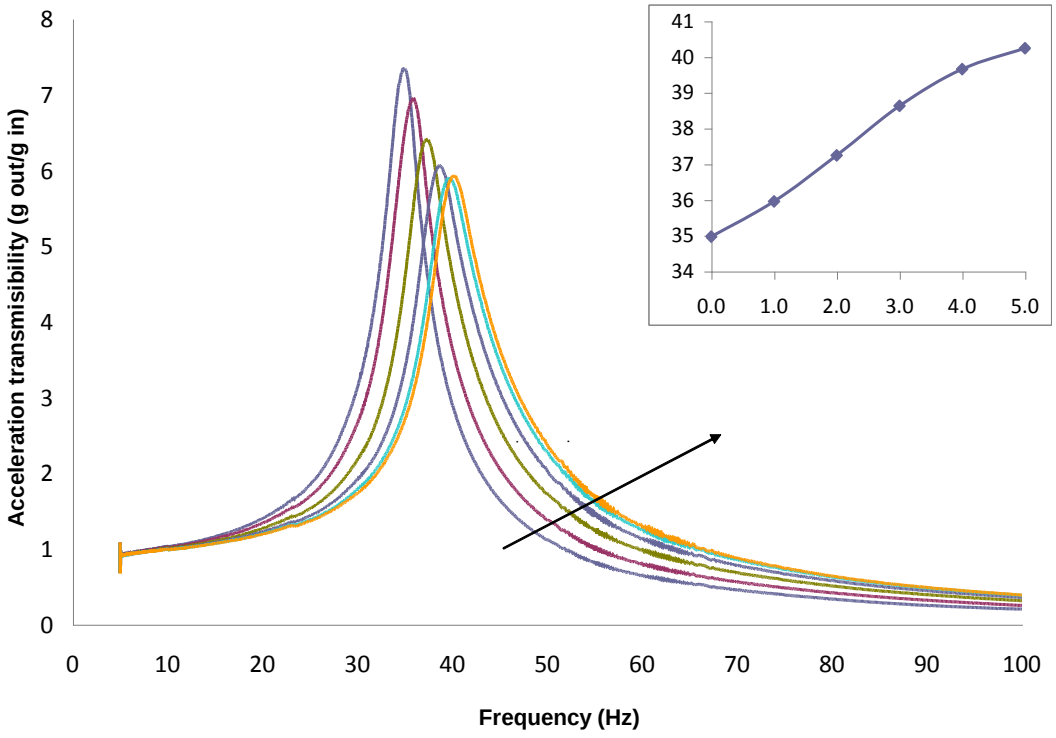

Figure D.11. Transmissibility of 0.3g sinusoidal constant amplitude acceleration input for different input electric currents ranging from 0 to 5 Amps for MRE and Rubber material system 2, Insert to Figure 11(b): Peak frequency vs. input electric current.

Appendix E. Design and Characterization of the Scaled Building

The 1:16 scale was selected based on the maximum size of the scaled building the shake table can handle. The scaling factors are shown in Table E.1. Scaled parameters can be calculated by dividing the actual parameter over the scaling factor e.g. $L_{scaled} = L/S$. The ground motion is scaled by keeping the acceleration constant and scaling the time by dividing it over $\sqrt{S}$.

Table E.1. Scaling factors used for the scaled building.

Scaled parameter	Scaling factor
Time	$\sqrt{S}$
Frequency	$1/\sqrt{S}$
Length	S
Weight	S^2
Acceleration	1

The scaled building consists of two stories that are 9 inches in height and a base floor that houses the four absorbers underneath. Each floor for each story is one solid platform with the dimension of 18"×18". The platforms are secured together by four rods that are fastened by nuts and washers - one at each corner of the platforms. Mass was added and adjusted on each story during testing by putting steel layers with dimension of 8"×8" each. The mass of the whole building including all nuts, washers and bolts was 78.63 kg without additional mass and was 228.06 kg with full additional mass. The setup was secured on the slip table of the shaking system using adhesives and bolts. Tests were performed in off and on states with the shake table

applying a horizontal sinusoidal vibration with a constant 0.05 g amplitude vibration applied to the base floor. A DAQ received the input signal from the absorber and produced output to process and generate the final transmissibility curves. Shaker controller software was used to control the shaker and obtain results. To better understand the test setup instrumentation, the schematic of the vibration experiments is illustrated in Figure E.1. As shown, all transmissibility signals were received in DAQ system and stored in computer. Three accelerometers were calibrated and attached to the scaled building floors to obtain the transmissibility of each floor. Additional mass in form of 0.25"×12"×12" blocks were added to the scaled building floors to observe the effect of additional mass on performance of the VSDAs.

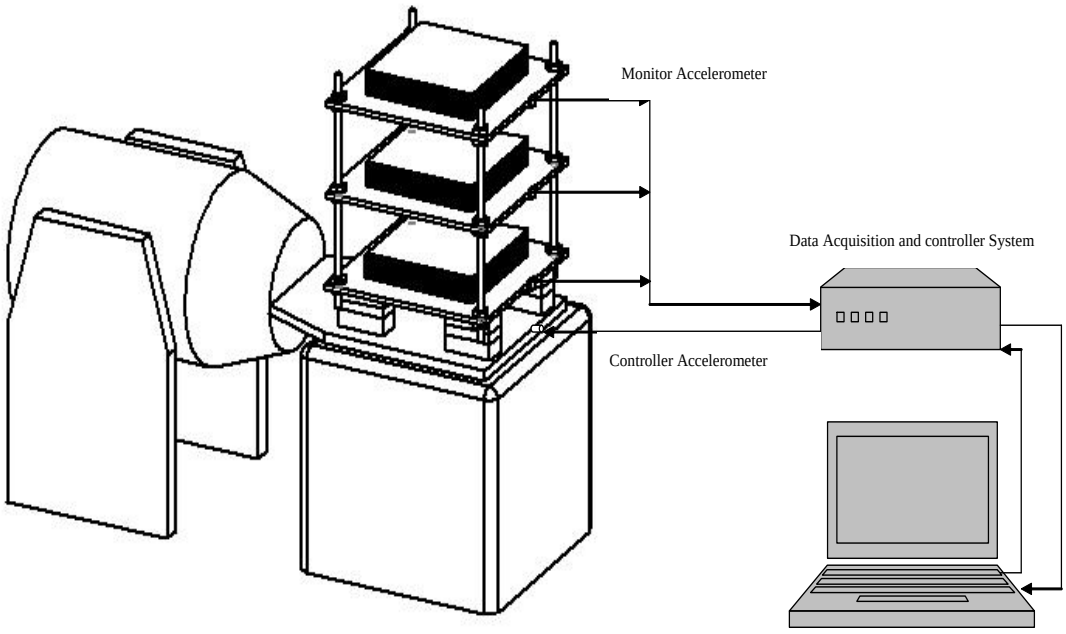

Figure E.1. The schematic of the instrumentation of the scaled building test setup.

Stiffness of each absorber which was obtained from characterization tests, was used to achieve the target period of around 0.1 seconds for the isolated scaled building. Then the SolidWorks FE analyses were conducted to find the period of the scaled building to verify the design procedure and results. Figure E.2 demonstrates the first mode of vibration for the scaled building without additional mass and Figure E.3 presents the same results for the scaled building with additional mass.

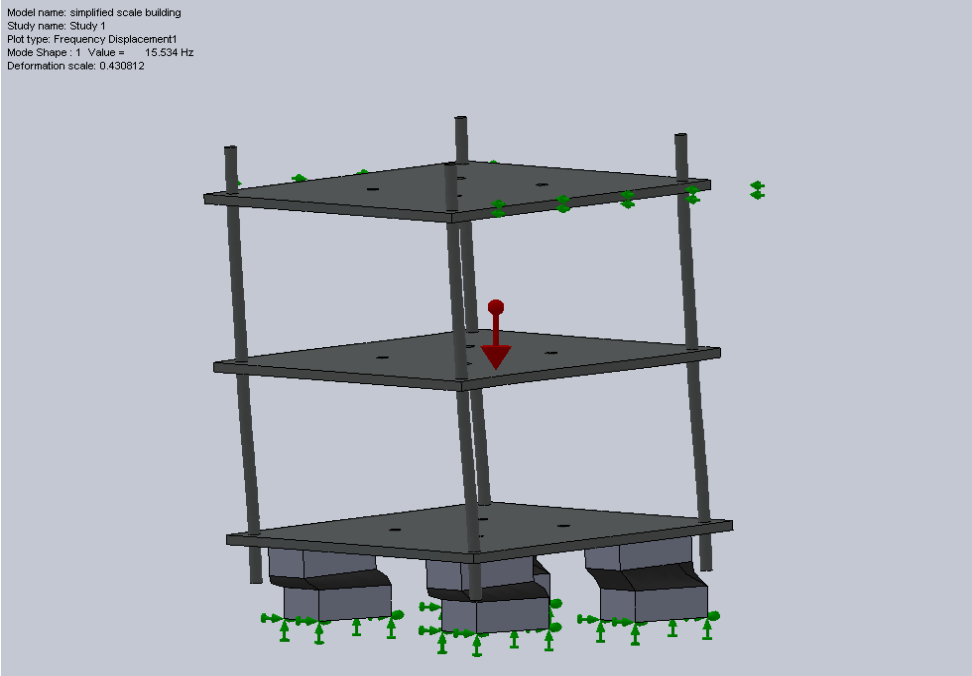

Figure E.2. The numerical model of the isolated scaled building without additional mass.

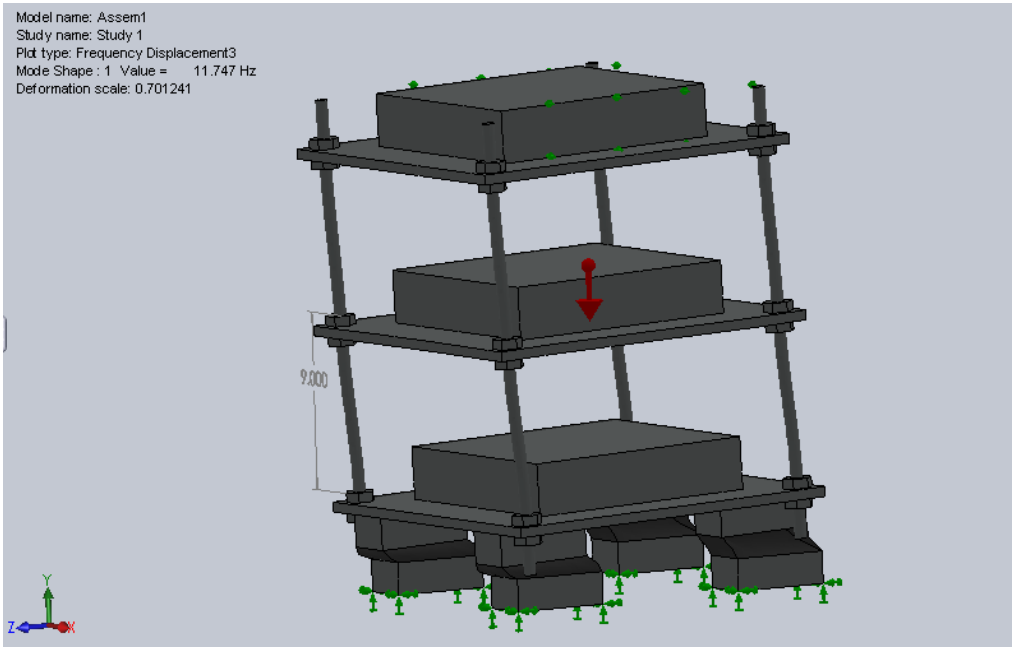

Figure E.3. The numerical model of the isolated scaled building with additional mass.

Table E.2 depicts the results of the period of the scaled building for the first natural frequency. The results of the numerical and analytical calculations are closer because both consider the perfect joints and fixed connections vs. the experimental results. Different parts and multiple connections make the real test setup softer and as a result, higher period was achieved. Moreover, the VSDA devises were made of different parts which are glued together that make the final device softer upon application of larger forces i.e. when they support the scaled building.

Table E.2. Comparison Between First Natural Periods of the Isolated Scaled Building Using Different Methods.

	Analytical SDOF approximation (sec)	Numerical analysis (sec)	Shake table experiments (sec)

With Mass	0.098	0.085	0.110
Without Mass	0.054	0.064	0.084

Figure E.4, Figure E.5 and Figure E.6 demonstrate typical transmissibility functions of the scaled building floors without additional mass in response to the base motion with 0.05 g peak acceleration in sinusoidal excitations. As shown, increasing the input electric makes VSDAs dynamically stiffer and shifts the resonant (or peak) frequencies to the right for all floors. An interesting finding is the different behavior of each floor in response to ground acceleration. Three natural frequencies occurred in the range of 5 Hz to 100 Hz while the maximum transmissibility of each floor occurs at different natural frequencies.

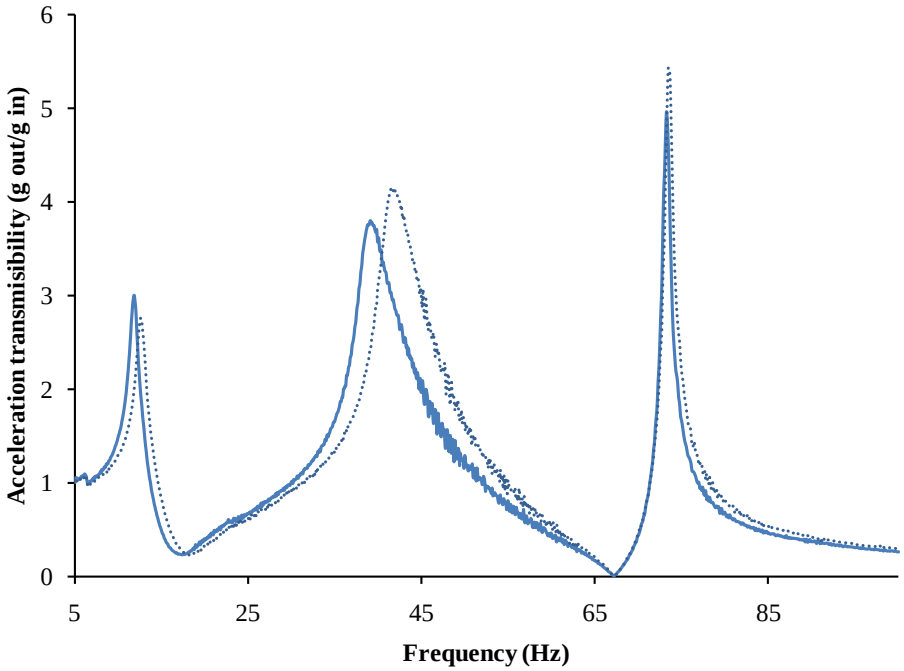

Figure E.4. Transmissibility of 0.05 g sinusoidal constant amplitude acceleration input for 0 and 1 Amps input electric currents for the 1st floor of the scaled building without additional mass.

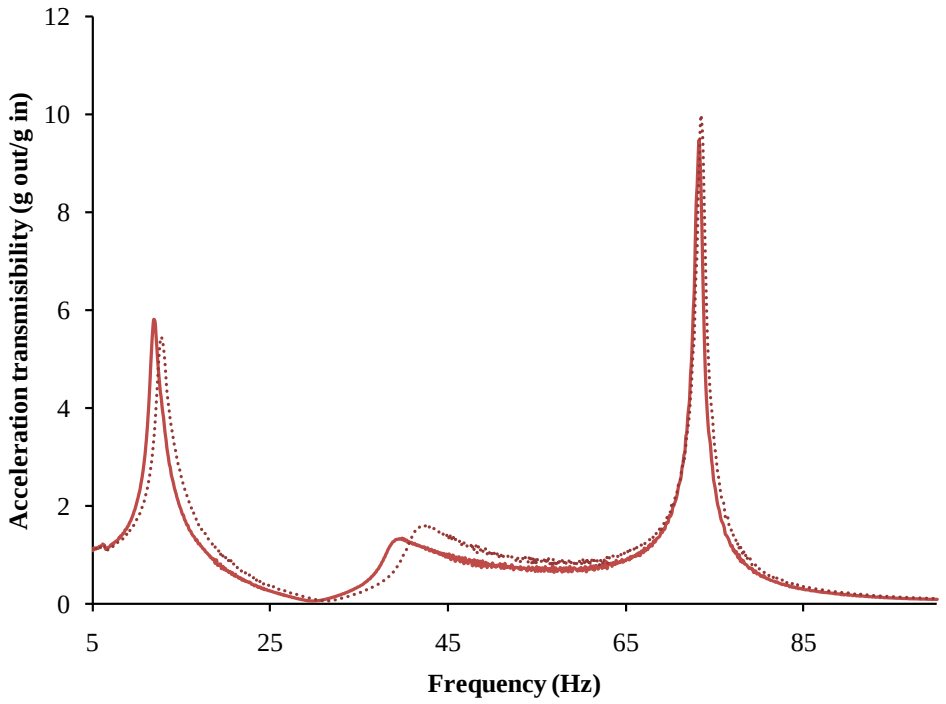

Figure E.5. Transmissibility of 0.05 g sinusoidal constant amplitude acceleration input for 0 and 1 Amps input electric currents for the 2nd floor of the scaled building without additional mass.

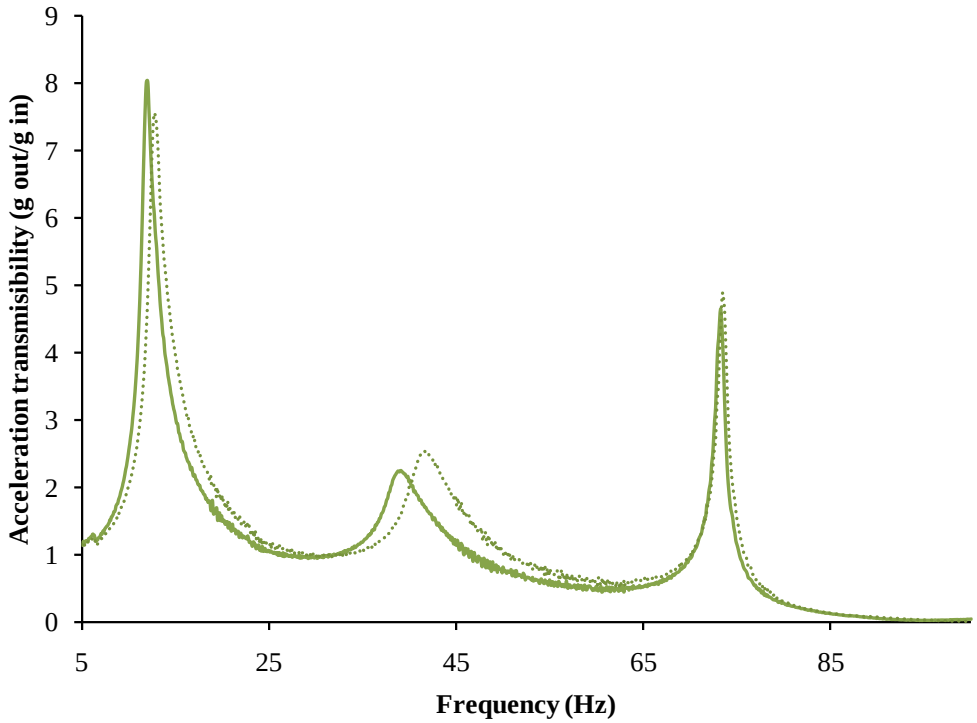

Figure E.6. Transmissibility of 0.05 g sinusoidal constant amplitude acceleration input for 0 and 1 Amps input electric currents for the 3rd floor of the scaled building without additional mass.

To further investigate the effect of utilizing of VSDAs under the scaled building, additional equal mass was introduced to each floor of the scaled building. Figure E.7, Figure E.8 and Figure E.9 present typical transmissibility of the scaled building floors with additional mass and sinusoidal input excitations with 0.05 g peak acceleration. As expected, additional mass results in the lower natural frequency of the scaled building. Effect of the VSDAs on the scaled building was decreasing maximum transmissibility of all floors due to activation for first and last natural frequency. However, it increases the maximum transmissibility of the second natural frequency. Three natural frequencies were lower in case of having additional mass on

the scaled building and the maximum transmissibility of all floors decreased for the first and third natural frequency but increased for the second natural frequency.

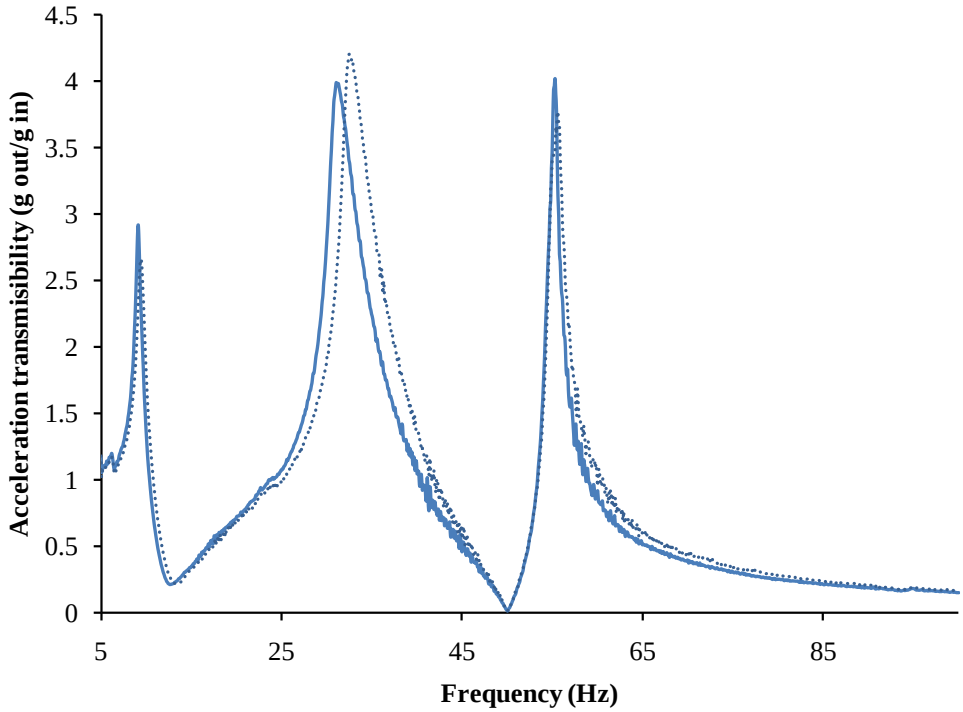

Figure E.7. Transmissibility of 0.05 g sinusoidal constant amplitude acceleration input for different input electric currents of 0 and 1 Amps for the 1st floor of the scaled building with 16.6 Kg additional mass on each floor.

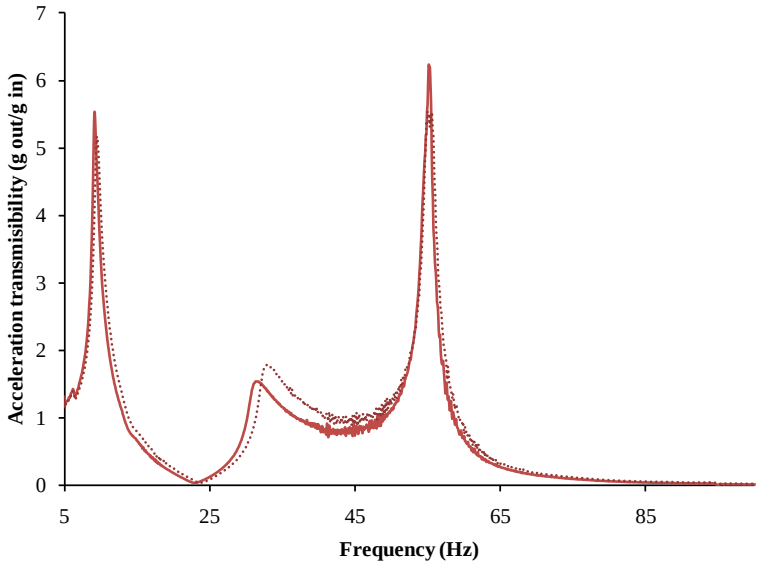

Figure E.8. Transmissibility of 0.05 g sinusoidal constant amplitude acceleration input for different input electric currents of 0 and 1 Amps for the 2nd floor of the scaled building with 16.6 Kg additional mass on each floor.

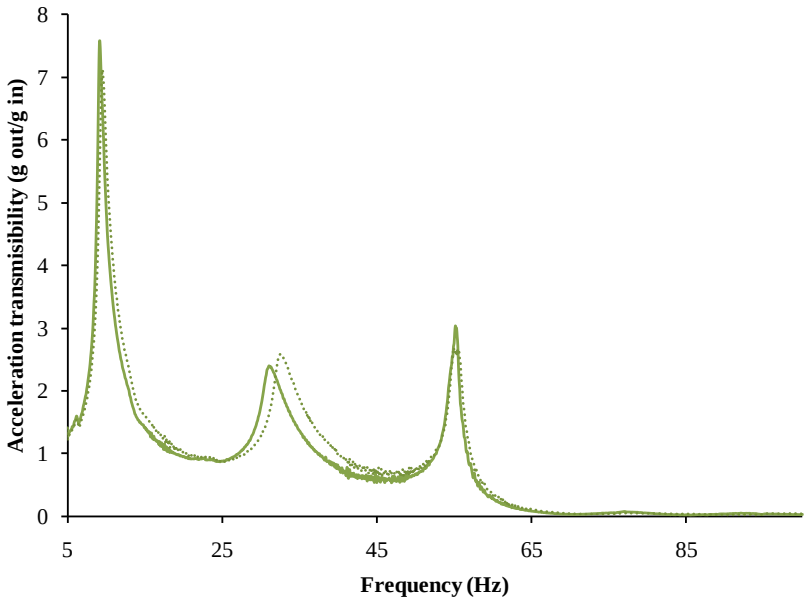

Figure E.9. Transmissibility of 0.05 g sinusoidal constant amplitude acceleration input for different input electric currents of 0 and 1 Amps for the 3rd floor of the scaled building with 16.6 Kg additional mass on each floor.